WEAR MECHANISMS OF SILICON NITRIDE BEARING MATERIALS UNDER CONTACT FATIGUE STRESSES

By

ZHENG CHEN

A DISSERTATION PRESENTED TO THE GRADUATE SCHOOL OF THE UNIVERSITY OF FLORIDA IN PARTIAL FULFILLMENT OF THE REQUIREMENTS FOR THE DEGREE OF DOCTOR OF PHILOSOPHY

UNIVERSITY OF FLORIDA

1995

ACKNOWLEDGMENTS

I would like to especially thank my advisor, Dr. John J. Mecholsky, Jr., for his constant guidance, support, and inspiration throughout the course of this work. I also wish to thank Dr. J. H. Adair, Dr. B. V. Sankar, Dr. R. K. Singh, and Dr. E. D. Whitney for advising throughout the research and for serving as committee members. I am very grateful for support by the Air Force Office of Scientific Research on the URI program.

I would like to extend my thanks to my colleagues, Mr. J. Cuneo, Mr. T. Joseph, and Dr. S. Hu for help in AFM analysis and FEA analysis. Special mention must be given to my officemates, Mr. L. P. Hehn and Dr. Y. Tsai, for the many discussions and suggestions (technical and otherwise) which helped keep everything in perspective.

I would like to express sincerest thanks to my parents for their love and encouragement throughout my entire life, and to my wife, Rongrong Jia, for her love, patience, and understanding, and for helping me to keep my sanity during the most difficult times.

TABLE OF CONTENTS

Pages

ACKNOWLEDGMENTS ii

ABSTRACT v

CHAPTER

1. INTRODUCTION 1

2. LITERATURE SURVEY 11

2.1 Theoretical Background 11
2.2 Mechanisms of Wear 18
2.2.1 Wear by Plastic Deformation 19
2.2.2 Wear by Brittle Fracture 20
2.3 Wear by Tribochemical Reaction 23
2.4 Wear Mechanisms in Si_3N_4 24
2.5 Apparent Study in Si_3N_4 Wear 25
2.6 Hertzian Stress 30

3. EXPERIMENTAL PROCEDURES 34

3.1 Silicon nitride Materials 34
3.2 Microstructural Analysis 36
3.3 Influence of Crack Size on Si_3N_4 Strength and Toughness 37
3.4 Ball on Disc Contact Fatigue Test 39
3.5 Diametral Compressive Fatigue Test 44
3.6 Characterization of Surface Geometry Using Fractal Dimension 48

4. RESULTS AND DISCUSSION 54

4.1 Microstructure of Si_3N_4 Bearing Materials 54
4.2 Fracture Behavior of Si_3N_4 62
4.2.1 R-Curve Behavior 62
4.2.2 Crack Initiation 78
4.3 Contact Fatigue Test 88
4.3.1 Stage I Wear-Roughening on the Contact Surface 92
4.3.2 Stage Wear II Wear
-Cone Crack Initiation and Propagation 104
4.3.3 Stage III Wear-Material Removal
from Outside the Contact Area 111
4.3.4 The Effect of Surface Finish
on Si_3N_4 Wear Behavior 123
4.3.5 Subsurface Damage 133
4.3.6 Effect of Microstructure on Wear Behavior 137
4.4 Diametral Compression Fatigue Test
under Different Environments 141
4.5 The Geometry of Wear and Fracture Surface 157
4.6 XPS Surface Analysis 175

5. CONCLUSIONS 178

APPENDIX A
FINITE ELEMENT ANALYSIS 188

APPENDIX B
A COMPUTER PROGRAM FOR
PREDICTION OF CRACK PATH 197

REFERENCES 203

BIOGRAPHICAL SKETCH 214

Abstract of Dissertation Presented to the Graduate School of the University of Florida in Partial Fulfillment of the Requirements for the Degree of Doctor of Philosophy

WEAR MECHANISMS OF SILICON NITRIDE BEARING MATERIALS UNDER CONTACT FATIGUE STRESSES

By

Zheng Chen

May 1995

Chairman: Dr. John J. Mecholsky, Jr.
Major Department: Materials Science and Engineering

The objective of this research was to investigate wear mechanisms of silicon nitride as bearing elements. The study is focused on two questions: (1) How does Si_3N_4 wear initiate and develop in the hybrid ball bearing system? (2) What materials and mechanical factors control wear initiation and development? The properties and fracture behavior of advanced silicon nitride bearing material, such as toughness, crack initiation and propagation, R-curve behavior, cyclic fatigue resistance, subcritical crack growth, and fractography, have been studied. The ball-on-disc cyclic-fatigue testing method has been successfully designed and applied to simulate loading

conditions in a hybrid ball-bearing operation. The diametral compression test has been used to study crack growth mechanisms and environmental influence on crack growth. The AFM, SEM, and XPS are the primary techniques that were used to study the topography and chemistry of the fracture and wear surfaces. From this research, wear mechanism models for Si_3N_4 bearing materials have been established. The causes of the wear have been determined to be directly related to a mode I brittle fracture process. The results of this research will lead to improvement in silicon nitride wear resistance by adjustment of the microstructure.

CHAPTER 1
INTRODUCTION

High quality silicon nitride (Si_3N_4) ceramics have low densities, low friction coefficients, low thermal expansions, high strengths, and high temperature and chemical stability, and are non magnetic. The combination of these properties makes silicon nitride an attractive material for rolling element bearing applications to withstand higher loads, severe environments, and high speeds [1]. The low density of the silicon nitride material presents particular advantages as the rolling elements of high-speed air turbine bearings. The centrifugal forces and gyroscopic moments induced during high speed, which are major contributors to the contact stresses generated in the bearings, are significantly reduced. Another advantage in using Si_3N_4 is that, because silicon nitride has high temperature and chemical stability, is an electrical insulator, and is non-magnetic, silicon nitride rolling-element bearings can be used at elevated temperatures, corrosive environments, and in magnetic fields in which conventional bearing steels are limited. In order to successfully use silicon nitride as rolling elements, the material must have

reasonable hardness, high toughness, and a high Weibull modulus which indicates a narrow distribution of defects in the material.

In the early 1960s, material scientists started to think that silicon nitride could be a potential rolling-bearing material [2]. Since that time, many investigators have devoted their time to processing and evaluating of silicon nitride bearing materials [3-10]. Since silicon nitride has a covalently bonded structure (hexagonal crystalline structure), difficulty in sintering became a major barrier to its manufacturing. Machining was also extremely difficult because of the high hardness of silicon nitride. All these reasons resulted in the fact that it was impossible to limit all defects, such as porosity, large inclusions, surface damage, and sintering flaws, in silicon nitride products. The various types of defects resulted in an uncertainty in the silicon nitride failure mode for many products. Even though many investigators explored wear mechanisms in Si_3N_4 and have documented their attempts in the literature [11-15], the wear mechanisms of silicon nitride in hybrid ball-bearing systems have not been precisely explained. This is because most of the failures resulted from random, external factors (such as defects caused by manufacturing and machining or improper preparation and improper selection of test) rather than from the aspects of material structure.

In the past two decades, the material manufacturing processes have been continuously improved, from porous silicon nitride materials with poor surface finish to dense materials with fine surface finish (up to 0.01 μm). Therefore, failure origins also changed from surface defects and/or large internal pores to small interior inclusions. Silicon nitride fracture and mechanical properties, e.g., strength, creep, toughness, and dynamic fatigue, have been reported by numerous authors [16-20] and show significant improvement.

In the study of silicon nitride wear mechanisms, numerous investigators have described Si_3N_4 wear mechanisms as cracking, spalling, subsurface damage, and tribochemical reaction mechanisms [20-25]. Another investigator suggested that plastic deformation was also involved [26]. The basic experiments currently used are rolling contact fatigue (three balls with one rod, or four-or five-ball contact rolling) [22,23,24,26,27], pin on disc [12], and rolling and sliding contact fatigue [11,13]. These experiments had success in evaluating quantitative volume loss with loading time. However, these experiments lack control of the wear process and, as a result, are unable to monitor the different stages in wear initiation and development. Notably, a large surface area was tested in these experiments

and it is unavoidable that random defects due to specimen preparation could involve the tests. The defects will enhance the material degradation during the tests and may result in a change in the wear mechanism. Therefore, the artificial factors due to specimen preparation could confuse the final results.

With increasing demand for Si_3N_4 hybrid bearing applications, a mechanism which can precisely describe the Si_3N_4 wear initiation and development in hybrid ball bearing is needed. The understanding of aspects of material structure (not random defects) which causes Si_3N_4 wear could be difficult to gauge by existing experiments, i.e., rolling contact fatigue experiments. Noticeably, previous studies used an excessive wear condition, which is a diamond rider sliding on a silicon nitride disc [26]. This resulted in plastic deformation and phase transformation occurring in Si_3N_4. Plastic deformation and phase transformations rarely happen in hybrid ball-bearing operations. So, these factors need to be considered in the design of a research schemes.

The understanding of the process of material failure initiation and development can be gauged by considering the following two parameters: first, the primary factor which results in silicon nitride rolling element degradation or wear in bearing systems; second, a well-defined stress field

which is similar to the stress field in the bearing systems. The well-defined stress can lead to a more precise description of wear i.e., wear initiation and wear development.

Figure 1 shows a typical bearing ball wear pattern from a recent bearing test which was conducted by Torrington Co. Based on this wear pattern, we presume that this failure was caused by brittle fracture due to contact stress fatigue.

In order to verify this, a research scheme was developed. The assumptions of the research scheme are as follows.

1. There is no significant external tangential traction force existing between the silicon nitride ball and M50 steel race because of very low friction between the M50 steel and the Si_3N_4 ball when liquid lubricant is applied. Therefore, the external tangential force can be ignored and Hertzian contact force is the only force which was considered in the designed experiment.

2. There is no three-body abrasive wear; the lubricant with which we start is free of particles.

Figure 1 SEM photo shows a typical bearing ball wear pattern from a recently bearing test. The pattern indicates the wear due to multiple Hertzian contact stress fatigue.

3. The surface of the specimens has the same or better surface finish than commercial balls. So, there is no additional wear caused by surface preparation.

4. Wear is caused by contact fatigue stress.

The objectives of this study are to investigate the mechanisms of wear initiation and development in an Si_3N_4 hybrid bearing system and to determine what material factors and mechanical factors cause Si_3N_4 wear. The results from the experiments should lead to improvement in Si_3N_4 wear resistance by adjustment of the microstructure. The work presented in this dissertation consists of four major aspects.

1. Characterization of mechanical properties for advanced silicon nitride material (TSN-03H). Toughness and strength of silicon nitride bearing material were evaluated as functions of initial crack size. The results demonstrated the material's sensitivity to crack size. In the study of failure initiation, Si_3N_4 specimens were fractured under the rotating cantilever beam test, and failure origins were identified using fracture surface analysis and chemical analysis. Based on the first stage of the study, an overview of the material properties and the material weaknesses under mechanical loading were established.

2. The models for Si_3N_4 wear initiation and development under contact fatigue stress were established by designing a wear testing method to simulate the loading condition in the hybrid ball-bearing system. Considering the general Si_3N_4 ball failure pattern during the hybrid bearing operation, a well-defined contact fatigue Hertzian stress field was applied to the silicon nitride disc-shaped specimen using a hard ball (WC). Exxon turbo oil 2380 was used as a lubricant during all the tests. By using different loading levels, cycling numbers, and frequencies, three wear stages were observed from the experiment. The mechanisms for silicon nitride wear initiation and development were determined in this investigation. Two types of advanced silicon nitride bearing materials have been used in order to study the influence of microstructure on the wear process. In this section of the dissertation, I will demonstrate the models of wear initiation and development in silicon nitride bearing materials under contact fatigue loading and explain on what they are based.

3. Investigation of crack growth in silicon nitride bearing materials under mode I stress. The fatigue crack growth rate is a key factor in determining wear development in brittle materials. The modified diametral compression testing method was employed in this part of the study. Static

and cyclic fatigue loading was used to study the mechanisms for crack growth. The tests were conducted under different environments and stress levels. The effectiveness of microstructure and environments on crack growth were evaluated

4. The failure mode was verified through surface geometric analysis. Fractal dimension techniques were applied to study the link between surface geometry and fracture and wear surfaces. Instead of using qualitative words such as smooth or rough surfaces to describe different surface appearances, the fractal dimension, a quantitative number to describe the surface geometry, was used. The fractal dimensions of wear and fracture surfaces were measured and the relationship between the wear surface and fracture surface was established. A wear failure mode was verified from this experiment.

The results from this study demonstrate the following. (1) Si_3N_4 wear in the hybrid ball bearing is a brittle fracture process under mode I stress. From wear initiation to large volume loss in the materials, the wear process follows a typical brittle fracture process. (2) Three different wear stages in Si_3N_4 bearing materials were observed. These are grain pull-out, cone-crack initiation and propagation, and large-volume material removal due to the

propagating crack curving up to the free surface. (3) Heterogeneity in the material's structure is the cause of wear initiation. (4) Cyclic fatigue crack growth contributes to major Si_3N_4 volume loss. (5) Different stress states created by contact loading can be used to study different types of failure. (6) Fractal geometry may be used to identify the material failure mode. (7) A high strength grain boundary phase and uniform microstructure can improve the wear resistance of Si_3N_4 bearing materials.

CHAPTER 2
LITERATURE SURVEY

2.1 Theoretical Background

The strength, σ, of most ceramics depends on the crack size, c, and toughness and can be obtained using fracture mechanics [28]:

$$\sigma = \frac{YK_{Ic}}{\sqrt{c}} \tag{2.1}$$

where Y is a well-documented parameter of crack and specimen geometry, K_{Ic} is the critical stress intensity factor, i.e., a measure of the toughness of the material, and $c=(ab)^{1/2}$ where a is the depth and 2b is the width of a semi-elliptical crack. When an applied stress on a material in which a crack has length c results in a stress intensity factor K_I at the crack tip larger than K_{Ic}, the material will fracture instantly. The crack can propagate continuously from the initial crack or defect, c, until the entire material is fractured, only if the stress intensity K_I is larger than K_{Ic}. However, when loading in terms of stress intensity factor (K_I) applies to the crack tip in a wave form, which is called cyclic fatigue loading, the crack can grow under global loading, $K_I <$

K_{Ic} [29,30]. Consider a structure under a global stress intensity factor K_I much smaller than the material K_{Ic} in which a crack propagates.

Due to cyclic loading or due to a combination of loading and environmental attack, such as molecular water and corrosive chemicals, the crack will propagate with time [31-37]. When the crack grows, the crack length c increases with time. The crack growth rate can be generally described as a simple power law [38]:

$$\frac{dc}{dN} = C(\Delta K)^n \tag{2.2}$$

dc/dN is the crack growth rate per cycle, ΔK is the stress intensity factor range, and C and n are material and environmental constants. The strength of the material decreases as loading time increases. The strength eventually will reach a time at which the material fractures. It is very important to be aware of the crack growth rate of materials under a particular mechanical or chemical attack during their applications. However, equation 2.2 does not fully represent reality. Actual data of crack growth rate vs. stress intensity factor fall on an S-shaped curve, or a line with variable slope when you plot a double logarithmic plot of dc/dN versus ΔK [39,40]. At low ΔK values crack propagation is extremely slow. Conceivably there is a threshold value

of ΔK below which crack growth can be ignored. Experimental verification of the existence of this threshold is difficult. A growing crack of some length has to be arrested by gradually decreasing ΔK until below the threshold.

In reality, the mechanisms of crack growth is more complicated. Using a single interpretation for the crack growth mechanism in all materials is obviously awkward, at best. Since many more parameters are involved than ΔK and another material constant such as Young's modulus, it is reasonable to assume that the mechanisms for crack growth in ductile (metals or metal alloys) materials are totally different from the mechanisms for crack growth in ceramics.

The crack growth in ductile materials is initiated by local plastic deformation [41, 42]. During the rising-load part of the cycle, slip occurs on favorably oriented slip planes resulting in crack growth. The crack growth is then inhibited by strain hardening. During subsequent cycles, the crack will continue growing in a slip plane in which slip can take place. Therefore, fatigue crack growth in the ductile material always leaves beach-marks on the fracture surface. These beach marks are formed due to crack growth in different slip planes created under different loading cycles.

The crack growth in ceramics has different mechanisms. The covalent or ionic bond structure limits crack growth through dislocation slipping. The crack growth mechanisms in ceramics are not as clear as in ductile materials. One mechanism describes the crack growth due to molecular water attack of molecular bonds in ceramics such as the O-Si-O bond in silica or the O-Al-O bond in alumina when these bonds are stretched by a tensile stress [43,44]. In recent years, the cyclic fatigue behavior of ceramics has been actively investigated [45-55]. It has been shown that crack growth occurs under cyclic loading conditions in non-oxide ceramics. This crack growth in non-oxide ceramics is inexplicable by the cracking mechanism due to molecular water attack alone. In particular, with silicon nitride, the effects of cyclic loading on crack growth have been confirmed experimentally [56]. So far, there are two mechanisms to rationalize the cyclic fatigue phenomenon experimentally observed and both of them are very dependent on microstructure and composition of materials. These are: (1) microscale-crack branching and (2) crack-path deflection [57].

In the case of microscale-crack branching, during tensile loading, the growing crack 0 ($K_0 > K_{Ic}$) branches off after growing a Δa_t distance, being followed by crack arrest ($K_1=K_2=K_3=K_4<K_{Ic}$) (Figure 2a). It is important to

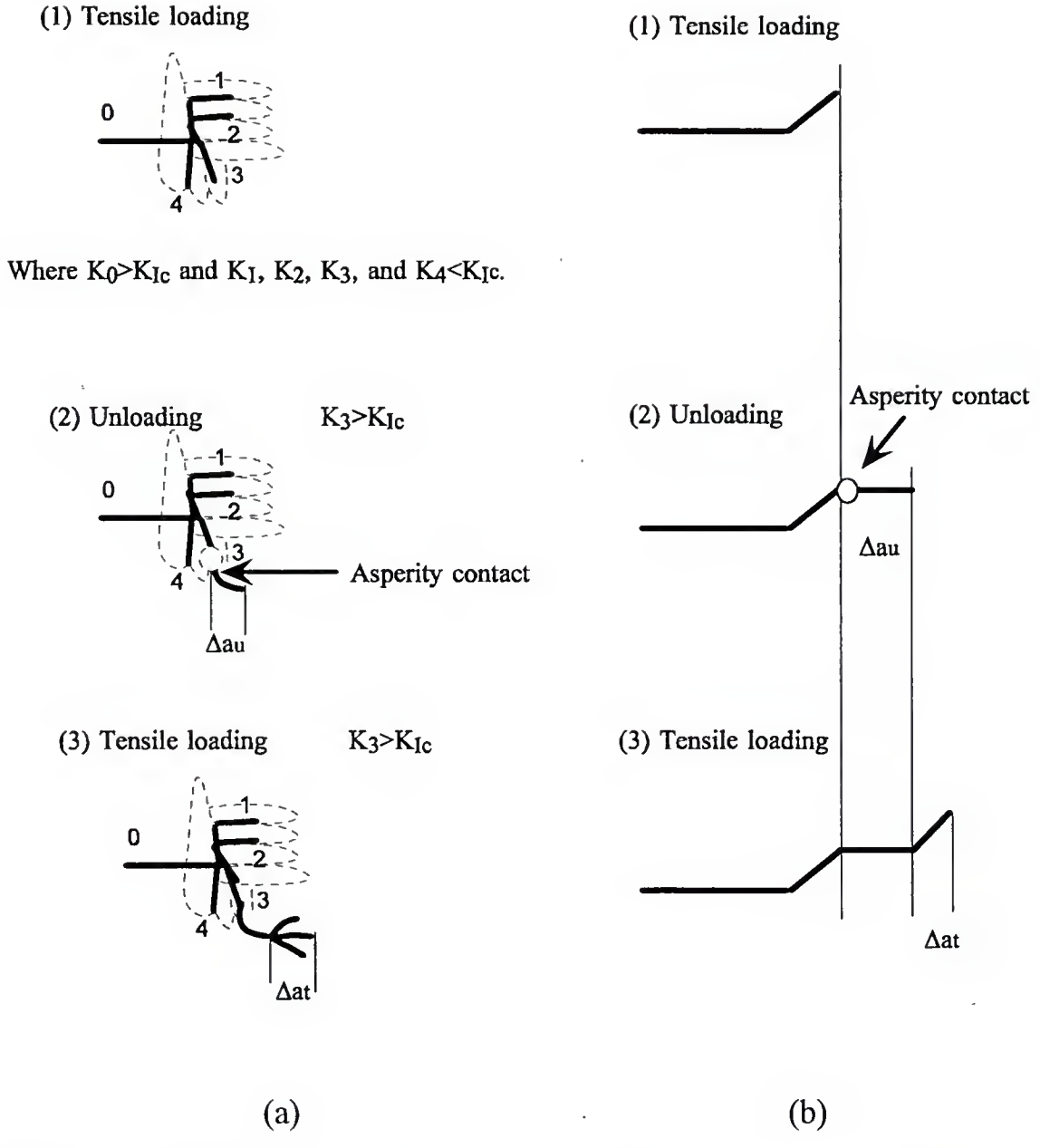

Figure 2 The fatigue mechanisms in material were characterized by microscale-crack branching in (a), and crack path deflection in (b). Δa_u and Δa_t are crack increments during tensile loading and unloading, respectively.

be aware that the stress intensity factor referred here is the local stress intensity factor. Note that such branching occurs along grain boundaries only in intergranular-fracture type materials, such as polycrystalline silicon nitride and alumina. During unloading, some of the branched cracks might grow a Δa_u distance, if there are some asperities or loose particles on the crack faces caused by the crack propagation. The advancement is most pronounced in crack 3 where the extent of asperity/particle-induced damage due to "wedge effect" is the highest. During the subsequent tensile loading, only crack 3 can grow because of only $K_3 > K_{Ic}$ at this moment. Then crack branching occurs again to arrest the cracks. Such a sequence is repeated during cyclic loading and results in cyclic crack growth.

In the case of crack-path deflection (Figure 2b), a propagating crack is deflected due to some obstacle in the front of the crack path during tensile loading. The crack is then arrested because the deflected crack is at an angle to the microscopic crack direction, consequently lowering the stress intensity factor below K_{Ic}. During unloading, in the area behind the crack tip where particle-contact was produced during the crack growth, the crack may grow due to a local tensile load to open the crack by a "wedge effect" through the

particle-contact point [57]. In this case, the crack growth occurs during the unloading rather than loading.

Previous research found little enhancement of fatigue crack growth by environmentally assisted crack growth at room temperature [58, 59]. However, the microstructural features, preexisting defect shapes, and composition of sintering aids can also affect crack growth mechanisms. Most previous experiments were conducted using bending specimens with a crack induced using a Vickers' indenter. The crack then grew from a indentation crack under a cyclic bending load.

Regardless of which crack growth mechanism is active for crack growth, the result of crack growth will eventually cause either material fracture or material loss. The material loss usually occurs in a localized region in which most likely a highly concentrated stress exists.

From an atomic scale view point, fracture or crack growth in materials is an atomic bond breaking process under stress [60-62]. The choices include a plastic-type bond break, i.e., dislocation movement, or a brittle-type bond break, i.e., mode I stress fracture, depending on material properties and bond structures, and the stress states in materials.

2.2 Mechanisms of Wear

Wear is defined as "damage to a solid surface, generally involving progressive loss of material, due to relative motion between that surface and a contacting substance or substances [63]." The mechanisms of wear can be divided into three categories. One is adhesive wear, in which two contact surfaces bonded by diffusion due to high pressure, are fractured by the motion of one substance on another substance [64]. Adhesive wear is not considered to be the case for wear in silicon nitride hybrid ball bearings because liquid lubricant is used to separate the two surfaces and hinder diffusion. Another is abrasive wear [65]. The last one is tribochemical wear.

Abrasive wear can be further divided into two types: one is two-body abrasion, in which rough surface contact results in wear; another is three-body abrasion, in which foreign particles are trapped between two solid surfaces. In principle, abrasive wear is caused by hard protuberances among the surfaces that slide over the surfaces and move material from these. There are two types of mechanisms involved in abrasive wear: wear by plastic deformation and wear by brittle fracture.

2.2.1 Wear by Plastic Deformation

A simple model can be explained for abrasive wear involving material removal by plastic deformation [66,67]. A hard protuberance, idealized as a cone of semi-angle, α, is plowed across the surface of a ductile material which plastically deforms under an indentation pressure, P. A scratch is formed in the material after the protuberance slides on the surface, and wear is assumed to occur by the removal of some portion of the material from the scratch. The normal load, w, carried by the protuberance, which causes a pressure P to act over the area of contact between the protuberance and the surface [68],

$$w = \frac{1}{2} P \pi^2 \tan^2 \alpha \tag{2.3}$$

And the wear rate, Q, (volume per unit sliding distance) can be described:

$$Q = \frac{Kw}{H} \tag{2.4}$$

where H is the hardness of material, and K a constant dependent on the friction of the materials and the geometry of the protuberance.

2.2.2 Wear by Brittle Fracture

When a hard angular particle is pressed against the surface of a brittle material, local plastic deformation can occur at the point of contact, followed by the formation of cracks which can lead to the detachment of material, and hence, to wear [69-77]. Cracks form in a brittle solid subjected to a point load. At the point of initial contact, very high stresses occur. Indeed, if the tip of the indenter were perfectly sharp and there was no plastic deformation in the material around the tip, there would be a stress singularity at this point. However, the intense stresses (shear and hydrostatic compression) are usually relieved by local plastic flow or densification around the tip of the indenter; the zone of deformed material is indicated by the letter D in Figure 3. When the load on the indenter increases to a critical value, tensile stresses across the vertical mid-plane initiate a median crack, indicated by M in Figure 3. Further increase in load is accompanied by progressive extension of the median crack. On reducing the load the median crack closes. Further unloading is accompanied by the formation and growth of lateral cracks (labeled L). The formation of the lateral cracks is driven by residual stresses, caused by the relaxation of mismatched deformation(elastic and plastic) around the region of the contact. As unloading is completed, the

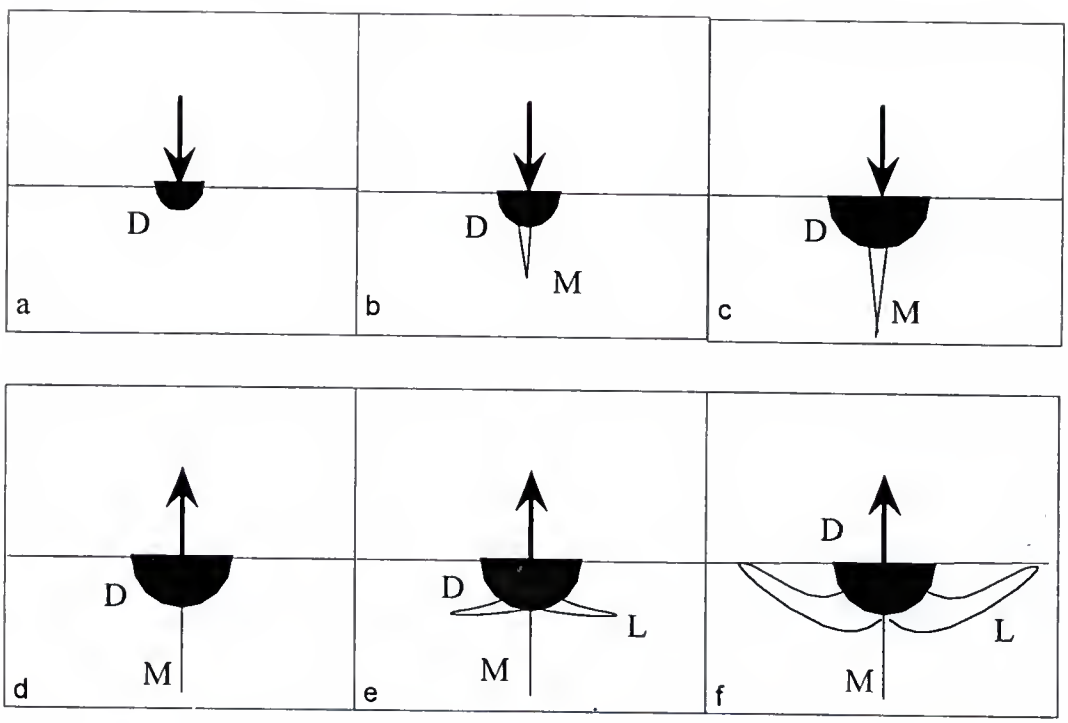

Figure 3 Diagram showing crack formation in a brittle material due to point indentation as the normal load is progressively increased from a to c and then reduced from d to f.

lateral cracks curve upwards and terminate at the free surface. The median cracks propagate down into the bulk of the solid with increasing loads on the indenter, and do not grow further during unloading. They are not associated with the removal of material. Lateral cracks, in contrast, can lead directly to wear.

Lateral cracks form only when the normal load on the indenter has exceeded a critical value, w*. The value of w* depends on the fracture toughness of the material K_{Ic} and its hardness, H [68].

$$w^* = (\frac{K_{Ic}}{H})^3 K_{Ic} \tag{2.5}$$

The ratio of H/K_{Ic} for a material provides a useful measure of its brittleness: a low value of this brittleness index corresponds to a high value of w*, and therefore indicates a material which is reluctant to fracture by indentation. This mechanism for the abrasive wear of brittle materials is based on the removal of material by lateral cracking. It is assumed that material is removed as chips from the region bounded by the lateral cracks and the free surface, and the volume wear rate, Q, is then estimated from the volume of this region [77];

$$Q = \alpha_2 N(\frac{w^{5/4}}{K_{Ic}^{3/4} H^{1/2}}) \tag{2.6}$$

where α_2 and N are a geometric constant and number of particles, respectively. In order to create this type of wear, the w here has to be equal to or larger than w*. In other words, wear by fracture will occur only when a critical load (yield strength) on each abrasive particle is exceeded.

2.3 Wear by Tribochemical Reaction

It is well known that friction and wear can cause chemical reaction to proceed much faster than they would otherwise. A number of mechanisms can be responsible for the kinetics of these tribochemical reaction [78-81]: (1) local or general temperature can be increased due to the dissipation of frictional energy; (2) the reaction products are removed periodically; (3) the diffusion of reactants increases because of injection of lattice defects by deformation and breaking of chemical bonds. The formation of the film and dissolution of matter in the chemical liquids under friction are tribochemical oxidation and hydrolysis reactions which occur only in the wear tracks. The tribochemical reaction rate is as a function of the friction coefficient of materials, traction force, and contacting velocity.

Tribochemical reaction can cause different results for different materials: for Al_2O_3 in water vapor, the wear increases due to tribochemical

reaction; while for Si_3N_4 in high humidity environment, the wear decreases due to the tribochemical reaction [82-84]. The tribochemical wear is not primary wear in Si_3N_4 hybrid bearing system. The precise mechanism of tribochemical wear is still not substantially understood.

2.4 Wear Mechanisms in Si_3N_4

Although the theoretical treatments of wear mechanisms discussed above are successful in explaining several aspects of observed behavior, they have many limitations. In some cases, this is because the theory is insufficiently developed and can not provide an accurate model for the mechanism of wear which occurs. In other cases, the mechanism itself differs significantly from that assumed in the model. In the case of Si_3N_4 wear in hybrid ball bearing applications, the observations of the wear pattern on Si_3N_4 ball surfaces (Figure 1) are different from those described with the above mechanisms for several reasons. First, the race in hybrid bearings is made of M50 steel which has a much lower hardness about {8 GPa (DHP)} than silicon nitride hardness which is about 16 GPa. The ratio of the hardness between Si_3N_4 and M50, H_{M50}/ H_{Si3N4} is well below the critical value, which could result in abrasive wear by plastic deformation.

Therefore, the wear mechanism by plastic deformation is not a contribution, or at least not a major one, in silicon nitride wear. Second, the maximum stress in the silicon nitride ball (compression/tension) in the hybrid ball bearing operation is well below the yield stress. So, the mechanism for abrasive wear of brittle materials, which is based on removal of material by lateral cracking, is also unable to explain the wear in silicon nitride. Many authors have described one of silicon nitride wear mechanisms as rolling contact fatigue [13,15,24,86-88]. However, there are few documents which explain in detail how and why the fatigue failure occurs in Si_3N_4 material. So far, few precise models for silicon nitride wear in hybrid ball bearing system have been developed, and the mechanisms of material removal in this case remain unclear.

2.5 Apparent Study in Si_3N_4 Wear

Interest in using silicon nitride as rolling bearing elements began two decades ago. Baumgartner, Dalal and Chiu began to evaluate the wear resistance of hot-pressed silicon nitride as a rolling bearing material in the early 70's [89,90]. Since then, several investigators, promoted by the increasing applications of silicon nitride in bearing systems, have explored

the wear, friction, tribochemical reaction, and fatigue behavior in Si_3N_4 bearing materials. Bhushan, Sibley, and Lucek [24,91] in their studies indicated that the wear is a contact fatigue mechanism. High tensile stress in the region just outside the contact area initiates a crack and then causes a localized failure. Morrison and Pirvics [92,93] also found that spalling was initiated from microporosity and foreign inclusions. Braza and Cheng [13] in their investigation used a rolling sliding contact test and found that the friction coefficient is governed by the type of contact rather than by the type of material. Grain pull-out contributes to a high wear rate. Galbato and Harris [15] conducted a silicon nitride wear investigation using two different testing methods: one was the five ball rolling contact test, another was the V-groove/ball rolling contact test. They also found silicon nitride failure outside the race tracks which they called spalling failure and Fischer et al [12,21] showed that a dramatic heat load could be created during high speed and high stress rolling and sliding contact. These accumulated high temperatures not only promote tribochemical reaction but also cause plastic deformation in the silicon nitride. Fischer, Tomizawa, and Akazawa [12] from their pin-on-disc experiment found that the tribochemical reaction was involved in wear mechanisms when the environmental moisture increases.

Frictional deformation was observed in Adewoye's conical riders sliding on a flat silicon nitride substrate test [22].

Considering spallation as a failure mechanism, the silicon nitride bearing lifetime was estimated using the Lundberg-Palmgren formulation based on statistical data [94,95]:

$$\frac{N_2}{N_1} = \left(\frac{\rho_{Si_3N_4}}{\rho_{steel}}\right)^{-3} \left(\frac{E'_{Si_3N_4/steel}}{E'_{steel/steel}}\right)^{-6.3} \tag{2.6}$$

where $N_{2,1}$ is the fatigue life-time of silicon nitride with steel bearings and steel with steel bearings, respectively. E′ is a reduced modulus which is $2/[(1-\nu_1^2)/E_1+(1-\nu_2^2)/E_2]$, $E_{1,2}$ a Young's modulus of bodies 1 and 2, respectively, and ρ is the material density. From this experimental equation, the higher modulus leads to higher contact stress and thus lower fatigue life, but the difference in density leads to even greater increases in fatigue life ($N_2/N_1 \approx 5$) at high operating speeds where centrifugal loading is predominant. These experiments indicated silicon nitride materials have very good wear performance in high speed bearing applications, longer fatigue lifetime and higher loading capacity.

However, the lifetime of silicon nitride bearing elements is much shorter than the prediction due to the variation of defects. Spallation is

considered as one of many failure patterns in the bearing elements. Hadfield and Stolarski found that artificially induced defects in the silicon nitride balls can significantly reduce the ball lifetime [87]. In reality, the failure could be initiated from random surface defects, such as pores, scratches, cracks, and inclusions. The random defects result in the measured fatigue lifetime values being scattered. It is obvious that the wear mechanisms obtained from previous experiments were also greatly influenced by wear testing methods, material defects and surface condition. Evaluation of a testing method is dependent on whether the selected wear testing method can represent the predominantly loading condition in bearing applications and can result in a similar wear pattern to these observed in bearing applications.

Bhushan and Sibley [91] published silicon nitride sliding friction coefficient data for various contacting materials and environments in 1981. The friction coefficient between M50 and silicon nitride in different lubricants range between 0.11 and 0.36. The low friction values indicate that the tangential traction force on the contact surfaces in the systems is very small and can be ignored without change in its primary loading condition.

Most of Si_3N_4 failure in the hybrid ball bearing systems were classified as local surface failure. The predominant failure appearances in the surface are fracture patterns under cyclic contact fatigue. However, the failure region is localized, not catastrophic. No evidence of plastic deformation was observed [15, 21,24]. The wear is attributed to material removal by fracture. Since most of the studies were based on rolling contact fatigue and pin on disk experiments, the contact areas are not well defined due to multiple contact paths on the rolling specimen surface. Stress states could also overlap each other. All these factors make the study of the wear initiation and development difficult. In addition, the high speed friction in limited contact areas could create a significant localized temperature rise in the contact area. Therefore, the wear process and failure appearances from these tests may not precisely represent the failure patterns observed in the silicon nitride hybrid bearing systems.

Recently, the incidence of failure related to microstructure defects and surface finishing conditions has been substantially reduced by development of more uniform, defect-free, dense silicon nitride materials and more sophisticated surface finishing techniques. More substantial study of the wear mechanisms in these advanced materials is needed in order to more

fully understand the performance of these materials in the bearing operation based on their structural behavior aspects rather than their material defect aspects. Far fewer investigations have evaluated the problems, such as silicon nitride wear initiation and development, the influence of microstructures on wear behavior, and wear surface topography, in hybrid ball bearing systems.

2.6 Hertzian Stress

In rolling element bearing systems, the silicon nitride materials are under a cyclic contact stress field during the bearing operations. This type of stress state can be created in a plate by simply pressing a rigid hard ball on a large flat brittle plate. The stress field was proposed by Hertz [96] and well described by others [97]. The axisymmetric stress field is shown in Figure 4 under the following assumptions: (1) there is no traction force on the contact surface (this is a reasonable assumption for the conditions of very low friction coefficient between silicon nitride and M50 steel under liquid lubricant) and (2) there is no plastic deformation in the materials under the applied load. Therefore, the tensile stress field outside the contact area creates a condition for crack initiation and propagation.

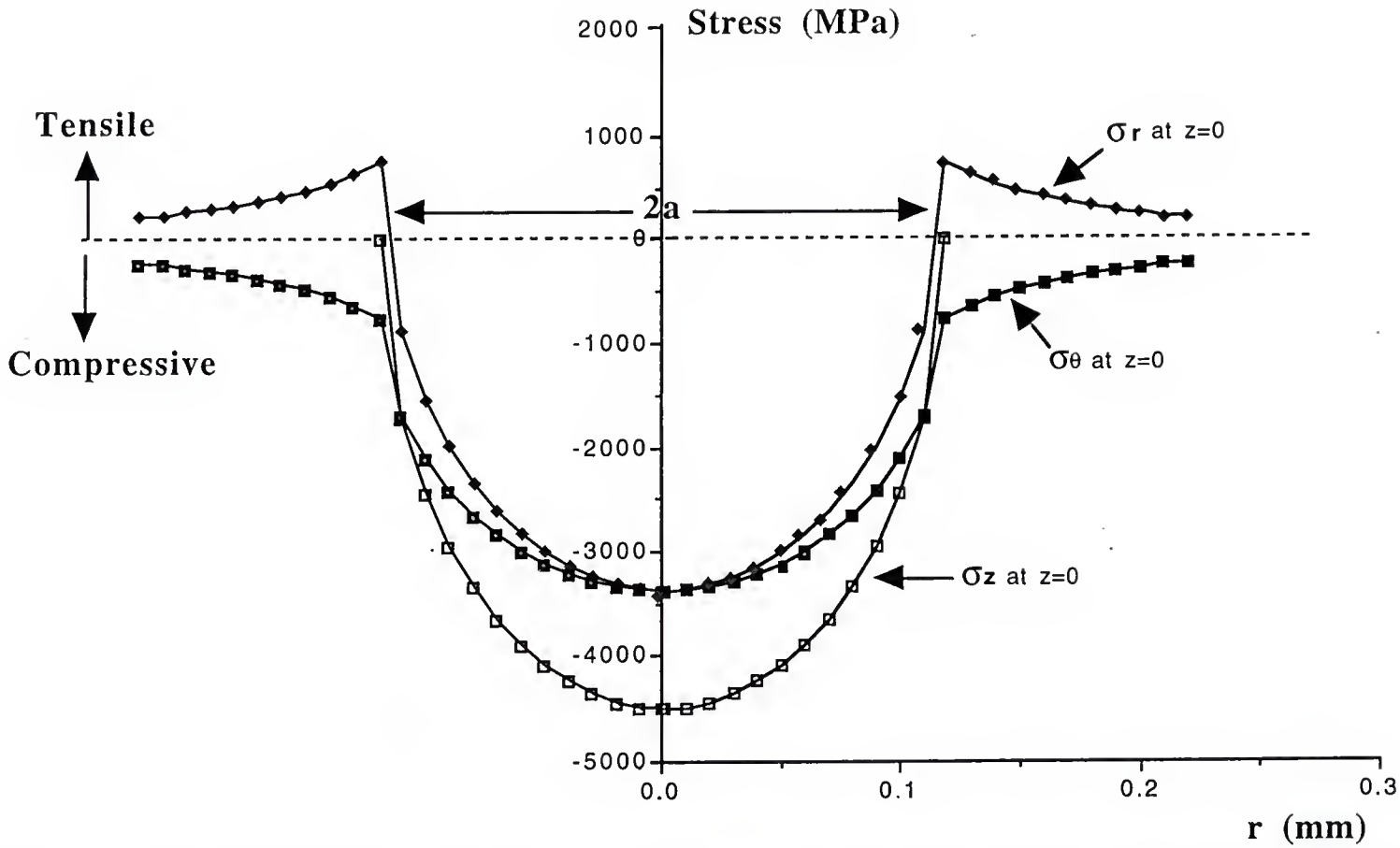

Figure 4 Stress distribution at the surface and along the axis of symmetry caused by Hertz contact load acting on a circular area with radius a. The maximum contact stress is 4.5 GPa.

Several investigators have studied the wear mechanisms of silicon nitride materials under high contact stress [99-103]. Therefore, severe plastic zones are initiated underneath the contact surface. These investigators found that plastic deformation induces slip regions and creates lateral cracks that then induce wear by removal of materials from these damaged regions. Other investigators described the subsurface damage due to a shear fault loop underneath the contact surface. It is difficult to understand that a brittle structure will fracture under a shear stress within a hydrostatic compression region. Obviously, the local plastic deformation created using a indenter at high local pressure could result in structural failure either on the surface or subsurface. .However, the stress field is beyond the Hertzian stress field definition once plastic deformation occurs in the contact region. Therefore, it is awkward using this mechanism to explain wear in bearing systems which always operate under Hertzian stress field. Other investigators observed that an unstable cone crack forms at a characteristic load ($K_I > K_{Ic}$) [98]. However, few investigators have studied the stable cone crack initiation and growth in silicon nitride bearing materials under Hertzian cyclic contact loading.

A mixed stress state created by Hertzian contact provides an opportunity to investigate the failure mode for different materials. Many material structures are operated under Hertzian type loading such as various types of bearing operations.

Brittleness of the materials is an obvious factor which causes material wear. However, the precise mechanisms of wear under contact fatigue stress are not clearly determined. Several subjects need clarification and examination: (1) wear initiation and development in silicon nitride bearing materials under cyclic Hertzian contact stress; (2) the influence of material structural aspects on wear; and (3) the relationship between the wear surface and fracture surface.

CHAPTER 3
EXPERIMENTAL PROCEDURES

3.1 Silicon Nitride Materials

Two types of silicon nitride bearing materials which are currently widely used in bearing industries were selected as the test materials. One is manufactured by Toshiba Co. and whose brand name is TSN-03H. It was designated as type A. Another material is from Cerbec with a brand name NBD-200. This material was designated as type B in this research. The physical and mechanical data of these materials which were provided by the manufactures are listed in Table 1. The geometric configuration of these materials as supplied include about 10 mm diameter cylinders and 16×12×6 mm rectangular plates. The study focused more on type A materials rather than type B because more type A material was available. Type B was used for comparison purposes. The composition of type A is silicon nitride with primarily Y_2O_3 and Al_2O_3 as sintering aids. The type B is silicon nitride with primarily MgO as the sintering aid.

Table 1 Properties of two Si_3N_4 bearing materials.

Material	Density (g/cm^3)	Young' s Modulus (GPa)	Poisson's Ratio	Hardness (GPa)	Toughness ($MPam^{1/2}$)	Flexural Strength (MPa)	Hertzian Compressive Strength (GPa)	Thermal Conductivity ($x10^{-6}$ W/m-k
Type A	3.24	300	0.27	16	6	1000	/	27
Type B	3.16	320	0.26	17	4	800	28	29

* All data listed were provided by the vendors.

3.2 Microstructural Analysis

Specimens 10 mm in diameter and 3 mm in thickness were cut from type A and type B silicon nitride rods, respectively. The specimens then were ground using a 30 μm and then a 15 μm metal bonded-diamond polishing plates to remove any visible scratches or pits on the surfaces. An automatic polishing machine then polished these samples until the samples showed mirror-like surface. The measured surface roughness of all the specimens was less than 6 nm.

Surface roughness is calculated from a surface image using the compute software which comes with from NanoScape III. The Surface roughness value, RMS, is the standard deviation of the Z values with the given area and calculated using the following expression:

$$RMS = \sqrt{\frac{\sum (Z_i - Z_{ave})^2}{N}} \tag{3.1}$$

where Z_{ave} is the average of the Z values within the given area, Z_i is the current Z value, and N is the number of points within the given area.

Two techniques were used to study the microstructure of the materials. One of these techniques is plasma etching, that is, using corrosive gases activated by plasma arc to react with the grain boundary phase. The

grain morphological image is created due to the grain boundary phase removed by chemical reaction. This plasma etching was conducted by Pratt and Whitney (West Palm Beach, FL). Scanning electron micrographs of the resulting silicon nitride microstructure of etched samples were imaged by JOEL 6400 SEM.

Another technique which was employed used the atomic force microscope (AFM). The polished samples were directly analyzed using the AFM. We take advantage of AFM's high 3-D resolution feature to identify the different heights between boundaries and grains on the polished surface. This tiny difference in the heights is due to the grain boundary phase and the fact that the grains have different wear resistance during the polishing process. The computer digital images of the resulting silicon nitride microstructures were created using Digital's Nanoscope III.

3.3 Influence of Crack Size on Si_3N_4 Strength and Toughness

The indentation-strength technique was applied to type A silicon nitride. The geometry of the specimens used was 16 mm long, 12 mm wide and 6 mm thick. The surface finish roughness was 1 μm. The initial flaws were introduced using a Vickers diamond pyramid. Indentation loads were

0.1, 0.2, 0.5, 1, 2, 5, 7, 24 kg, respectively. Larger initial flaws in the surface of specimens were created by applying multiple indentations. A seven kilogram indentation load was used to make 5, 7, 9, 12, 15, and 25 impressions in different specimens, respectively, along the middle line of the tensile surface perpendicular to the tensile stress direction. The distance between each crack tip was kept within 10 μm. Indented samples were then mounted in a 3 point fixture whose span distance was 10 mm. Cyclic loading in a form of a half sine wave was applied to the samples. The cyclic tensile stress range from 100 MPa to 0 MPa on the indented surface. Each indented specimen experienced 300 loading cycles at 1 Hz frequency. The purpose of this pre-cyclic loading is to release residual stress around the crack tip, which was induced during indentation, and to link multiple indent cracks into a large single crack. Afterwards, the specimens were fractured using a three point-bend test fixture in an Instron test machine. The span distance used was 12 mm and the displacement rate was 0.02 mm/sec. The fracture strength σ was calculated using:

$$\sigma = \frac{3LP}{wt^2} \tag{3.2}$$

where L is the span distance, P the load, and t and w the thickness and the width, respectively. The critical flaw size, c, and mirror size r were measured directly from the fracture surface under optical microscope. In Figure 5, a schematic shows how to measure c and r. The mirror size r was a larger value from r_l and r_r, where r_l is measured at the left side of mirror boundary and r_r is measured at the right side mirror boundary. The toughness of type A material was measured using the following equation:

$$K_{Ic} = 1.24\sigma\sqrt{c} \tag{3.3}$$

The reason to choose 1.24 as the crack geometry constant is because the indentation residual stress has been released during cyclic loading.

3.4 Ball on Disc Contact Fatigue Test

Disc-shaped specimens of type A and B silicon nitride materials were cut from 10 mm diameter rods in about 3-5 mm in thick. The specimens then were ground down to 15 μm using diamond polishing plates in order to remove any visible scratches or pits. An automatic polishing machine further polished these samples until the surface roughness was less than 6 nm. A 4.76 mm (3/16") hard ball (WC) with surface roughness = 10 nm was used as a rigid indenter. The ball was used to create a Hertzian stress in

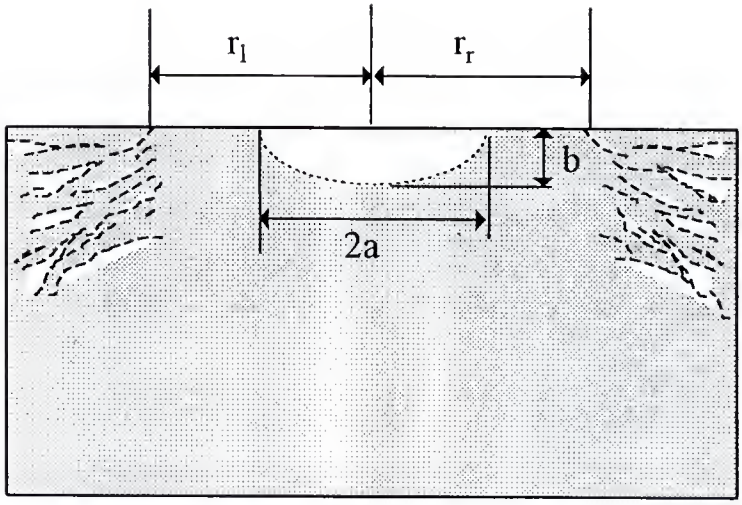

Figure 5 Schematic showing a fracture surface. The initial flaw size c is calculated using $c = \sqrt{ab}$. r represents a mirror size which is a larger value from r_l and r_r.

Si_3N_4 discs. Cyclic loading in the form of a half sine wave was used in the experiment. The number of cycles which varied from 1 cycle to 5 million cycles was chosen to examine the wear initiation and development in Si_3N_4 materials. A frequency range (5, 7, and 10 Hz) was used to investigate the frequency effectiveness on fatigue lifetime of the materials. The maximum contact stress was calculated using the following expression [97]:

$$\sigma_{max} = \left(\frac{6PE^{*2}}{\pi^3 R^2}\right)^{1/3} \tag{3.4}$$

where

$$\frac{1}{E^*} = \frac{1-\nu_1^2}{E_1} + \frac{1-\nu_2^2}{E_2} \tag{3.5}$$

and P is the applied load, R the radius of the indenter, $E_{1,2}$ and $\nu_{1,2}$ the Young's modulus and Poisson ratio of the disc and the indenter, respectively. The different maximum compressive stresses (3.2, 7, 10, 15, 17, and 20 GPa) were applied to the specimens, respectively.

The strain in the Si_3N_4 due to contact loading is within the elastic range. This was verified using the following experiment. A fine surface finished silicon nitride disc was coated with about 50 nm thick Au-Pd. The specimens then were loaded at different contact stresses. The Au-Pd coating recorded the contact area corresponded to each loading level. The measured

radius a′ of the contact areas was plotted with the calculated radius a of the contact areas in Figure 6. The calculated radius a is given by an elastic equation [97]:

$$a = (\frac{3PR}{4E*})^{1/3} \tag{3.6}$$

When a load starts to cause the measured area deviation from the calculated area, the load is a transition load. Loading above this value will result in plastic strain occurring in the Si_3N_4. All the loads which were used in the contact fatigue experiment were below the transition load. Considering the advantage in test time, higher contact stresses than the stresses used in bearing operations were used most of time in this experiment. The Hertzian stress distributions within the Si_3N_4 material were calculated using the finite element analysis method. This calculation was performed in collaboration with Wright-Patterson Air Force Laboratory. The detail of this analysis is described in Appendix A.

The contact fatigue test was designed to simulate the loading condition in the Si_3N_4 hybrid ball bearing system under the assumption that there is no external tangential traction force on the contact surface. This is because very low friction between silicon nitride and M50 steel was

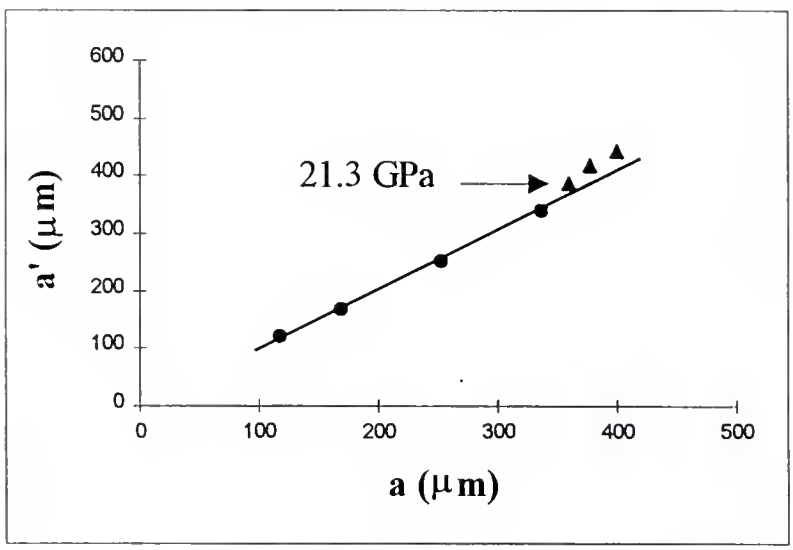

Figure 6 The plot shows measured radius a' of the contact area vs. calculated radius a. Some inelastic deformation occurred in the contact area after the contact stress exceeded 20 GPa (labeled with solid triangles).

observed [91]. Hertzian contact stresses are applied to the silicon nitride specimens using the WC ball. The tests were conducted in an MTS machine using a load control mode. Exxon turbo oil 2380 was used at the contact surfaces as a lubricant. A schematic of the test method is shown in Figure 7.

From this test, two interesting regions were investigated. One was the contact area where initial wear occurred. The whole wear process in this area was able to be examined. Another was the tensile region which was outside the contact area. From this region, the cone crack initiation, propagation and its path were examined afterwards. This test method provides total control in stress level, cyclic frequency and the number of cycles. The stress state in the contact region is also well defined. Therefore, the damage process (or wear process) under the contact stress region has be closely monitored.

3.5 Diametral Compressive Fatigue Test

The diametral compression test was introduced by Carniero and Barcellos in 1953 [104]. This test is primarily used to test the strength of brittle materials because of the ease of simple preparation and simple loading. The specimens fracture from interior (rather than at a free surface),

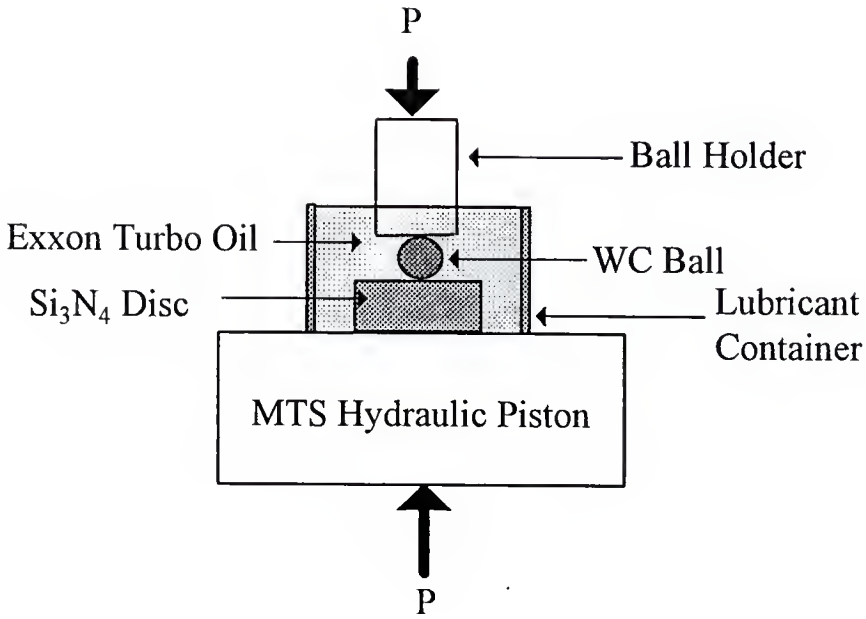

Figure 7 A schematic which exhibits the ball on disc contact fatigue test.

and biaxial stress is produced within the test specimen (along the plane AB in Figure 8). The biaxial stress state, which is similar to the stress state near the contact area of rolling elements in the bearing systems, can be used to study crack propagation. The configuration of the specimen is also ideal for measurement of crack propagation in the materials. Moreover, the test can also be used for *in-situ* monitoring crack growth under cyclic tensile and compressive stresses simultaneously, when a pre-crack is induced in the middle surface of the specimen using an indentation technique. If the specimen is acted on by a pair of concentrated loads, the tensile stress σ_{xx} can be calculated based on classical plane elasticity [105, 106]:

$$\sigma_{xx} = \frac{P}{\pi R} \tag{3.7}$$

where P is the applied concentrated load per unit length along the thickness of the specimen, and R the radius of the sample. In reality, the load applied on the specimen is distributed on a finite width instead of a line (Figure 9). The tensile stress under a distributed load was calculated based on the equation [107]:

$$\sigma_{xx} = \frac{P}{\pi}\left(\frac{1}{R} - \frac{2b^2 + 4(R-y)^2}{b^2\left(b^2 + (R-y)^2\right)^{1/2}} + \frac{4(R-y)}{b^2}\right) \tag{3.8}$$

where b is the half-width of the distributed load (Figure 9), and y the

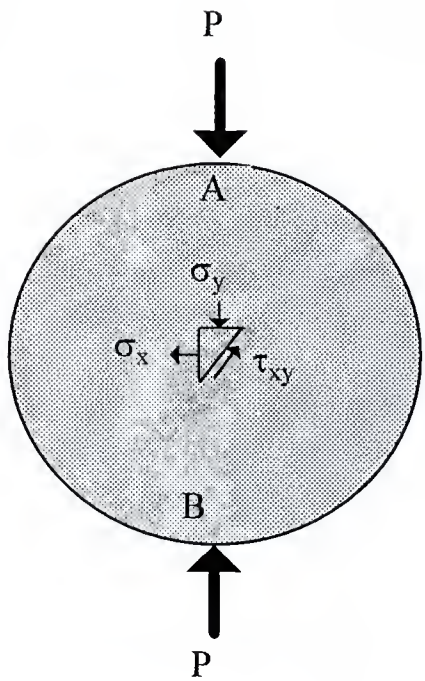

Figure 8 Schematic showing a diametral compression test. A biaxial stress state exists along plane AB which is parallel to the loading direction.

distance from the center of the specimen along the radius parallel to the loading direction. Therefore, the stress calculated from equation 3.7 is a more accurate description of the stress state encountered by the specimen than equation 3.6.

Different environments were employed in this experiment to study the influence of environment on crack growth rate. A schematic of the testing system is shown in Figure 10. Crack growth was monitored by a traveling microscope. Precise measurement was conducted using an optical microscope when the samples were removed from the testing machine after experiencing a number of loading cycles. The specimens used in this experiment were 10 mm in diameter and 2.5 mm in thickness. Both Type A and B were used in this test for the purpose of comparison. The surfaces of the specimens were polished and the surface roughness was less than 6 nm.

3.6 Characterization of Surface Geometry Using the Fractal Dimension

Two different techniques were used to experimentally measure the fractal dimension. One technique used dental impression material to create a negative replica of the fracture surface. After the replica dries, a positive of the fracture surface is made by filling the cavity formed in the impression

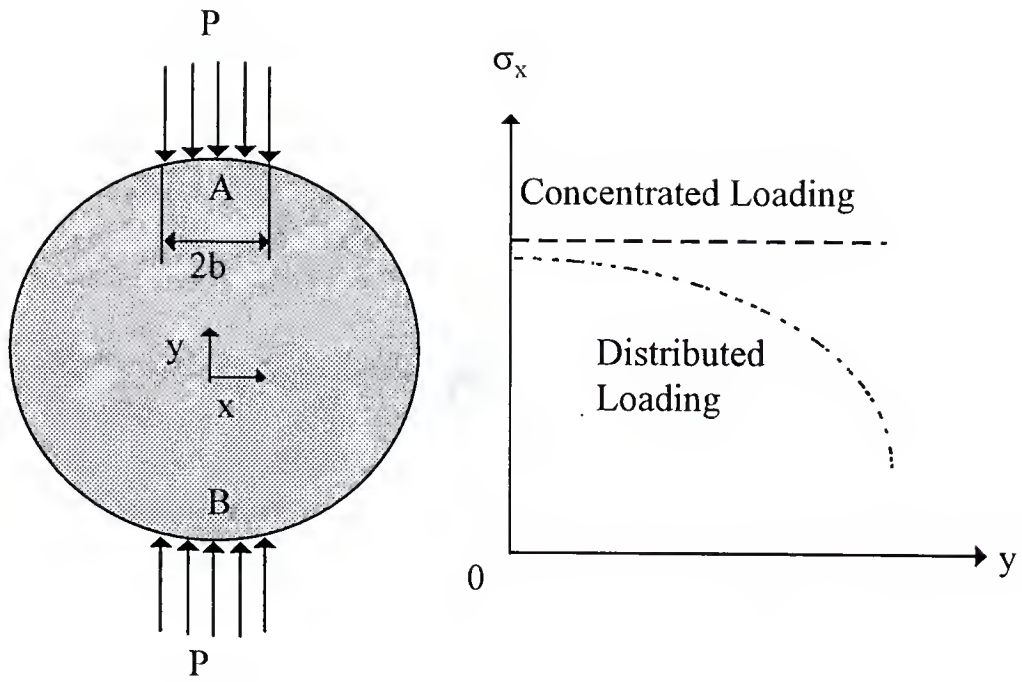

Figure 9 When an applied load is distributed on a width 2b, the tensile stress σ_{xx} along plane AB shows that it is different than the stress caused by the concentrated loading.

material with epoxy. After the epoxy is cured, the positive impression is coated with an electroless nickel plating. The coated sample is then covered by epoxy. The replica is now treated in the usual manner to produce slit island contours by polishing approximately parallel to the fracture surface (Figure 11). The detail of this process was described by Plaia[108]. The second technique uses the atomic force microscope (AFM) [TopoMetrix, Santa Clara, CA 95054]. The basic components of an AFM are shown in Figure 12. The cantilever beam keeps a constant distance between the tip and fracture surface by control of the beam angle. The distance between the tip and the surface is determined by the atomic force between these two materials. When the sample moves in the x-y plane, the change of the surface profile is measured using PSPD (photo sensitive position displacement) by detecting the angle change of the reflected laser beam from the cantilever beam. The AFM creates a 3-D image directly from the fracture surface. Packaged software then sections the 3-D fracture surface image parallel to the fracture surface. This sectioning forms slit islands from which the fractal dimension is obtained. Monotonic fracture surfaces, fatigue fracture surfaces, and wear surfaces were used in this experiment to investigate the link between the fracture surface and the wear surface.

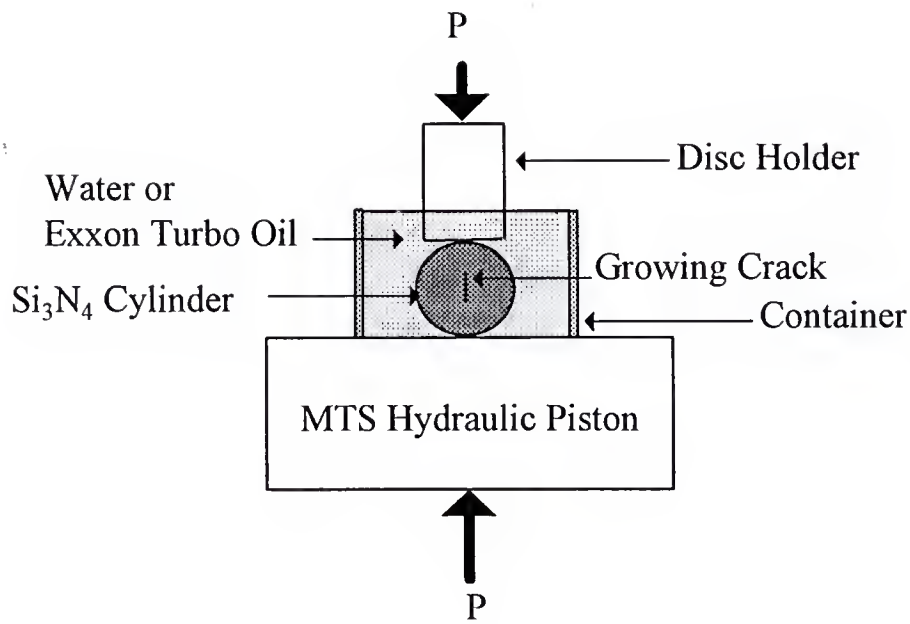

Figure 10 A diametral compression fatigue test used to study the influence of environment on crack growth.

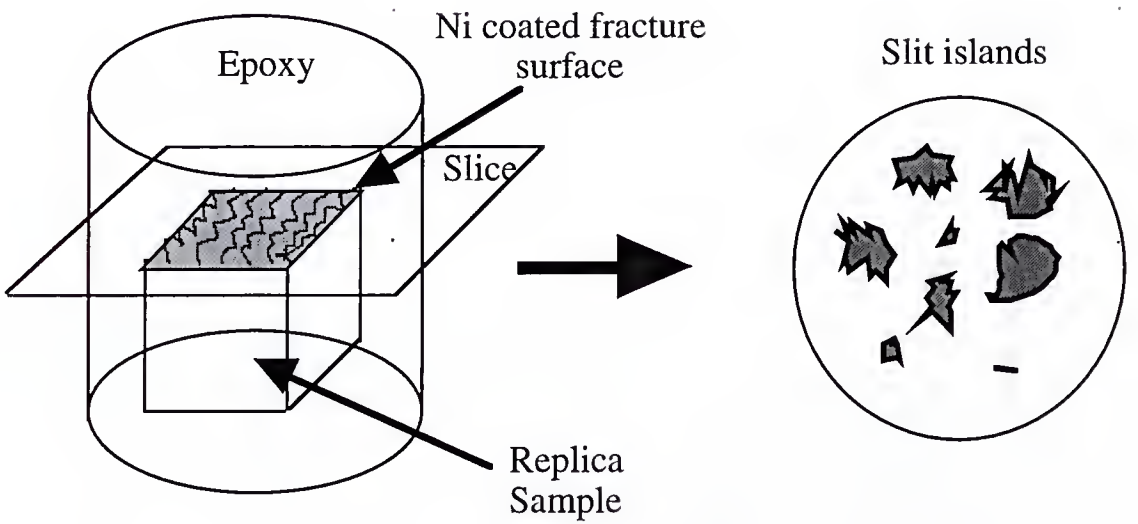

Figure 11 Schematic showing the slit islands of the fracture surface obtained from the polishing method.

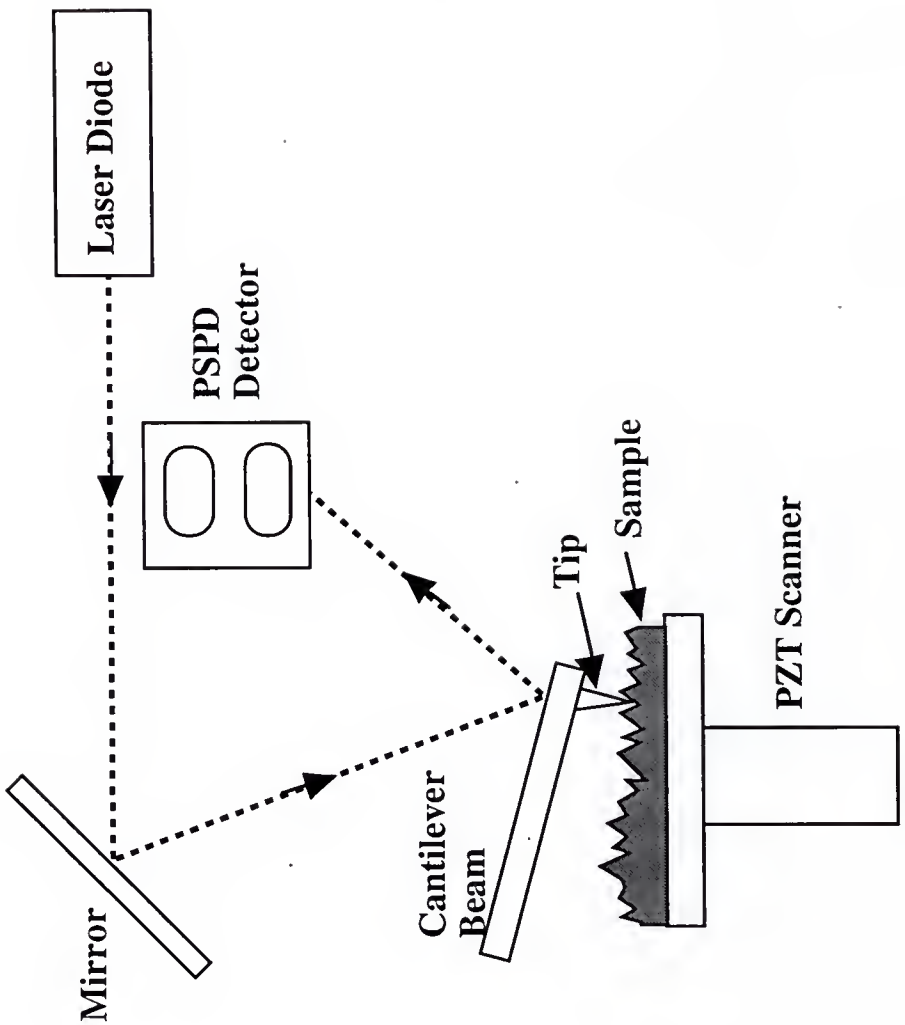

Figure 12 Basic components of the AFM.

CHAPTER 4
RESULTS AND DISCUSSION

4.1 Microstructure of Si_3N_4 Bearing Materials

The mechanical properties of silicon nitride are greatly influenced by its microstructure. SEM photomicrographs of Type A and B silicon nitride after plasma etching are shown in Figure 13. These two specimens were carefully prepared, to show the complete structure in 3-dimensions. In both pictures, the β phase grains showed a rod-like grain structure. Type B has some amount of very fine (0.1 μm or less) grain structure. The finer grains generally are distributed among the intersections of large rod-like grains. Type B also has some larger size rod-like grains, i.e., over 10 μm long and 2 μm wide. The shapes of all grains in Type B are irregular and nonuniform. Type A shows more uniform grain structure and has very few large sized grains. The cross-sections of all the rod-like grains have a hexagonal geometry. Most of the grains in Type A are less than 2.5 μm long and about 0.5 μm wide. Their aspect ratio is about 5. Closer examination of the second (sintering) phase distribution in the microstructure under high

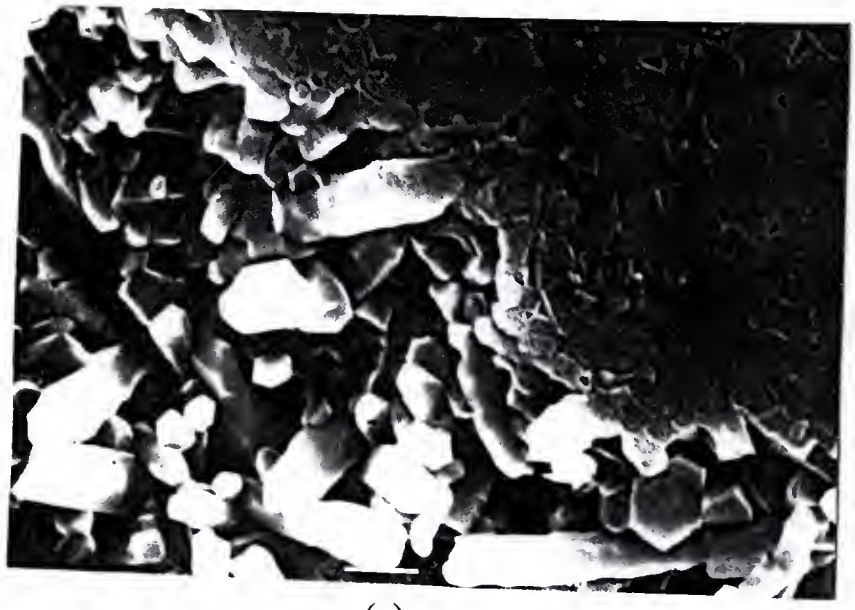

(a)

(b)

Figure 13 SEM photos show the microstructures of Si_3N_4 bearing materials in both 2 and 3-dimensions. (a) type A material and (b) type B material.

magnification shows that most of the sintering phase material in Type A is located at the triple-point of the grains (Figure 14 a). Only a very small amount of sintering phase was found to exist along the grain boundaries in Type A. In contrast, the sintering phase in the Type B microstructure is uniformly distributed along the grain boundaries and has a much thicker grain boundary phase than the grain boundary phase in Type A microstructure (Figure 14 b).

Even though the plasma etching technique can give a clear picture of the grain structure, the process is time consuming and expensive. Another purpose of the characterization study was to try to find a new way to characterize the microstructure in an easy and more cost effective way. Observation of the wear process showed that material removal was easier with softer and less wear resistant materials during the polishing process than with harder and high wear resistant materials. After a certain amount of polishing, differences in heights between the grain boundaries and grains appear. The scanning electron microscope (SEM) has high resolution in the lateral direction, but poor resolution in the vertical direction. The SEM can not resolve height differences between grains and grain boundaries less than 20 nm. The atomic force microscope(AFM) uses a small tip, generally

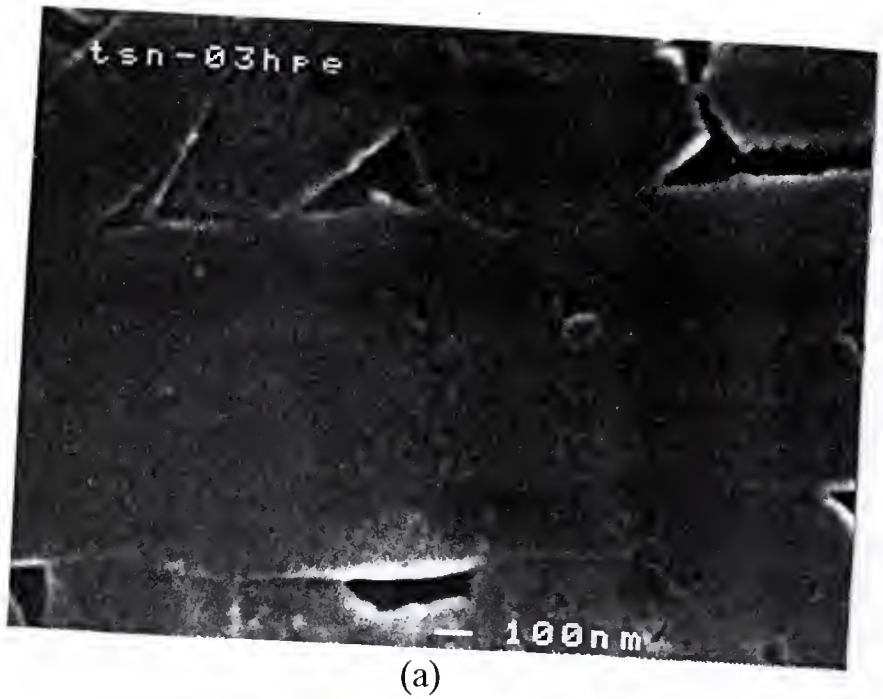

(a)

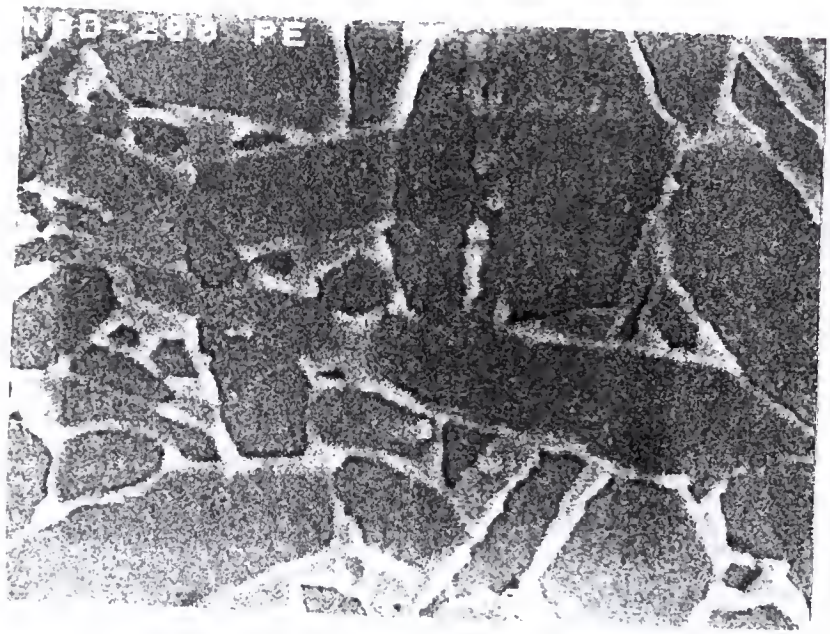

(b)

Figure 14 High magnification pictures display that the sintering phase is distributed in the triple-points (a) rather than along the grain boundaries (b). (a) Shows Type A material and (b) Type B material.

5-10 nm, to generate a profile of the surface. The AFM is non-destructive; the tip uses van der Waals forces on the order of a 10 pN-1μN to generate an image. The basic components of an AFM were shown schematically in Figure 12. The AFM has been widely used for the study of surface topography and roughness on many types of materials, in part, because it is non-destructive to the surface and requires little or no sample preparation. Because of the differential hardness of Si_3N_4 grain boundaries, a Si_3N_4 surface polishes preferentially at the grain boundaries, revealing the grain structure. Due to its high vertical resolution, the AFM is able to display contrast between the grains and grain boundaries. The 2-D images created by the AFM for both Type A and B are shown in Figure 15. The resulting images of the grain structure are as accurate as those using plasma etching. The AFM is also able to image 3-D microstructures. The 3-D images of both materials are displayed in Figure 16. From 3-D images, it was found that Si_3N_4 grains polish preferentially on the plane parallel to the c-axis of the hexagonal crystal. Therefore, the polished surface shows that the faces of these vertically oriented rod-like grains have higher altitude (with light color in Figure 16). The information from 3-D images implies that heterogeneous mechanical properties exist in the grain structure. In other

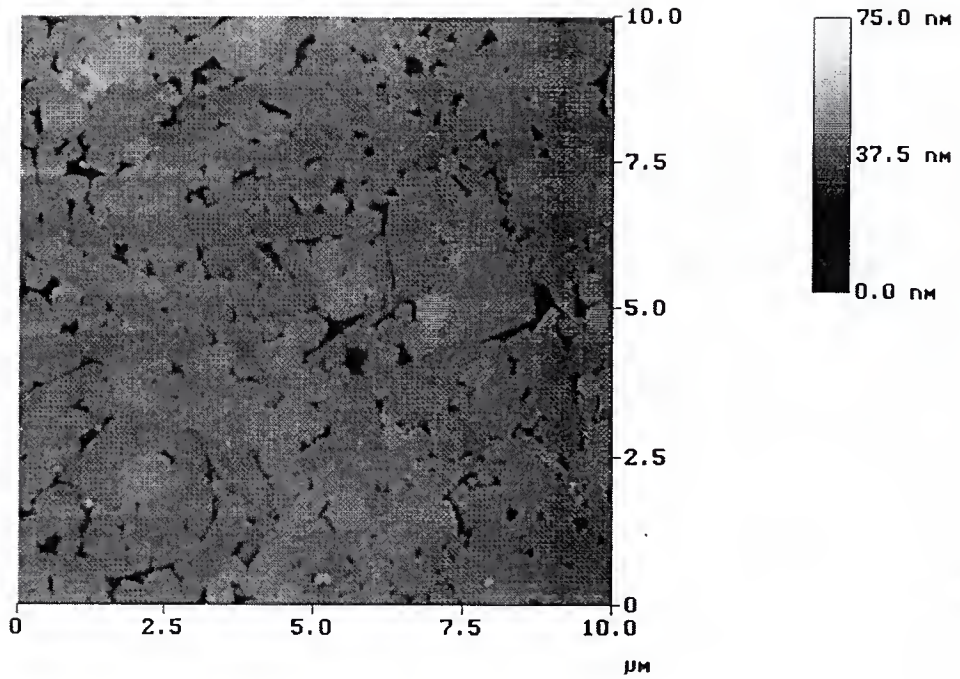

(a)

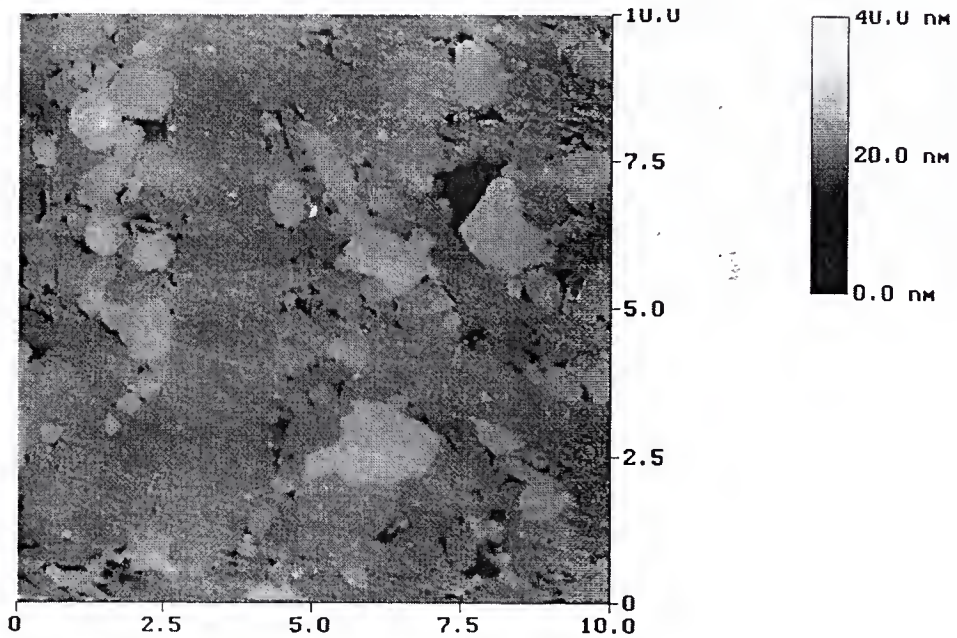

(b)

Figure 15 AFM images of Type A Si_3N_4 microstructure. In (a) Type A microstructure, in (b) Type B microstructure. The resulting images of the grain structure are as accurate as those using plasma etching.

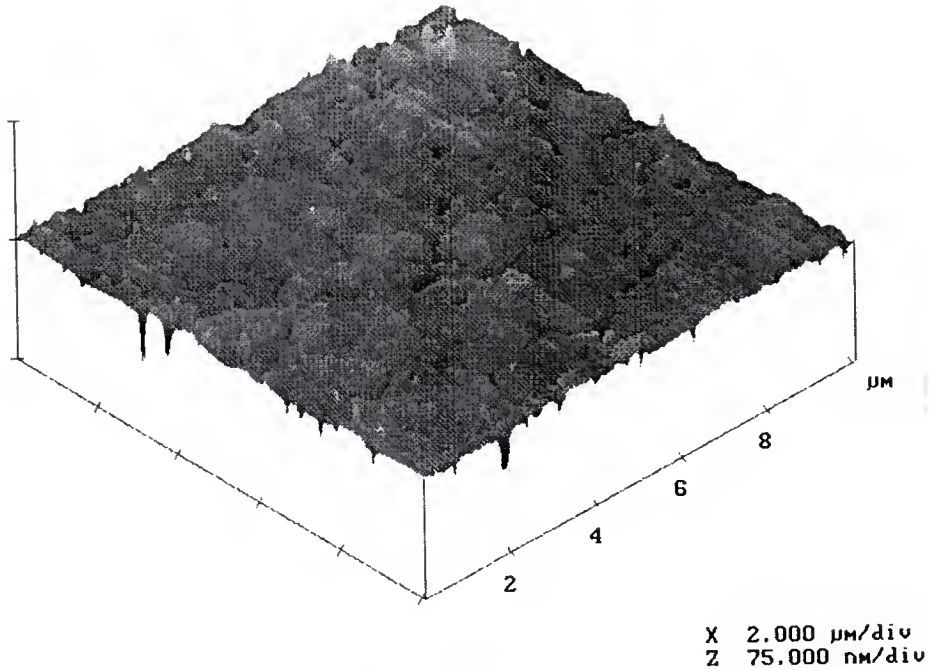

(a)

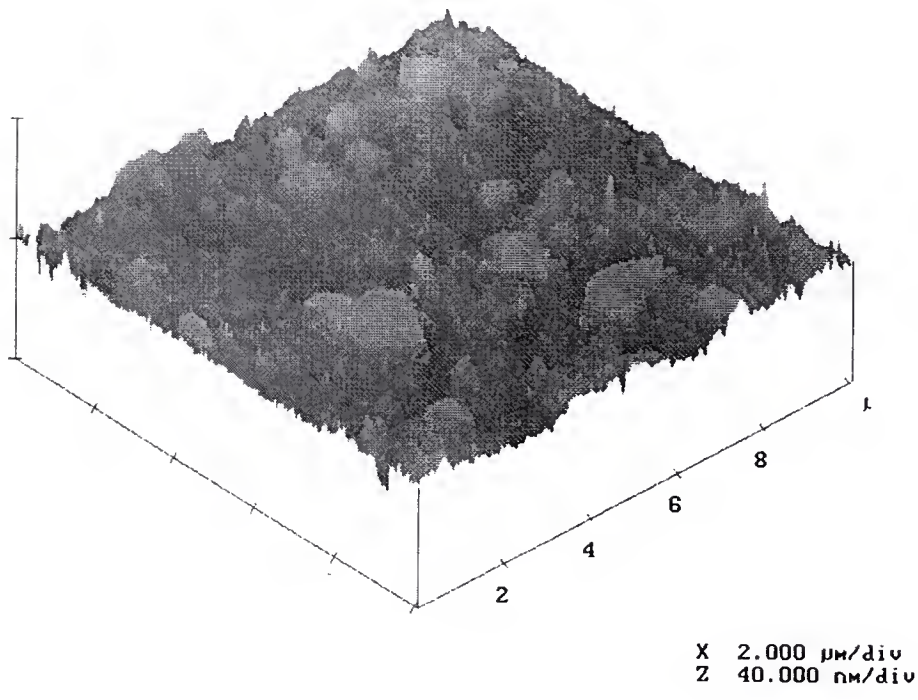

(b)

Figure 16 3-D AFM images. (a) Type A material and (b) Type B material. Preferential polishing in the plane parallel to the base plane of Si_3N_4 hexagonal structure indicates the heterogeneous nature of the crystals.

words, the wear resistance on different crystalline planes of Si_3N_4 would be expected to be different.

From the study of the microstructure, several conclusions can be drawn and are described in this paragraph. Both microstructures of Type A and B consist of rod-like grain structures. Type A microstructure shows that it has more uniform grain size and structure than Type B. Type B has a number of large size grains which disrupt the uniformity and could result in localized residual stress. The sintering phase in Type B is distributed more uniformly in the microstructure than Type A, but Type B also shows that it has a thicker sintering phase along the grain boundaries than Type A. The sintering phase in Type A preferentially concentrates at the triple-points of the grains. The AFM's 3-D microstructural images indicate that different Si_3N_4 crystalline planes have different mechanical properties. The basal plane of hexagonal Si_3N_4 shows a higher wear resistance. The results further imply the heterogeneous Si_3N_4 structures resulting in heterogeneous mechanical properties. The heterogeneity of the grain structure could enhance the mechanical damage due to the mechanical property mismatch when the structure is under a large load. The AFM could provide an additional tool in analysis of material microstructure with a more simple,

quick, and less-expensive way. The AFM microstructural analysis method can be mostly automated and, as such, can rapidly obtain results. 3-D images can be further employed to determine material heterogeneity.

4.2 Fracture Behavior of Si_3N_4

4.2.1 R-Curve Behavior

The fracture strength of Type A silicon nitride was measured as a function of critical crack sizes. The strength data, critical crack sizes, and fracture toughness values are listed in Table 2. In Figure 17 the strength is plotted as a function of critical crack size c. Notably, the function (solid line) shown in Figure 17 does not agree with the function described by equation 2.1. The critical crack size, c, ranged from 6 μm to 800 μm. In Figure 18, optical microscope photos of fracture surfaces with different critical crack sizes are shown. The fracture strength shows a decrease with increase in c. Type A Si_3N_4 exhibits strength sensitivity to crack size. The fracture toughness of Type A was measured with different critical crack sizes. Equation 3.2 was used for the toughness calculation. For Type A, K_{Ic} increases with the critical crack size and displayed the so called "R" curve behavior (Figure 19). The K_{Ic} was found to increase from 5.8 to 10 $MPam^{1/2}$

Table 2 Fracture strength σ_f, toughness K_{Ic} and c/r ratio of Type A material are dependent on the critical crack size c.

c (μm)	r (μm)	σ_f (MPa)	K_{Ic} (MPam$^{1/2}$)	c/r ratio
6.1	/	1887	5.8	/
9.8	/	1489	5.8	/
13.1	187.8	1229	5.5	0.40
16.3	202.3	1117	5.6	0.41
29.5	328.7	856	5.8	0.30
24.0	273.7	968	5.9	0.33
94.4	730.5	611	7.4	0.35
129.2	661.0	574	8.0	0.32
209.9	1001.8	479	8.7	0.34
227.1	1021.8	485	9.0	0.23
298.1	1249.6	466	9.6	0.20
292.8	1247.8	450	9.9	0.21
335.9	1478.3	455	10.3	0.16
336.9	1580.5	456	10.4	0.09
337.5	1352.2	433	9.8	0.09
392.6	1853.5	421	10.2	0.08
387.4	1748.7	413	10.3	0.07
825.4	/	296	10.5	/
817.0	/	283	10.0	/

* r is the mirror size of the fracture surface.

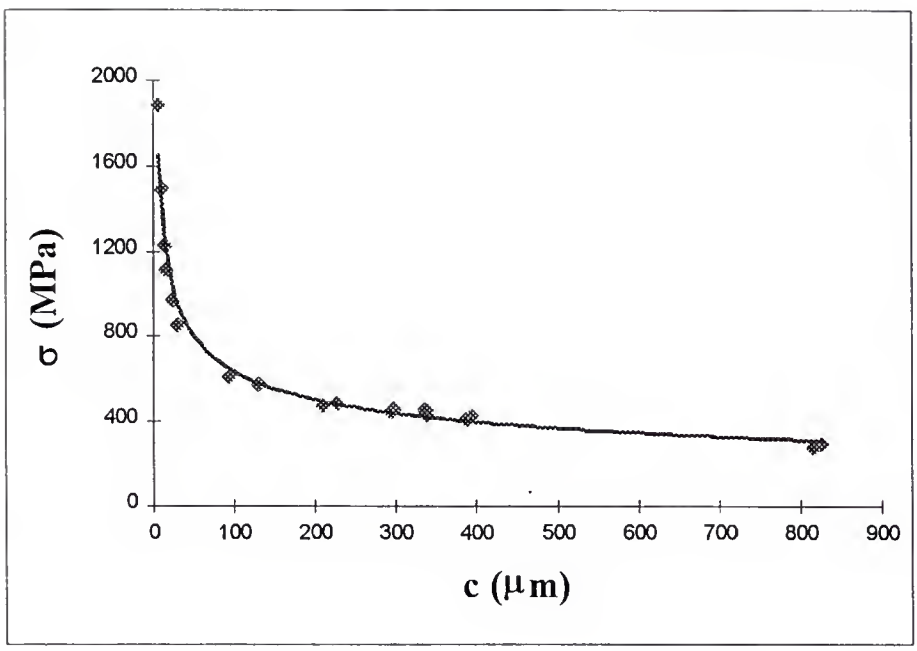

Figure 17 The fracture strength of type A Si_3N_4 is a function of critical crack size, c. However, the function does not follow (the fracture mechanics) equation 2.1. The solid line is a best fit to the data.

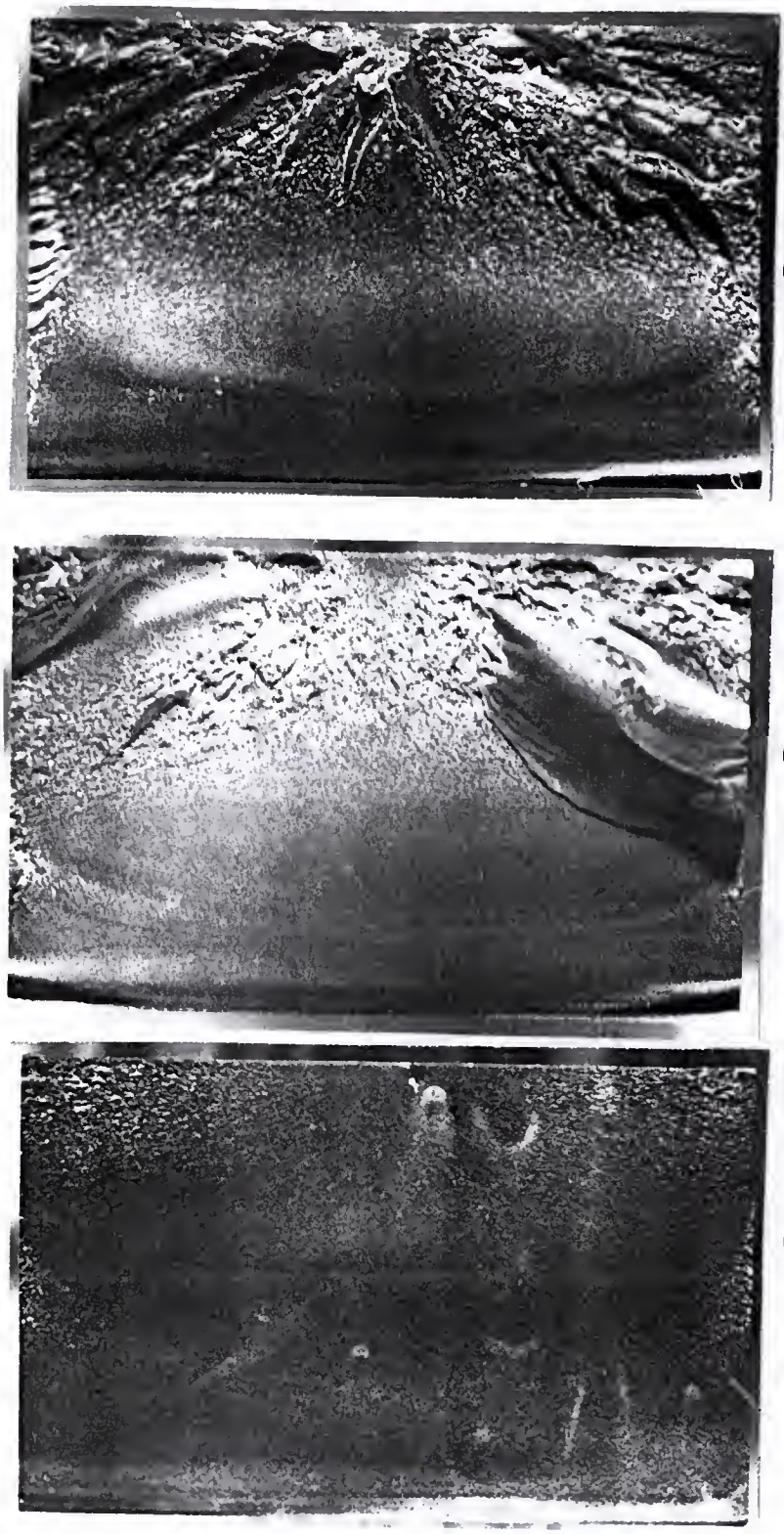

Figure 18 The fracture surfaces of Type A Si_3N_4 show different appearances when the critical crack size increases from small (a) to medium (b) to large (c).

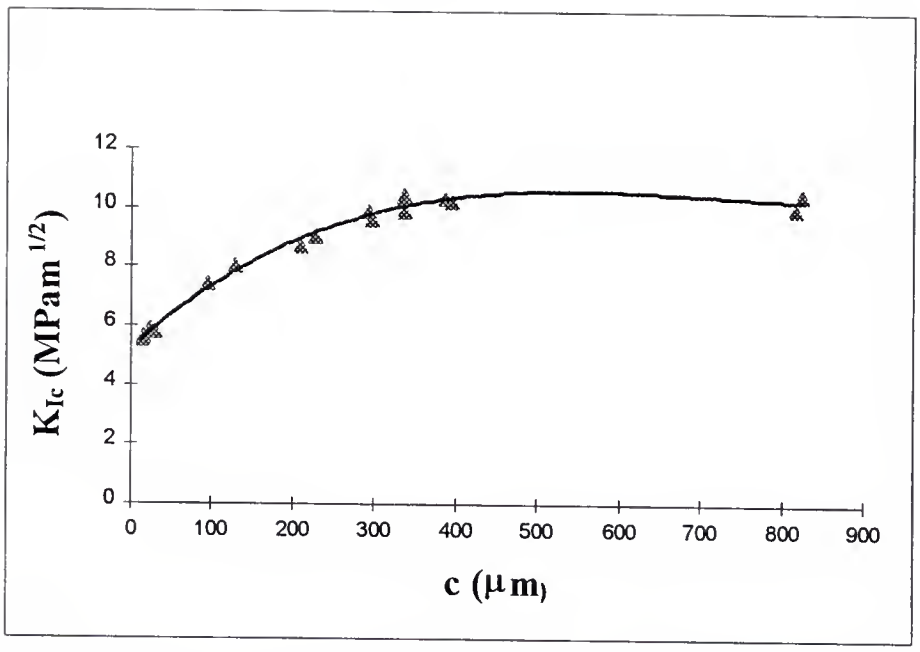

Figure 19 The toughness of type A Si_3N_4 displays "R" curve behavior.

with increasing crack size. This result indicates that the resistance to crack growth increases with increase in initial crack length.

Several studies have proposed possible mechanisms responsible for R-curve behavior in brittle materials[109-112]. Phase transformation, crack-opening microstructural residual stress, elastic grain-bridging, and frictional grain-pullout have been proposed as possible mechanisms for rising crack resistance. From our microstructural study, the silicon nitride bearing material consists of rod-like or "whisker-shaped" grains. These grains grow in randomly oriented directions and are interwoven with one another. This interweaving results in an additional mechanical interlock force causing them to remain in close contact. Since silicon nitride has a very strong covalent bond structure, most of the fracture in silicon nitride is through the grain boundaries. When the cracks start to propagate through the grain boundaries, the crack immediately faces an interlock force among the grains which resists in the grains pulling apart during crack opening. This resistant force is also called a crack bridging force. In Figure 20 a photo of grain bridging in Type A material is shown. Some of the grains are seen to be pulled-out and others fractured during the bridging process.

In order for bridging to occur, a growing crack has to be deflected

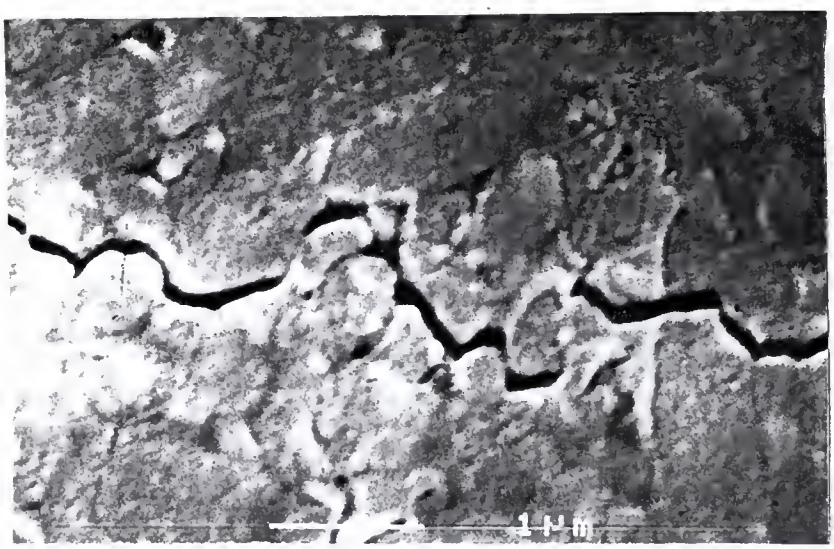

Figure 20 Grain-bridging toughening was found in type A materials.

locally by grains into the grain boundaries. The bridging changes the strain energy release rate ΔG by exerting a closure (bridging) stress on the crack surfaces. The change in strain energy release rate can be expressed by the following equation [113]:

$$\Delta G = 2\int_0^{u^*} P[u(x)]du \tag{4.1}$$

where P[u(x)] is the bridging stress , 2u is the total crack surface opening at a distance x from the crack tip, and u=u* at x=c. If grain bridging occurs in the elastic range, ΔG can be expressed in the following form [113]:

$$\Delta G = \frac{2P_{max}u^*(u^*/u_{max})^n}{n+1} \tag{4.2}$$

where P_{max} is the maximum bridging stress, and u_{max} is the maximum crack-opening displacement that can be supported by the bridging grain at $x=D_b$ (bridging zone size). The value for the constant n can be either 0.5 or 1 depending on whether elastic grain bridging deformation is restricted by grain boundary friction, or elastic grain bridging deformation is continuous until grain fracture or pull-out, respectively. The present experimental observations that elastic grain bridging deformation is restricted by grain boundary friction (n=0.5) is the most common case for Type A and Type B

silicon nitride bearing materials. In terms of a relationship between the critical stress intensity factor K_{Ic} and ΔG, the expression can be written:

$$K_{Ic} = K_o(1+\frac{E'\Delta G}{K_o^2})^{1/2} = K_o(1+4\frac{p_{max}u^{*1.5}E'}{3K_o^2 u_{max}^{0.5}})^{1/2} \quad (4.3)$$

For maximum rising K_{Ic}, $K_{Ic\,max}$, at $c=D_b$ and $u^*=u_{max}$, we have:

$$K_{Ic\,max} = K_o(1+\frac{p_{max}u_{max}E'}{K_o^2})^{1/2} \quad (4.4)$$

where K_o is the material's intrinsic toughness (K_o = 5.8 MPam$^{1/2}$ at the smallest initial crack size), $E' = E/(1-\nu^2)$, E is the elastic modulus of the material, and ν is Poisson's ratio. From this equation, part of the rising K_{Ic} is dependent on the grain boundary strength and grain boundary mechanical interlock force which, in turn, is dependent on the shape of the grains. When the crack length, c, is very small and u^* is close to zero, the K_{Ic} is equal to the intrinsic toughness K_o. With increasing crack size, c, the bridging force starts to play a role in suppressing the crack opening and results in a rising K_{Ic}. When the crack $c = D_b$, and $u^*=u_{max}$, K_{Ic} reaches its maximum. High grain boundary strength and longer interwoven grains produce a high crack bridging force P_{max}. Longer grains and higher frictional forces along the boundary increase the maximum crack opening displacement u_{max}. Both P_{max} and u_{max} help increase K_{Ic} when the crack size increases. From Table 2

and Figure 19, we see that K_{Ic} stays at about 5.8 $MPam^{1/2}$ for a crack size of c=6 μm until the crack gets larger than about 30 μm. For c=30 μm to 335 μm, the K_{Ic} rises at a very steep rate to reach a value of about 10 $MPam^{1/2}$. From then on, K_{Ic} stays at about 10 $MPam^{1/2}$ for a wide range of c. The R-curve behavior also indicates that the grain bridging zone size is about 335 μm. This is because when the crack is less than 30 μm, less than 10% of the grain bridging effective zone acts as a closure stress on the crack surface and no significant bridging occurs to increase K_{Ic}. After the crack increases to greater than 335 μm which is the maximum bridging zone size, K_{Ic} reaches its maximum. Further increase in the crack size does not result in an increase in bridging force and hence there is also no increase in K_{Ic}.

In figure 21, σ_f vs. c is again plotted and compared with σ_f obtained from equation 2.1 (assuming no toughening by bridging), where K_{Ic} = 5.8 $MPam^{1/2}$ (intrinsic toughness) and Y = 1.24. From Figure 21 when c is larger than 335 μm the difference between the two curve is constant ($\Delta\sigma_f \approx 155$ MPa). At this point, $\Delta\sigma_f$ is an estimate of the maximum bridging stress. This value reasonably agrees with the value of 105 MPa calculated by Li [114].

Fracture surface analysis can be used to study the relationship

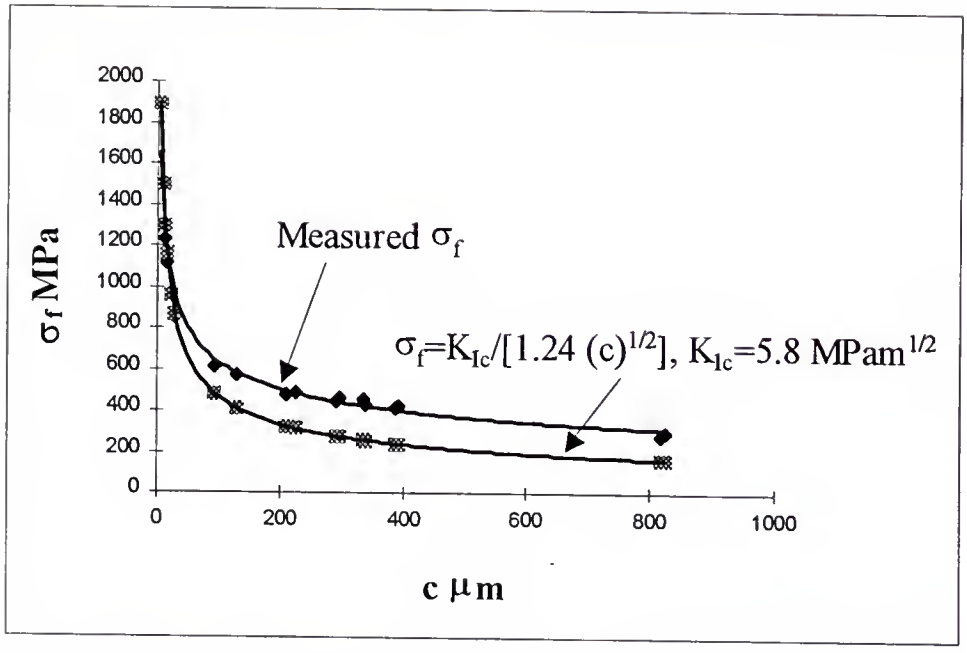

Figure 21 The maximum grain bridging stress can be measured from the difference between experimentally measured σ_f and calculated σ_f (from equation 2.1).

between crack size, crack branching size, and fracture energy. In this study, we found that the ratio of the critical crack size c and mirror boundary size, r, increases with an increase in c (Figure 22). The mirror boundary is where the crack front at some locations starts to deviate from its original crack plane and create more than one crack path [113]. Many criteria were developed to explain the cause of crack branching [115-118]: (1) a velocity criterion in which branching occurs when the crack velocity reaches a maximum value (close to the sound velocity); (2) a critical stress intensity factor criterion in which branching occurs when the stress intensity factor reaches a critical value; (3) a strain intensity criterion requiring that the strain energy available at the crack tip must be sufficient to form two cracks; and (4) a energy criterion [61]. All these criteria have different explanations but indicate crack branching needs a critical energy. However, the study indicates that the c/r ratio is a material constant dependent on material brittleness [117]. This is because K_{Ic} is a constant for glasses and most monolithic ceramics. The present results show that the c/r ratio varies as a function of the crack size. Previously, it was shown that there is an elastic grain bridging stress on the crack surfaces when a crack propagates in silicon nitride. This bridging stress balances part of the applied stress at the

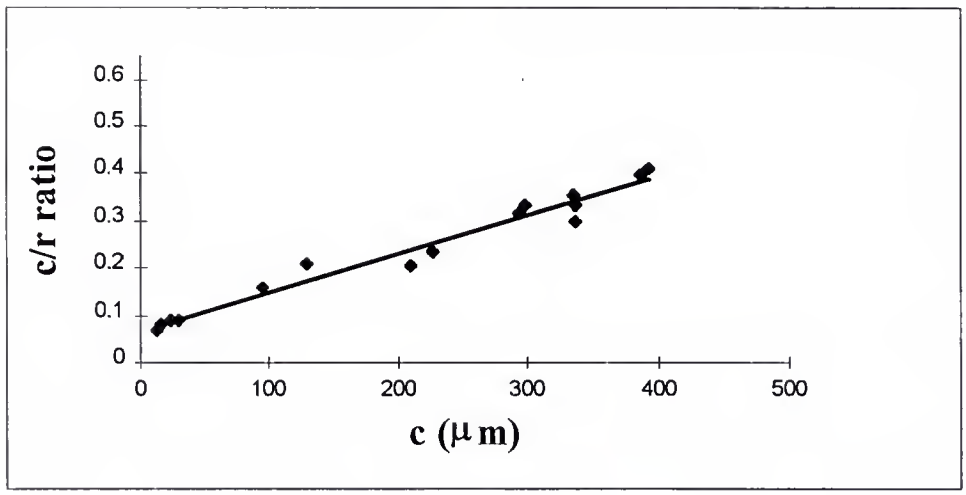

(a)

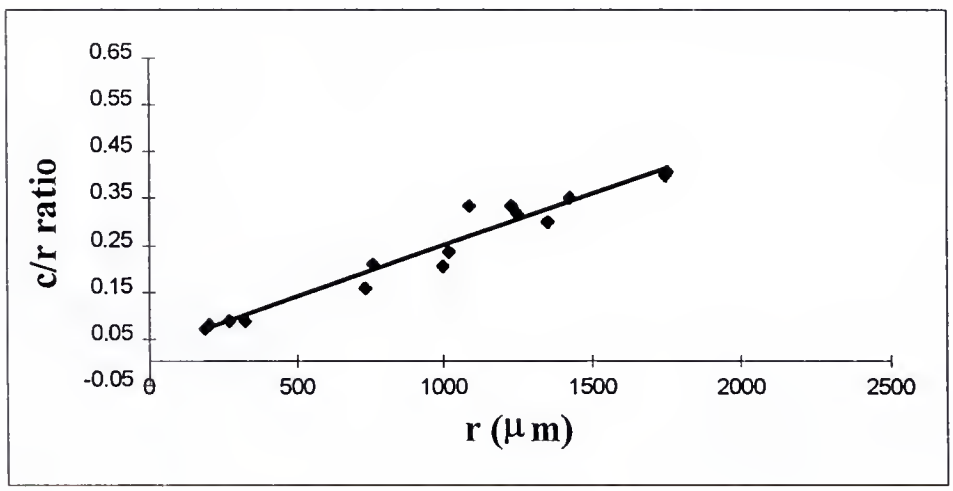

(b)

Figure 22 The ratio of critical crack size c over mirror size r shows a function of c in (a) and a function of r in (b).

crack tip. Extra stress is needed to reach the critical stress intensity factor K_{Ic}, at which crack starts propagation. Therefore, a longer crack has a higher bridging force in suppressing crack opening and hence a higher critical strain energy is needed to drive crack propagation. The grain bridging, therefore, results in K_{Ic} as a function of the initial crack size c:

$$K_{Ic}(c) = Y_c \sigma_f \sqrt{c} \tag{4.5}$$

The stress intensity criterion K_B for crack branching is

$$K_B = Y_r \sigma_f \sqrt{r} \tag{4.6}$$

where failure stress σ_f is the stress that causes the initial crack propagation, and r is the mirror size. The branching starts at the maximum strain energy release rate or at the maximum crack velocity [119]. Since the stress wave velocity is a constant for an identical material, the crack velocity in the material is dependent on the material and the stress level. Therefore, K_B should be a material constant based on equation 4.6. The curve of normalized K_B (K_B^j/K_B^1) versus mirror size r is plotted in Figure 23. K_B^j is one of 15 crack branching stress intensity constant measurements obtained from 15 different fracture surfaces, where the superscript j is equal to 1, 2, etc. up to 15. K_B^1 is one of the K_B^j measured from a pair of σ_f^1 and r^1 values (equation 4.6). The curve in Figure 23 shows a straight line with slope zero

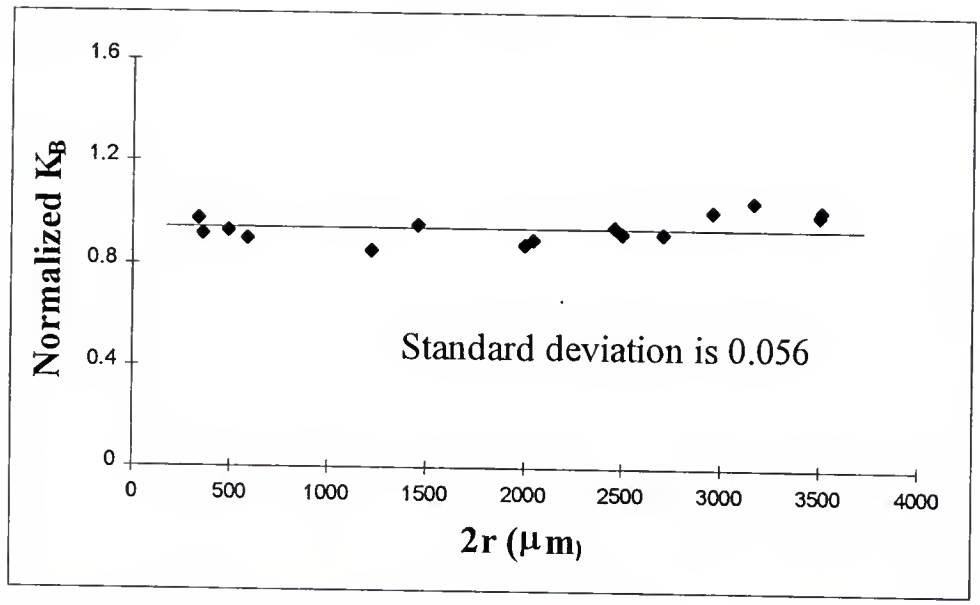

Figure 23 The normalized K_B (K_B^j/K_B^1) value is independent of the mirror size r. This indicates that K_B is a material constant. The standard deviation for the average of normalized K_B is 0.06.

and with a small standard deviation of 0.06. The result indicates that K_B^j is a material constant regardless of the initial crack size. From equation 4.5 and 4.6, we have

$$\frac{c}{r} = Y_{rc}\frac{K_{Ic}^2}{K_B^2} = Y_{rc}\frac{Y_c^2\sigma_f^2 c}{K_B^2} \tag{4.7}$$

where $Y_{rc}=Y_r/Y_c$ is a constant (Y_r is about 1.24 when r is measured along the tensile surface). Since K_B is a constant for the material, the ratio of c over r increases with c. The c/r ratio totally depends on K_{Ic}, which is a function of the initial crack size, c.

Material with a rod-like grain structure can increase the material's capability to resist crack growth. The results of the present experiment demonstrated that Type A material has a rising resistance to the crack growth (R-curve behavior). Its rod-like grain structure acts as a grain bridging stress on the crack faces to suppress the crack opening. However, the R-curve behavior only has effect when the crack length, c, is greater than 30 μm. For small cracks which are usually found in bearing elements, the R-curve behavior has little effect. In fact, localized residual stress could be induced due to material and structural heterogeneity (rod-like grains). In addition, thermal expansion anisotropy around rod-like grains has much

more influence on crack propagation at small size ranges (on the order of a few grains). Therefore, a high aspect ratio of rod-like grain structure may result in a decrease in material strength when small defects or flaws are present in the material. The present research questions whether it is recommended to develop material with R-curve behavior to be used in bearing applications as a trade-off for material homogeneity. This design decision should be considered in the future.

4.2.2 Crack Initiation

High quality silicon nitride is now being manufactured in which large pores and inclusions are nearly eliminated. The question is: "what major factors (if not large defects) cause material failure under fatigue loading?" Fracture mechanics provides a theoretical basis for fracture analysis in brittle materials. However, without fractographic analysis, the theory and failure analysis will be handicapped, especially for materials which fracture catastrophically after a number of loading cycles. In this case, the use of fracture mechanics alone to conduct failure analysis is difficult. The following experiment was the result of a collaboration with Torrington Co. which performed the rotating cantilever beam preparation and rotating

cantilever beam fatigue tests. Two types of materials, Type A and Type B, were tested. Failure origins were found in ten out of 30 samples. Failure origins were difficult to identify in the rest of the samples because of material loss during fracture. All of the 10 failures initiated internally from regions rich in sintering phase material. No specimens were found in which failure was initiated by surface defects. Figure 24a shows a typical Type A failure origin. EDS identified that the Type A failure origin is rich in Y, Al, and O (Figure 24b). For Type B samples, most of the origins were difficult to identify due to material loss. This is because the Type B microstructure consists of irregular-shaped grain with a wide range of sizes. The microstructure seems to lack the mechanical interlock forces among the grains and evidently results in surface grain pullout after fracture. This phenomenon is surmised because of missing grains on the fracture surface. In Figure 25, the photo of the Type B fracture surface shows some fracture debris and loose grains on the surface. From some fracture surfaces, the region from which the crack started was identified as a Mg and O rich region.

From the failure analysis, all the failures initiated in a glassy (sintering) phase rich region. This observation indicated that slow crack

(a)

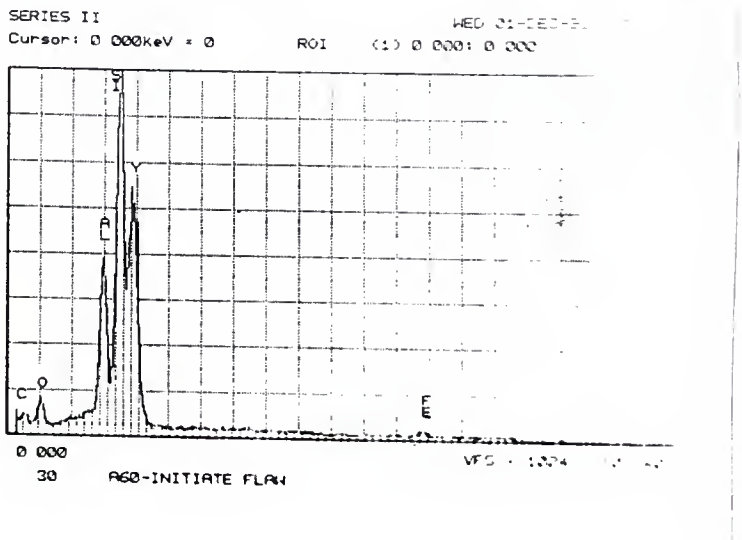

(b)

Figure 24 A typical failure origin of Type A materials (a), EDS spectrum displaying the composition in the failure origin (b).

Figure 25 SEM photo showing a typical failure origin of Type B Si_3N_4 rich in Mg and O.

growth may have occurred in the glassy phase rich region under fatigue loading. The crack growth rate in the glassy phase region is dependent on the stress level at its location and the amount of moisture (H_2O molecules) around it. The OH^- ions or H_2O molecules may exist in the material or diffuse into the material from the outside surface. The crack growth rate, v, can also be described as a function of stress intensity factor, K_I, by the following equation[120]:

$$v = \alpha' \exp(-\frac{\Delta H}{RT}) K_I^n \tag{4.8}$$

where α' is a constant, ΔH is the activation enthalpy of the reaction between the glassy phase and water molecules, T is the temperature, R is Boltzmann's constant, and n is a material constant which determines the material sensitivity for slow crack growth. ΔH is generally found to be temperature independent. For most of the oxide ceramics, n is a value in the range of 10 to 20, e.g., n=16 [120] for alumina.

Crack growth rate depends not only on the stress intensity factor but also on environmental factors such as the amount of moisture. Under a load, crack growth in the material starts very slow at low K_I because of the small initial flaw size. The crack growth rate for pure Al_2O_3 in 50% humidity air

is less than 10^{-11} m/sec under a 800 MPa stress. We assume that the initial flaw size, c, from which the crack growth starts is 1μm, or about half the grain size. The crack growth increases with K_I due to an increase in flaw size. After the crack grows to a critical size, which depends on the local toughness, catastrophic fracture occurs. From one of the fatigue fracture surfaces (Figure 26a), the fracture appearance is similar to a monotonic fracture surface (Figure 26b). The resulting failure analysis indicates that fatigue fracture in silicon nitride materials is a process which consists of a slow crack growth for a small distance in the glassy phase and then monotonic fracture when the stress intensity factor reaches a local critical stress intensity factor.

Since most of the critical flaw sizes are very small (≤18 μm), it is difficult, if not impossible to measure them under an optical microscope due to the limitation of the depth of field. The mirror boundary on the fractured specimens appears clearly when visible white side light is properly directed to the surface. The critical flaw size, c, was obtained from the c/r ratio using the measured mirror radius, r. The c/r ratio is a function of r as shown in Figure 22b. Using this method, the critical flaw size, c, of each fracture surface was determined. The failure stress was calculated based on the

(a)

(b)

Figure 26 (a) A fatigue fracture surface is similar to (b) a monotonically loaded fracture surface.

failure origin location y (distance between the origin and tensile surface) using the equation:

$$\sigma_f = \frac{M(R-y)}{I} \tag{4.9}$$

where M is the bending moment, I the moment of inertia of the specimen, and R the radius of the cantilever beam at the fracture location (equal to 2.4 mm). The local critical stress intensity was calculated using the formula for an embedded initial crack[121]:

$$K_{Ic} = \sqrt{\pi}\sigma_f \sqrt{\frac{a}{Q}} \tag{4.10}$$

where Q is the flaw shape parameter (equal to 1.35 when the ratio of a/2b is 0.3). Equation 4.10 can then be expressed as:

$$K_{Ic} = 1.18\sigma_f \sqrt{c} \tag{4.11}$$

The fracture surface analysis data are given in Table 3. The local critical stress intensity was found to be about 3.4 $MPam^{1/2}$ which is much smaller than the toughness (about 5.8 $MPam^{1/2}$) measured using indentation. The results indicate that the materials prefer to fail from the lower local critical stress intensity (K_{Ic}) region. The region with the lowest local K_{Ic} in the material is the region rich with a glassy phase. Both the low toughness of the glassy phase and the local residual stress due to heterogeneous

Table 3 Fracture surface analysis data for rotating cantilever beam fatigue test.

Sample	σ_{max} (MPa)	# of failure cycles x10^3	y (μm)	r (μm)	σ_f (MPa)	c (μm)	K_{Ic} (MPam$^{1/2}$)
A7	686	349.2	400	194	572	14	2.5
A11	849	42.3	22	163	841	11	3.4
A60	800	43902.3	96	180	768	13	3.2
A61	649	39964.2	284	269	572	18	2.9
A69	848	20945.9	39	155	834	11	3.2
B23	823	40278.3	27	156	814	11	3.2
B26	832	53058:6	34	155	820	11	3.2
B39	826	30511.4	46	198	810	14	3.6
B48	774	8.9	15	185	769	13	3.3
B49	833	26533.9	16	146	827	10	3.1

* σ_{max} is the maximum stress on the tensile surface of the beams.

** y and r are the distance between the origin and the tensile surface and the mirror size, respectively.

*** σ_f is calculated the failure stress at the failure origin.

\+ c is calculated the critical flaw size based on c/r ratio.

++ K_{Ic} is measured local toughness.

mechanical behavior may contribute to material failure at low stress intensity levels.

This experiment clearly demonstrates that the local toughness of the material determines the failure stress under cyclic loading. The fracture surface analysis explained why materials always appear to fail at low stress during fatigue loading.

The failure origins for both materials were identified using SEM and fracture surface analysis. The crack initiated through a slow crack growth process in the region rich in glassy phase. Catastrophic fracture occurred when the stress intensity of the growing crack under cyclic fatigue loading exceeds the local K_{Ic}. The location of the failure origin is dependent on the size of glassy phase and the stress level in this region. No fatigue fracture marks were found on the fracture surfaces in this experiment. Slow crack growth was limited to a small region and then monotonic fracture takes over the fatigue crack growth. The critical crack size and local fracture toughness in the failure origin region can be determined using fracture surface analysis by measuring the crack branching radii.

4.3 Contact Fatigue

In Figure 27b, an SEM photo shows the Si_3N_4 wear pattern that was caused by the ball on disc fatigue test. A typical silicon nitride bearing ball wear pattern caused by a bearing test is shown in Figure 27a. The wear pattern in Figure 27a was caused by multiple contact fatigue damage, the wear pattern in Figure 27b was caused by single contact fatigue damage. Regions 1, 2, and 3 in Figure 27a exhibit a similarity to Hertzian cone type fracture that is shown in region 4 of Figure 27b. It is concluded, then, that the ball on disc contact fatigue testing method is appropriate for use in studying silicon nitride material wear mechanisms in hybrid bearing systems.

The ball on disc contact fatigue test data are listed in Table 4. The wear process observed in these tests basically consisted of three different stages (Figure 28): roughening of the contact surface (Stage I), cone crack initiation and propagation (Stage II), and large volume of material removal from outside the contact area (Stage III). In the following sections, each stage of wear will be discussed and the mechanisms of wear will be proposed.

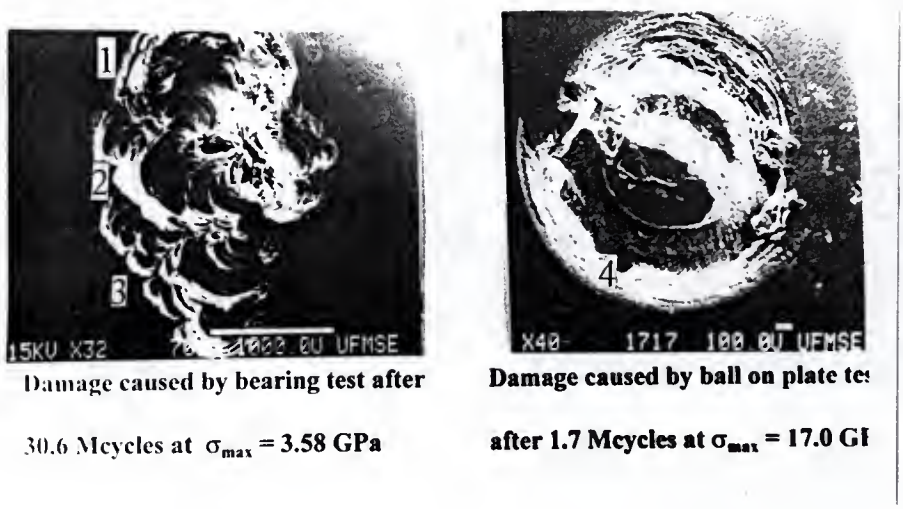

Damage caused by bearing test after 30.6 Mcycles at σ_{max} = 3.58 GPa

Damage caused by ball on plate te: after 1.7 Mcycles at σ_{max} = 17.0 GI

(a) (b)

Figure 27 (a) A type hybrid bearing ball failure pattern and (b) a Hertzain contact failure pattern from the ball on disc contact fatigue test. Both of them show some similarity in the egions labeled with the numbers such as 1, 2, 3, and 4.

Tbale 4 Data from the ball on disc contact fatigue test.

Si_3N_4 Type	σ_{max} (GPa)	Hz	# of cycles (k)	Total time (hr.)	Damage Description
A	10	10	1500	26.4	few grains pull-out, cone-crack
A	15	10	600-1500	11.1-26.4	few grains pull-out, cone-crack
A	15	10	2000	55.5	cone-crack, chip-out
A	15	10	3000	83.3	large volume loss
A	17	10	20	0.6	few grains pull-out, cone-crack
A	17	10	1700	47.2	large volume loss
A	20	10	1	0.03	cone-crack, chip-out
A	15	7	700	27.8	cone -crack
A	15	5	500	27.8	cone-crack
A	3.5	10	5000	138.9	grain pull-out, cone-crack
B	15	10	500	13.9	grain pull-out
B	15	10	1000	27.8	grain pull-out, cone-crack
B	15	10	2500-3000	69.4-83.3	large volume loss
B	3.5	10	5000	138.9	grain pull-out, cone-crack

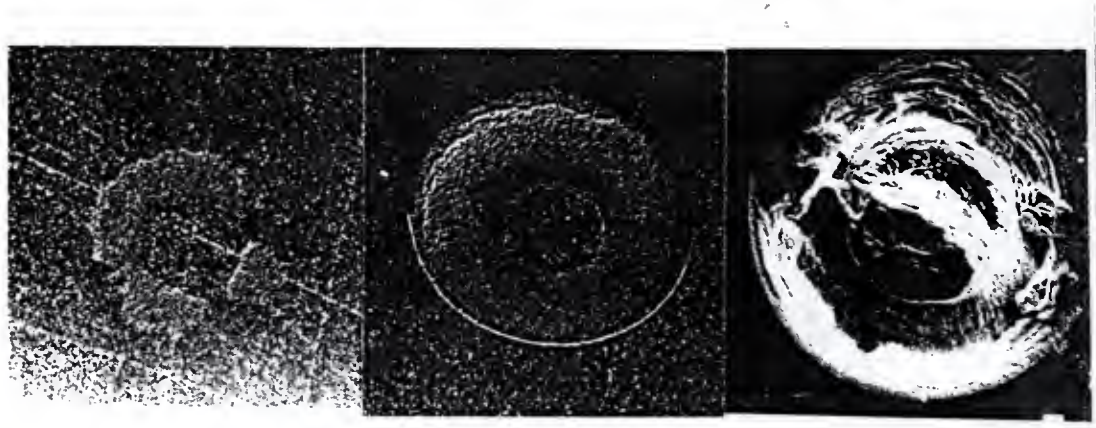

Stage I Stage II Stage III

(a) (b) (c)

Figure 28 Wear due to the ball on disc contact fatigue test consists of three different stages: (a) wear at Stage I, (b) wear at Stage II, and (c) wear at Stage III.

4.3.1 Stage I Wear-Roughening on the Contact Surface

The Type A specimen was tested under a 3.2 GPa maximum stress at 10 Hz frequency. Figure 29a is the wear pattern after 5 million loading cycles. The plot of roughness vs. its corresponding location on the contact surface is shown in Figure 29b. Each location is represented by a letter A, B, C, or D, respectively, corresponding to the location shown in Figure 29a. An increase in the contact surface roughness indicates that wear has occurred. For convenience in later discussion, the middle of the contact surface (labeled with a letter A in Figure 29a) was designated as the central region. The roughest area just outside the middle contact area was called the outside central region (labeled with a letter B). The contact area was examined under high magnification SEM. In the central region (Figure 30a), most of the grain boundaries were damaged and a few grains were pulled out from the surface. Away from the central region, many more grains were lifted up in the outside central region shown in Figure 30b.

For theoretically dense brittle materials with covalent or ionic bonds, it is difficult to fracture under a hydrostatic compression. This is because none of three fracture modes in fracture mechanics can explain fracture under hydrostatic compression. The questions raised here are: why

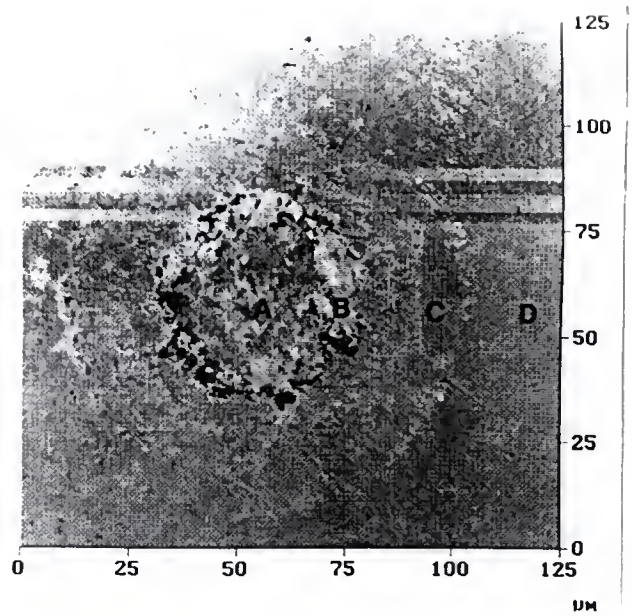

(a)

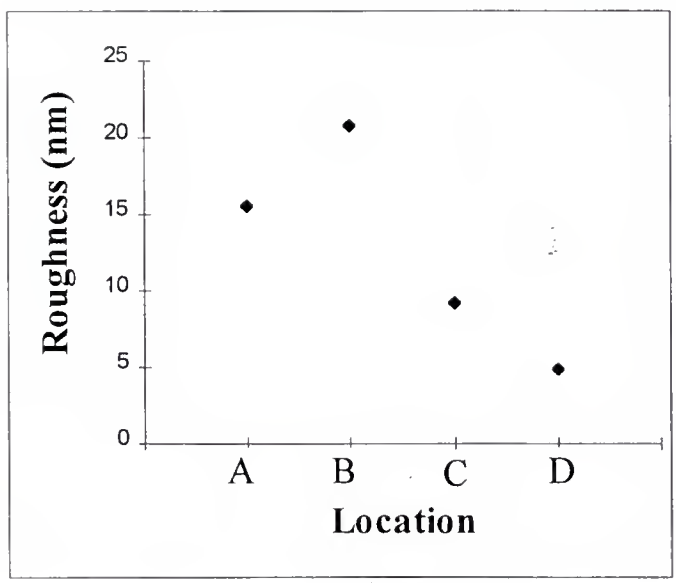

(b)

Figure 29 (a) is AFM image resulting from a wear surface. (b) is a plot of surface roughness vs. different locations on the contact surface which is corresponding to the location labeled in (a).

(a)

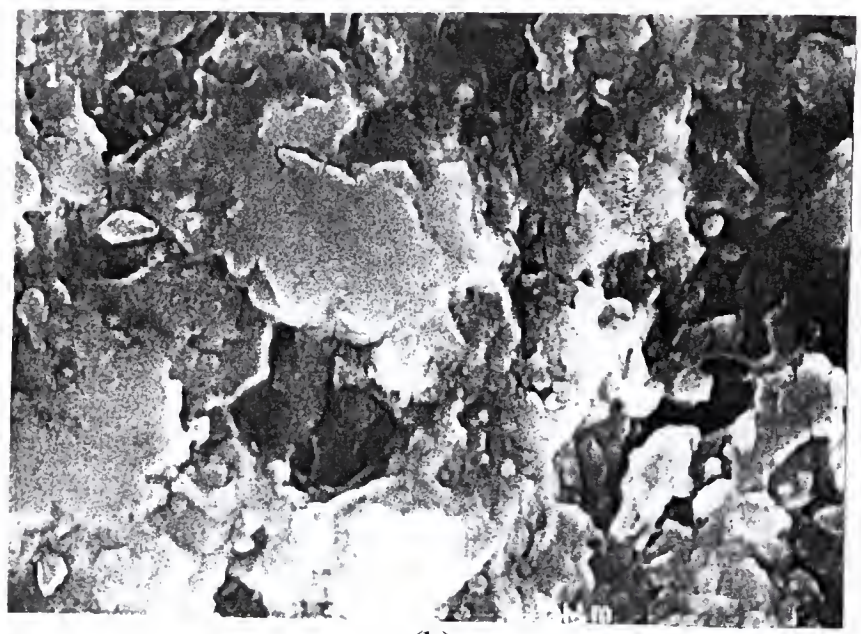

(b)

Figure 30 Wear surface topography, the picture in (a) shows wear at the central region and the picture (b) wear at the outside central region.

are the grain boundaries damaged under a compressive stress and why are fewer grains pulled out in the central contact region than in the outside central region?

First, damage of the grain boundaries under the compressively loaded region was observed. The existing grain boundary phase is recognized as a glassy phase which was used to improve Si_3N_4 densification during the sintering process. The boundary phase in Type A is mainly composed of Al_2O_3, Y_2O_3, and SiO_2; in Type B it is MgO and SiO_2. The glassy or amorphous materials are always susceptible to structural rearrangement under stresses because of their long range disordered structure or disordered network structure [122]. Therefore, there is a delayed elastic deformation of the glass phase in response to a load due to disentangling of structural elements, such as rings and chains of atoms [123]; this is called viscoelastic behavior. De Bast and Gilard [124] studied the viscoelastic behavior of a stabilized soda-lime-silica glass. The specimens were loaded in compression in a testing machine equipped with a specially designed extensometer. The delayed elastic component can be represented by a generalized Kelvin-Voigt model:

$$\varepsilon_d = \varepsilon_\infty[1 - \exp(-a_1 t)^b] \tag{4.11}$$

where a_1 and b_1 are the constants depending on temperature, and ε_∞ a deformation. The schematic curves in Figure 31a show the relationship between loading and deformation for both glassy material and polycrystalline materials, respectively. The glass mechanical behavior is represented by springs and dashpots; Si_3N_4, a polycrystalline material, is represented by a spring. Si_3N_4 deformation responds to the loading immediately, whereas the glass deformation shows an immediate response (elastic) and a delayed response (viscous) to the loading. The delayed response results from that the glassy structural units gradually entangling each other during unloading. This "entangling action" causes a time-dependent change in volume manifested as the delayed deformation.

Finding an exact solution for the delayed deformation of the sintering phases is difficult due to many unknown mechanical properties, such as the values of Young's modulus and viscosity as well as the precise composition of the glassy phases. However, studies of mechanical behavior in glassy materials have shown that viscoelastic behavior exists in glass [123]. Viscoelasticity originates from internal friction occurring in long-range disorder in the structure under stresses. The delayed time τ is expressed by Nowick and Berry's equation [125]:

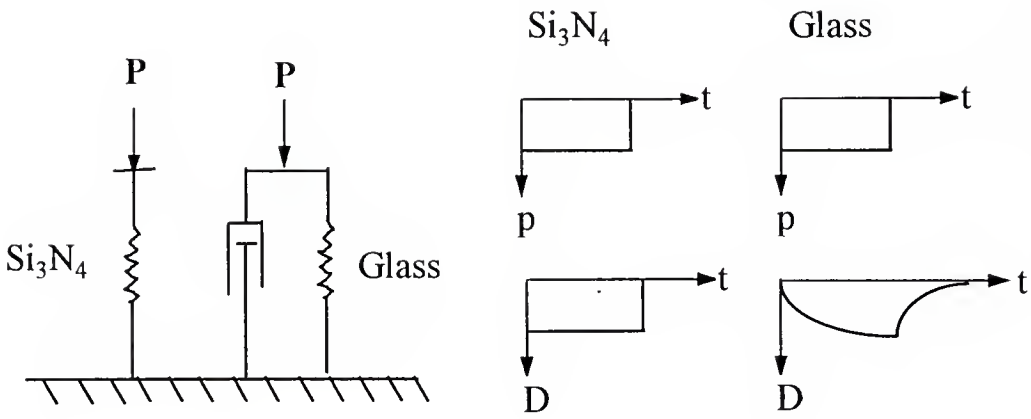

(a)

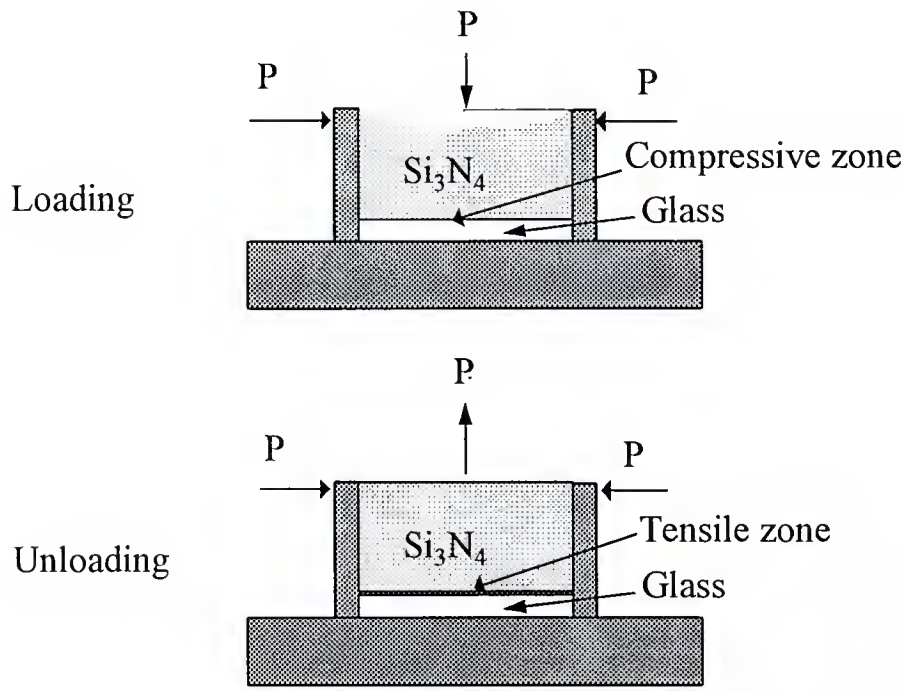

(b)

Figure 31 (a) Kelvin-Voigt solid model and its load-deformation curve. (b) Schematic showing tensile stress built along the grain boundary due to delay deformation in the grain boundary phase.

$$\tau = \frac{h}{kT}\exp(-\frac{\Delta S}{R})\exp(\frac{\Delta H}{RT}) \qquad (4.13)$$

where ΔS and ΔH are the entropy and the activation enthalpy of the glassy structure, respectively. An internal friction spectrum for the glass $3SiO_2{\cdot}Na_2O$ was shown in reference [123]. The first friction peak at about -32 °C corresponds to a migration of the alkali metal ions under stress. The second, near 182°C, has been associated either with the oscillations of non-bridging oxygen ions or with the presence of hydroxyls (OH) in the structure. Each of the peaks emerging from a continuum represents viscoelastic effects.

The sintering phases in Si_3N_4 consist of a long-range disorder glassy structure. Near the surface, hydroxyls(OH), due to moisture in the environment, can easily enter the glassy phases. The existence of viscoelastic behavior in the sintering phases due to internal friction is obvious. Therefore, when a compressive load P on a silicon nitride grain is released (Figure 31b), the grain is immediately back in its original position; whereas the glass phase along the boundary is gradually returned to its original position due to an entangling action happening among its glassy structural units. A tensile stress is built in the glass phase due to the glass

phase's delayed deformation during the unloading cycle. The cyclic tensile stress in the glassy phase eventually causes grain boundary fracture. However, if there is no tangential traction to lift up the damaged grains from the contact surface, the grains will still remain in their position due to the grain boundary mechanical interlock.

Now, why are fewer grains pulled out in the central contact region than in the outside central region? To answer this question, first, it is necessary to examine the shear stress distribution to see if there is any stress difference between these areas. The shear stress distribution in the xz plane is shown Figure 32. A higher surface tangential traction was found on the outside central region. This traction is primarily due to Young's modulus and Poisson's ratio mismatch between the ball and the disc during the contact loading. So, the traction lifts up the grains whose boundaries have been damaged. In the central region, most of the grains still remain in their position because of the low tangential traction.

Stage I wear, therefore, can be described using the model shown in Figure 33. There is a different deformation response to the loading and unloading cycles between the grain and grain boundary phase. In addition, the constraint force on the surface is decreased due to the free surface. Both

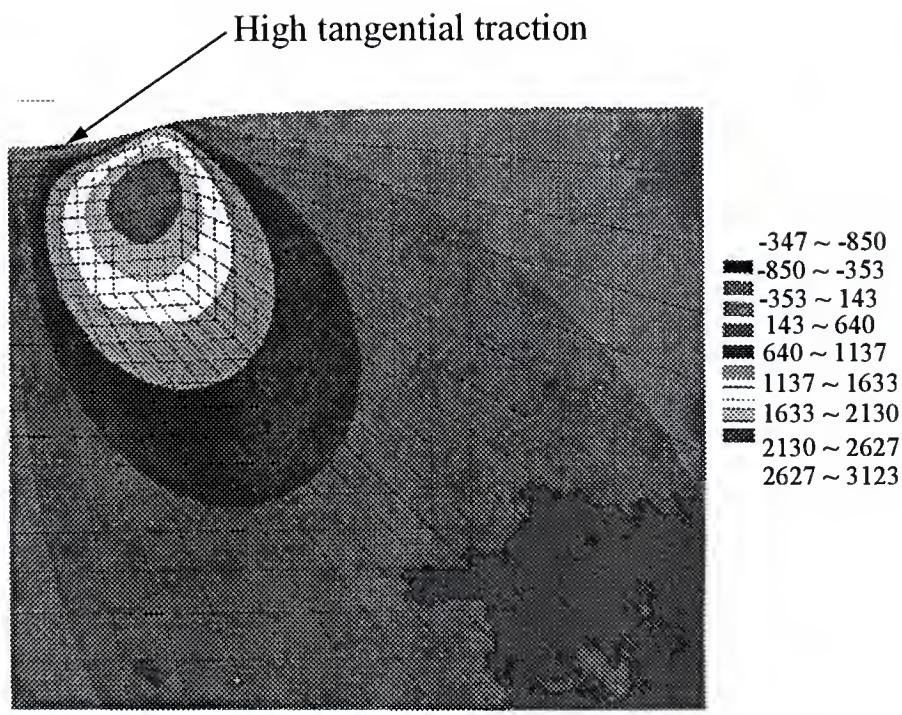

Figure 32 Hertzian shear stress distribution in xz plane within a range of x=1000 mm and z=865 mm. Notice, a high tangential traction exits at the outside central region.

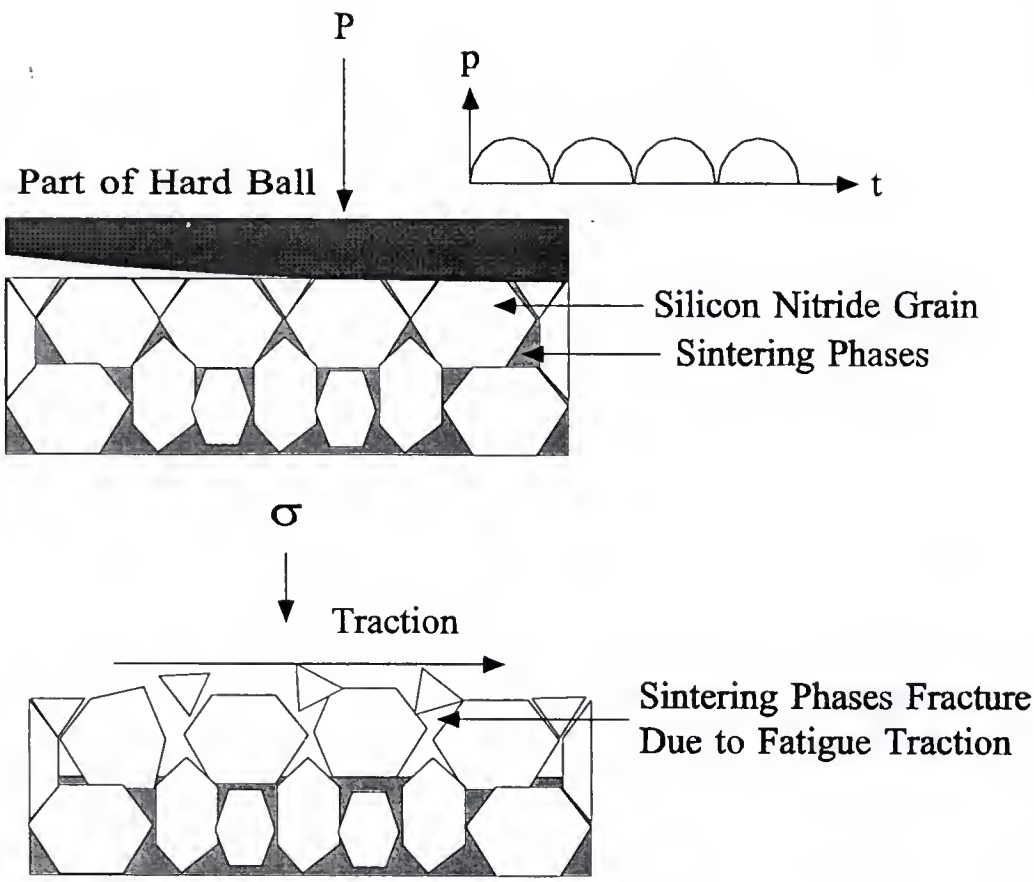

Figure 33 Schematic showing the mechanism of wear in stage I. Grain boundary phase is damaged due to its delayed deformation under cyclic loading. Grain pull-out is caused by the surface tangential traction.

of these factors cause fatigue damage along the grain boundaries near the surface. Then, the grains whose boundaries have been damaged are pulled-out by the tangential traction. The wear initiation is due to heterogeneous mechanical behavior between the grain and grain boundaries (elastic behavior versus elastic and viscoelastic behavior). Wear development is attributed to the tangential traction on the contact surface which lifts up grains from the surface.

To verify this explanation, a contact fatigue load was applied to a homogeneous material, borosilicate glass, to investigate if any damage occurred in the contact area. From the picture shown in Figure 34, it is obvious that the contact area remains intact after 6000 loading cycles and under a 2.5 GPa maximum contact stress. The result clearly demonstrates that a homogeneous structure can eliminate Stage I wear on the contact surface. In other words, this experiment confirmed that the heterogeneous mechanical behavior in the silicon nitride material and the grain boundary phase is the cause for Stage I wear.

Figure 34 Homogeneous borosilicate glass shows no wear in the contact area under cyclic contact stress.

4.3.2 Stage II Wear-Cone Crack Initiation and Propagation

Considering the bond structure of brittle materials, i.e., covalent or ionic bonding, the Mode I stress is a basic stress mode that causes brittle material fracture. From the contact stress distribution in the lateral direction (Figure 35), there is a maximum tensile stress just outside the circumference of the contact area. The surface of the specimens has been carefully polished down to a surface roughness less than 6 nm. We assume that there are no pre-existing cracks in the surface (or at least, we can assume there are no pre-existing sharp cracks). For crack growth, the first step is to initiate a sharp crack. The following discussion will be focused on crack initiation in the tensile region.

The SEM photos taken from a wear area are shown in Figure 36. There appears to be a cone crack near the maximum tensile region in Figure 36a. However, under higher magnification, it was identified as a loose grain region (Figure 36b). Other pictures (Figure 37) also display loose grains and pulled-out grains near the maximum tensile region. After grains loosen and are pulled out from the surface, a crack initiates from the pulled-out grain region. The crack then propagates under a cyclic stress in Mode I. A model in Figure 38 is used to explain the cone crack initiation and propagation in

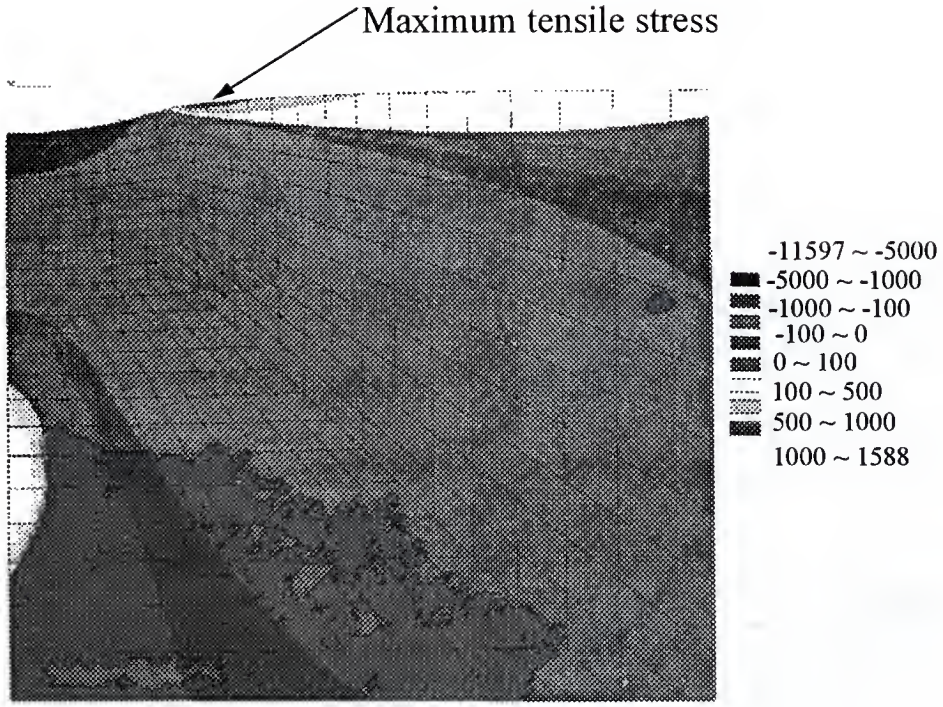

Figure 35 Hertzian stress distribution in x direction within a range of x=1000 mm and z=865 mm. Notice, there is tensile stress field just outside contact area.

(a)

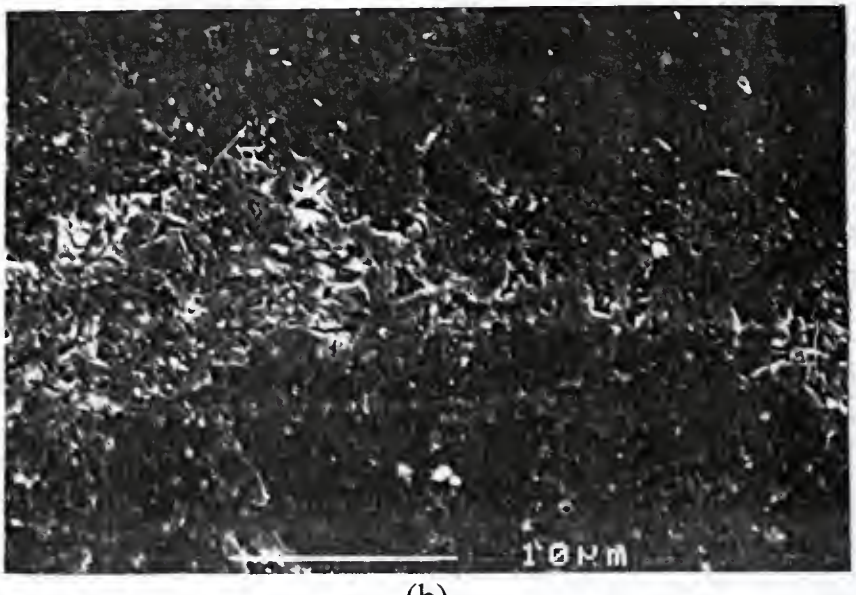

(b)

Figure 36 (a) The cone-crack seems to be initiated near the maximum tensile stress region. (b) High magnification SEM shows the cone-crack is a grain loose region.

(a)

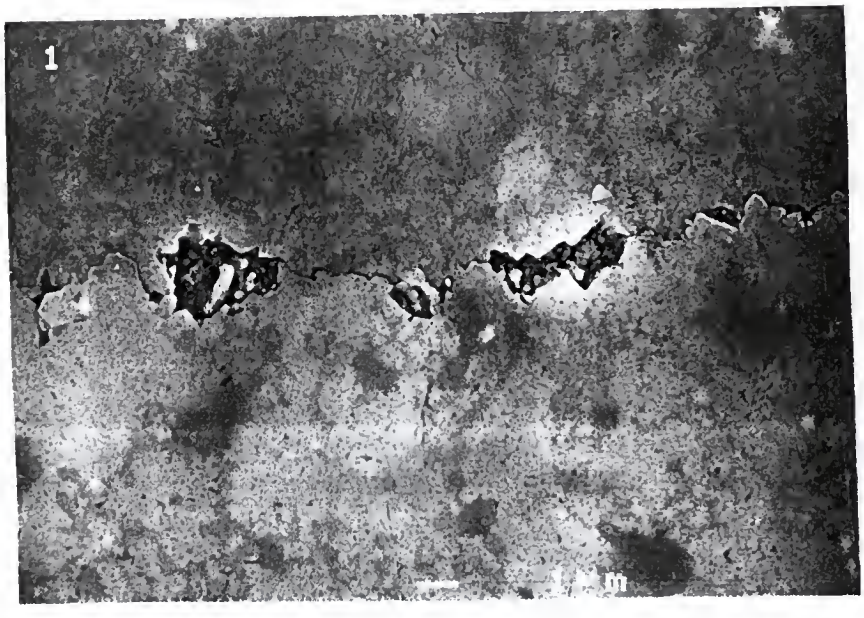

(b)

Figure 37 (a) The cone-crack was initiated near maximum tensile stress region. (b) High magnification SEM shows the loose grains and pull-out grains at the maximum tensile region.

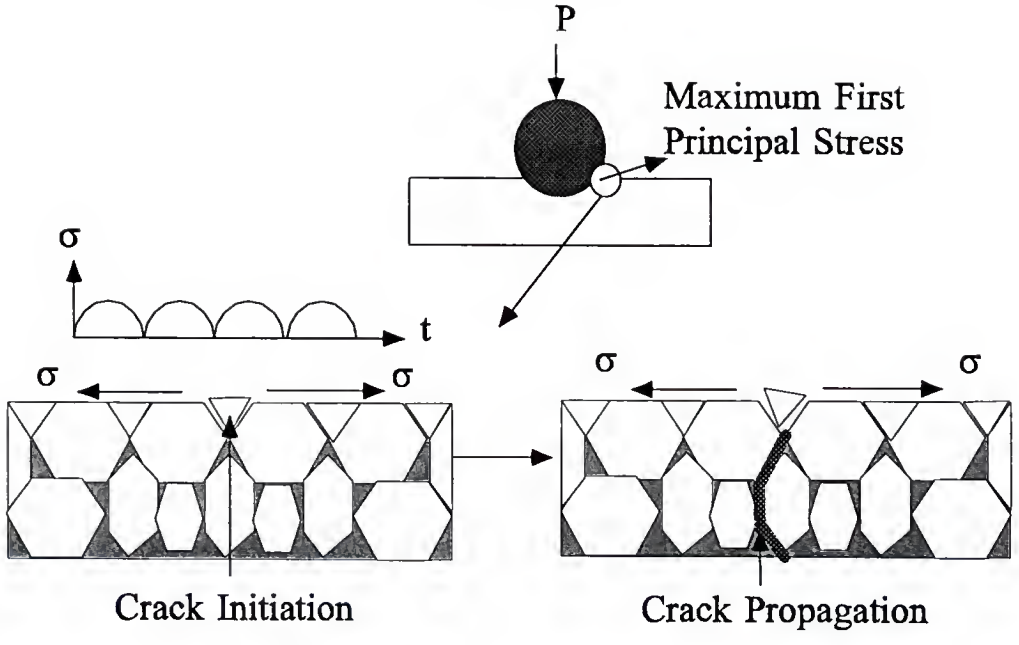

Figure 38 Schematic showing the mechanism of wear in Stage II.

the maximum tensile stress region under cyclic contact fatigue. The material just outside the contact area circle experiences a maximum (cyclic) tensile stress. The cyclic stress causes fatigue damage in the grain boundary phase near the surface due to its weak mechanical properties, i.e., low strength, low toughness, and environmental sensitivity. The loose grains near the surface at the maximum tensile region, which are caused by boundary phase fatigue, result in cone-crack initiation. The crack then propagates stably along the grain boundary under a cyclic Mode I stress. Again, the weakness of the grain boundary phase and the existence of the tensile stress outside the contact area are two major factors which result in Stage II wear: Stage II wear is a cone crack initiation and propagation process.

Another phenomenon which occurred during Stage II wear is the initiation of multiple-cone cracks in outside the contact area. A SEM photo in Figure 39a shows multiple cone-cracks from a cross section of the contact area. From the cross section, the first cone-crack, which is closest to the contact circumference has the longest length. The length of other cone-cracks decreases with an increase in distance between the cone-crack and the circumference. The first cone crack determines Stage II wear, and the following cone-cracks enhance Stage II wear.

(a)

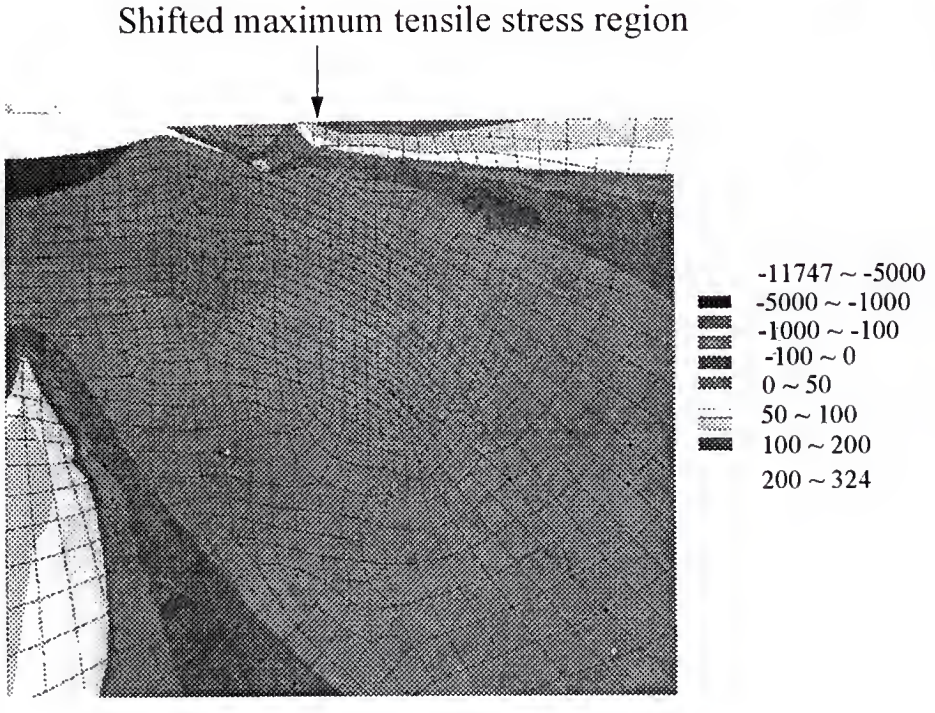

(b)

Figure 39 (a) SEM photo shows multiple cone-cracks outside contact area. (b) Hertzian stress in the lateral direction is redistributed due to existing crack.

A FEA program was used to analyze the stress distribution after the first cone crack was initiated (Appendix A). The stress distribution along the lateral direction (Figure 39b) shows that there is a higher tensile stress around the crack tip region. In addition, the maximum tensile region on the surface is shifted from next to the contact circumference to a distance away from it. The shifted tensile stress is the cause of the second cone-crack initiation. The third and the forth cone-cracks follow for the same reason.

In general, Stage II wear is a process of cone-crack initiation and propagation from the surface outside the contact area. The wear process is governed by a cyclic tensile stress from contact loading on the surface.

4.3.3 Stage III Wear-Material Removal from Outside the Contact Area

During Stage III wear, a large volume of material removal was observed outside the contact area (Figure 28c). To investigate the causes of this stage of wear, the wear specimens were sectioned across their contact areas. From the pictures of the cross section in Figure 40 a and b, the cone-crack starts to curve up to the surface (Figure 40b) after the crack propagates down into the bulk of the specimen (Figure 40a). The curved-up crack eventually results in material being removed from the region bounded by the

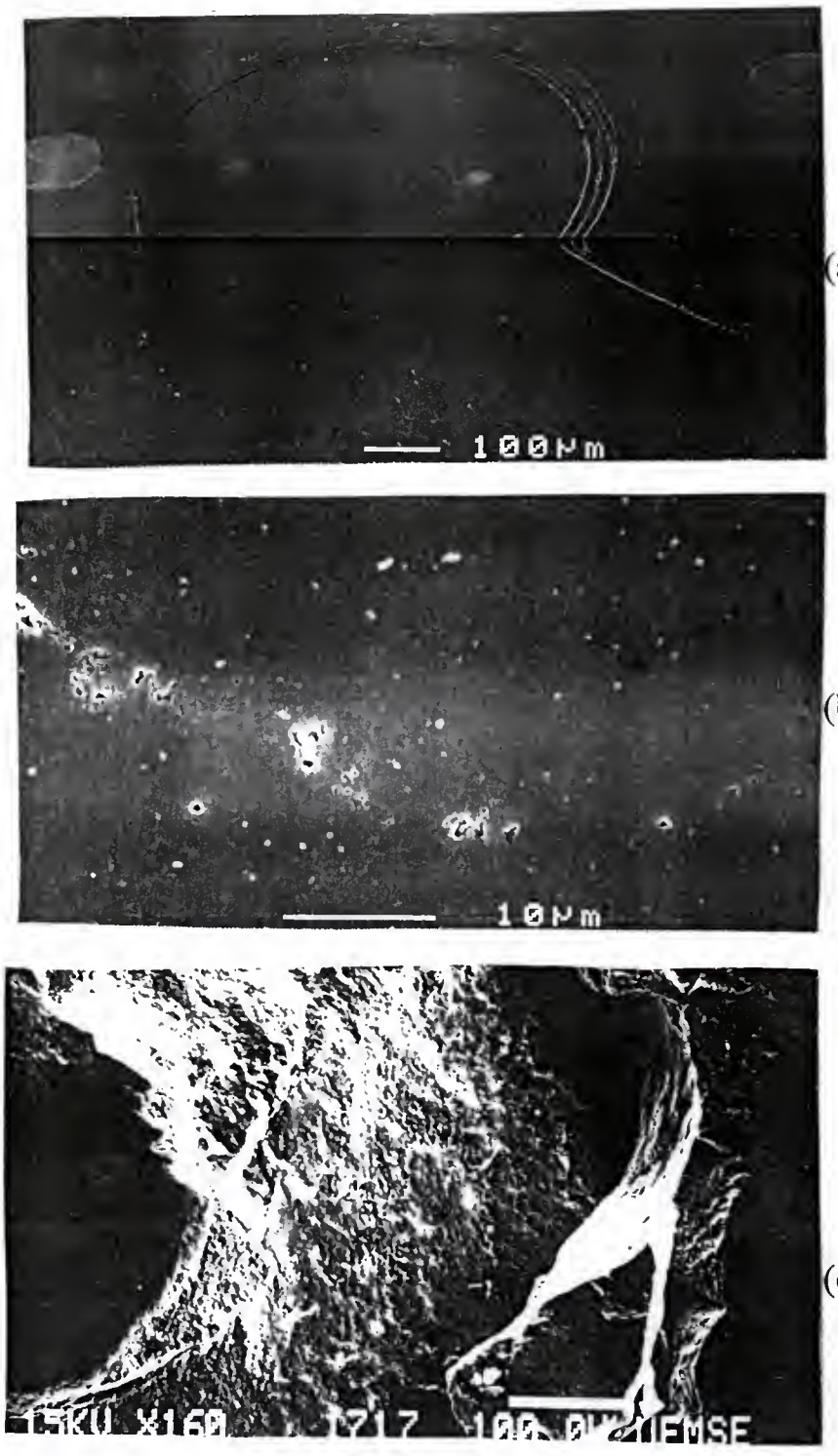

Figure 40 SEM photos from (a), (b), to (c) show the cone-crack curving up to the surface after growing a certain depth into the specimen, and material removal.

crack and the free surface (Figure 40c). Other photos in Figure 41 also display the crack curving up to the surface, and the material being removed from outside the contact area. Both cases indicate that material removal in Stage III wear is caused by the cone-crack curving towards the free surface under cyclic loading.

The picture in Figure 42a shows a specimen fractured at 27.8 GPa maximum contact stress under monotonic loading (at 900 kg/sec loading rate). The cone-crack propagates following a cone-shaped path all the way down to the bottom of the sample and then the propagation results in specimen fracture from the bottom to the top of the specimen. However, for cyclic loading, the crack only grows downwards a short distance and then starts curving up to the free surface (Figure 42b & 40c).

Singh and Shetty have demonstrated that a pre-existing crack in a brittle material will propagate towards a direction with a pure Mode I stress even though the crack starts with mixed mode stresses[126]. Hu, Bark, and Nairn also indicated that a microcracking path, in brittle laminated composites under complicated (mixed-mode) local stresses, follows the local Mode I stress path [127].

(a)

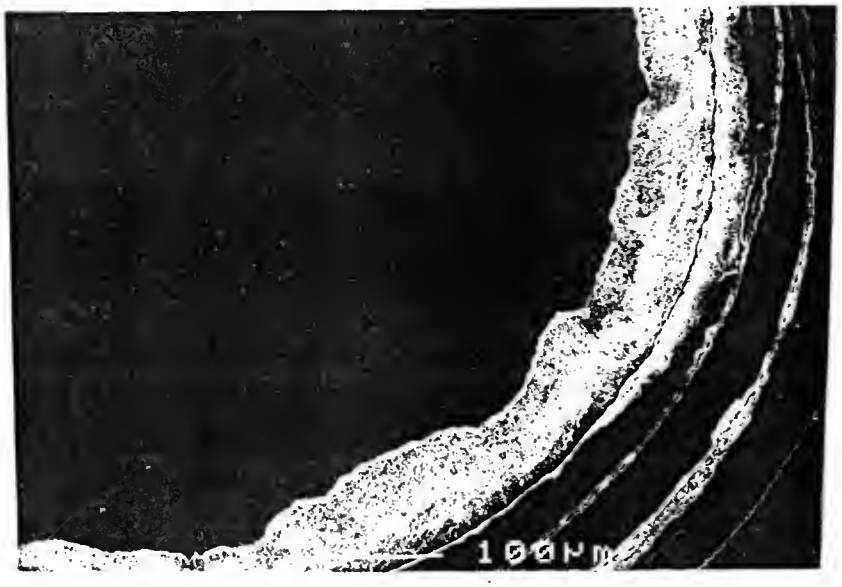

(b)

Figure 41 SEM pictures show cone-crack curving up (a) and material removal (b). Contact area is 506 µm in diameter at the center of the damaged area.

(a)

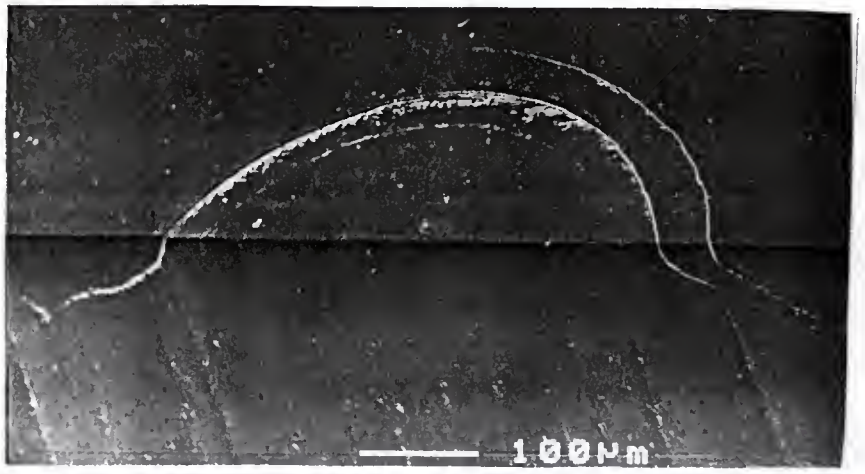

(b)

Figure 42 SEM pictures show a monotonic fracture path (a) and a cyclic fracture path (b).

It has been found that the Hertzian cone crack is not a straight crack [128]. It initiates at the top surface a little outside the circumference of the contact and propagates down into the bulk of the specimen. As the number of fatigue cycles increases, the cone crack gradually changes direction and propagates away from the contact area. In order to predict the crack path, an approximation that the crack proceeds orthogonally to the greatest tensile stress (the first principal stress or Mode I stress) is proposed here. Thus, following the trajectories of the other two principal stresses, one is in-plane (the axial symmetric plane) and the other is out-of-plane. In fact, this approximation involves two assumptions, i.e., both the crack initiation and propagation are controlled by the first principal stress. The first assumption that the crack initiation is controlled by the maximum principal stress is generally acceptable. However, the second assumption needs careful examination. It is noted that at each increment of crack growth, the first principal stress may change its direction. Consequently the path which has the maximum strain energy release rate for crack propagation may alter accordingly. Excellent agreement between the predicted crack path and the experimentally observed crack path [127], however, indicates that the stress state prior to cracking is directly related to crack propagation. Thus the

reduction of the system energy due to crack formation and propagation has a minimum effect on the principal stress trajectory. The stress state is obtained using the stress components given by [97] which are integrated over the contact area with the assumption of ideal Hertzian contact. The crack path which follows the second in-plane principal stress is obtained by this first order differential equation:

$$\frac{dz}{dx} = \frac{\tau_{xz}}{\sigma_1 - \sigma_x} = \frac{\sigma_z - \sigma_x}{2\tau_{xz}} + \sqrt{[(\frac{\sigma_z - \sigma_x}{2\tau_{xz}^2})^2 + 1]} \qquad (4.13)$$

where σ_I is the first principal stress. This equation can be solved using a fourth-order Runge-Kutta method [127]. A computer program written in FORTRAN language was used to calculate the crack path. The program is listed in Appendix B. The crack path predicted by the Mode I stress path is shown in Figure 43. Comparing the predicted path with a crack path measured from the specimen which was fractured under monotonic loading show that there is good agreement for the experimental and theoretical paths. This result clearly demonstrates that crack propagation in brittle material is governed by Mode I stress (the maximum tensile stress). However, under cyclic loading conditions, the crack path only follows the Mode I stress path to a certain distance and then starts to deviate from the predicted path

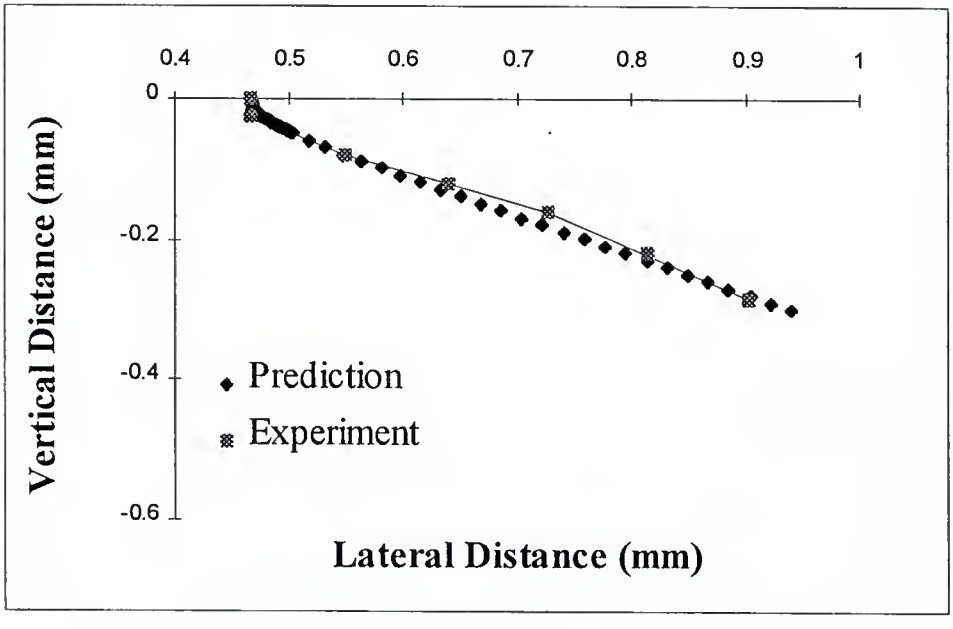

Figure 43 A measured monotonic fracture path follows the mode I stress path by prediction.

(Figure 44).

There is no precise explanation for the crack to curve up at this stage. However, there is evidence that the curve up of the crack is not due to material heterogeneity, because we found that this also occurs in homogeneous glass. From an unreported experiment which was conducted by J. Conway in the Department of Mechanical Engineering from Pennsylvania State University, a fast moving crack in PMMA (polymethyl methacrylate) brittle polymer was arrested after growing a certain distance. He found that a reflected stress wave from the back of the specimen caused a compressive stress around the crack front and suppressed crack propagation. In the ball on disc contact fatigue test, a stress wave continuously is reflected from the back of the specimens during cyclic loading. We speculate that the reflected stress wave may create a compressive stress field in front of the cone-crack to superpose the stress caused by cyclic loading and force the crack propagating up to the free surface. In fact, the crack does not have strong motivation to continuously propagate downwards after having grown a few hundred micrometers. This is because the tensile stress field or Mode I stress field decreases quickly with an increase in distance from the surface. After the crack is forced to curve up by the reflected stress wave, the crack

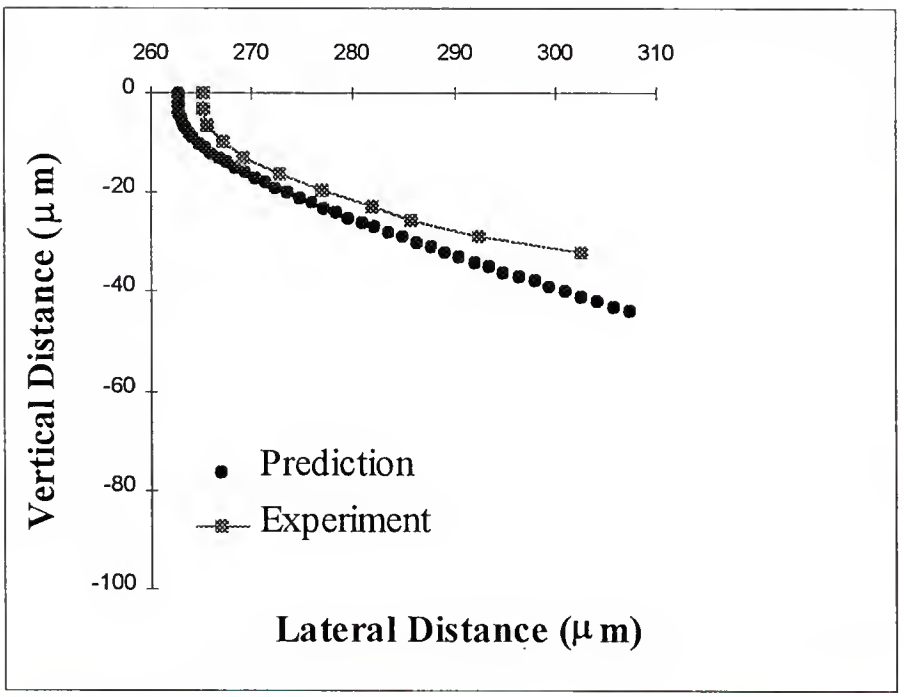

Figure 44 A cyclic fatigue fracture path follows the prediction path (mode I stress path) to a certain distance then deviates toward the surface direction towards the free surface.

then grows following the Mode I stress path up to the free surface under cyclic loading. Finally, an amount of material bounded by the crack and the free surface is removed. The mechanism which causes Stage III wear is also schematically shown in Figure 45.

For more understanding of the mechanism of the crack curving up under a cyclic load, further experiments and analysis are needed. The shape and intensity of the reflected stress wave can be adjusted by changing the loading wave form and specimen thickness. The changes in the reflected stress wave could lead a change in the shape of the crack curve if it is true that the reflected stress wave is the cause of the curve up of crack. The ideal material for these experiments is glass.

Three wear patterns and their mechanisms under contact fatigue loading have been demonstrated. However, there are still some primary concerns in hybrid ball bearing applications which will be addressed in the following sections.

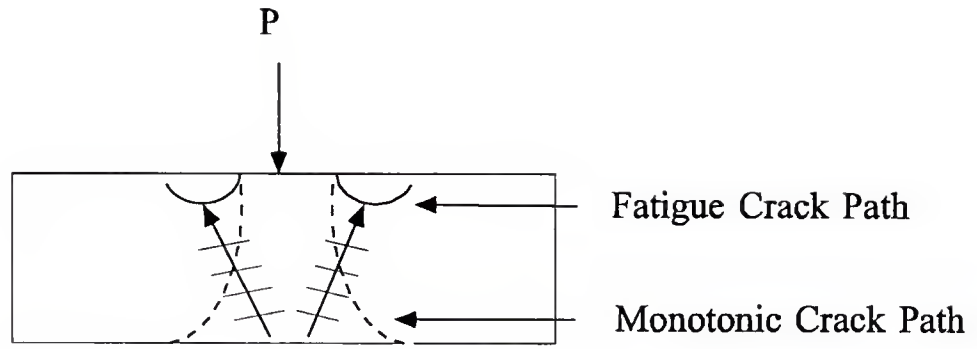

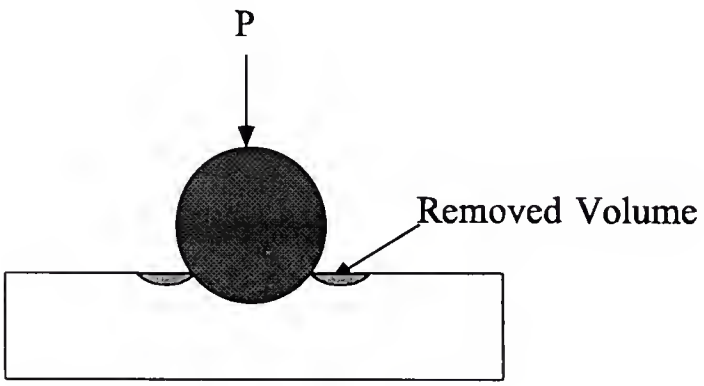

Figure 45 Schematic shows the mechanism of wear in Stage III, which is that curing a crack due to reflected stress wave results in material removal.

4.3.4 The Effect of Surface Finish on Si_3N_4 Wear Behavior

A picture in Figure 46 displays one of our polished Si_3N_4 surfaces. Even though the surface roughness is about 5 nm, under 3-D high resolution imaging (AFM), you can still see some tortuousity on the surface. The face of each grain is not at the same altitude on the specimen surface. This is because Si_3N_4 has a hexagonal crystalline structure. Its heterogeneous mechanical properties in the crystalline directions have different responses to the polishing wear. In addition, a triple-point of the grains in Figure 47 shows that the glassy phase is more easy polished than the Si_3N_4 grains due its low hardness. However, these defect sizes on the specimen surface are extremely small comparing with these on commercial products. Surface defects on commercial products can be induced in many ways, such as manufacturing, machining, handling, and transportation, etc.

The 3-D surface of an as received Si_3N_4 new ball was imaged using the AFM, which is shown in Figure 48. Some asperities and scratches on the surface after the surface was lapped were observed from the image. The surface roughness of the new ball is about 11.4 nm. After a 183 hour bearing test, the ball surface (Figure 49) shows a few asperities and some enhanced scratches. The surface roughness decreases to 6.5 nm. A decrease

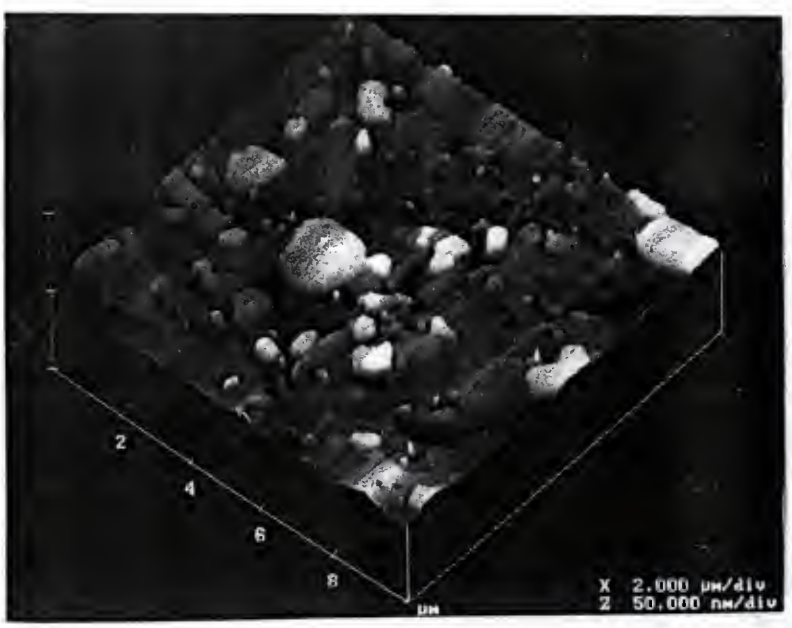

Figure 46 AFM 3-d image displays some tortuousity on the polished specimen, even though surface roughness is less than 6 nm.

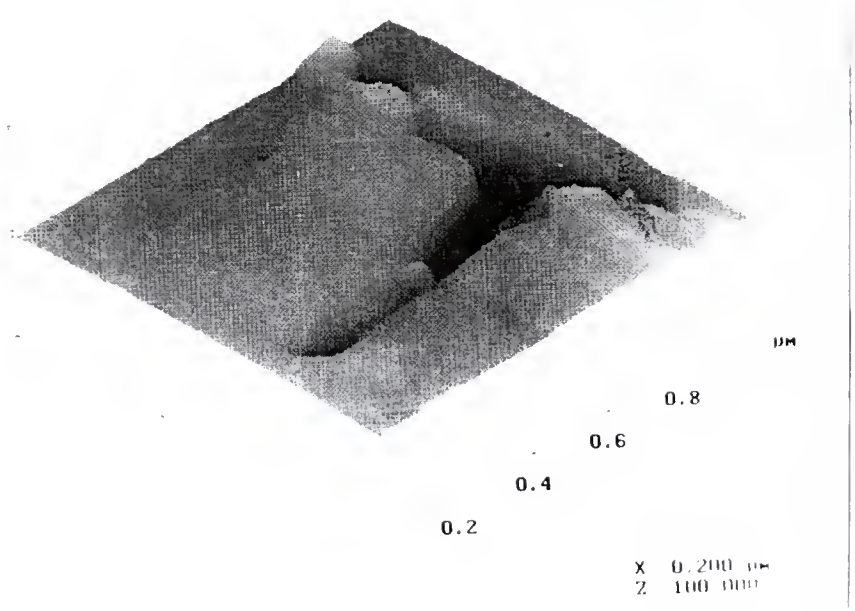

Figure 47 A depth is shown at a triple-point of the Si_4N_4 grains due to glass phase easily removed during surface polishing.

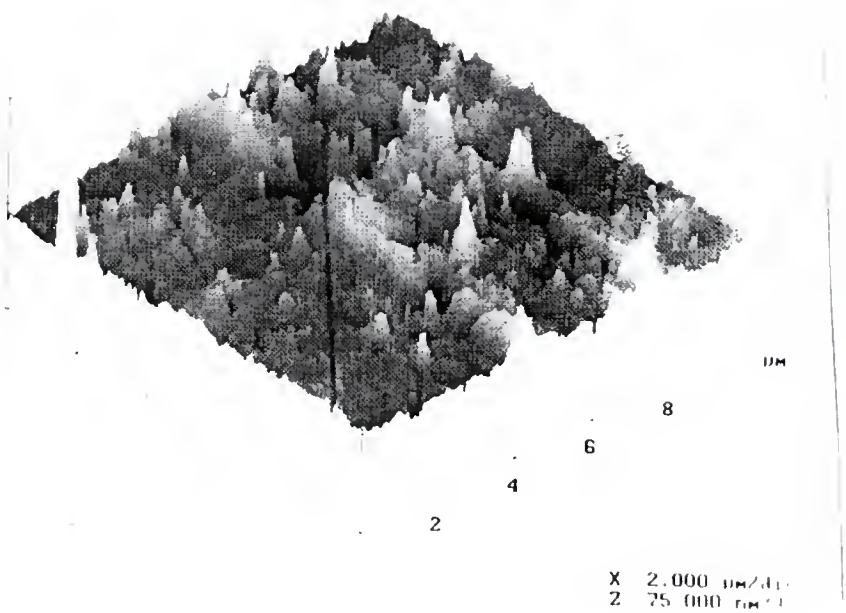

Figure 48 The surface of an as-received new Si_3N_4 ball shows some asperities and scratches due to the surface lapping process. The surface roughness is about 11.4 nm

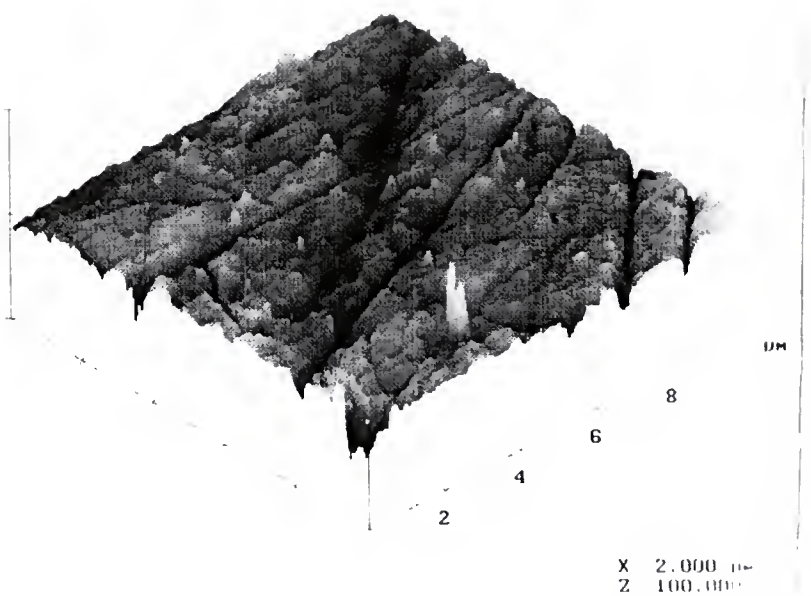

Figure 49 The surface of a Si_3N_4 ball after experiencing 180 hours bearing test shows a few asperities and some enhanced scratches. The urface roughness decreases to 6.5 nm.

in the surface roughness indicates that most of the asperities go into the lubricant or are embedded in the M50 steel during the test. These asperities may cause wear in the M50 steel race when they go into the lubricant. However, the asperities in the lubricant cause little wear of the silicon nitride ball. Surface roughness has little effect on Si_3N_4 wear.

Another concern on the ball surface is the lateral defects such as a scratch or crack. In order to study the influence of lateral defects on wear behavior, indentation techniques were used to artificially create lateral defects. First, a Knoop indentation was employed to create 5 μm wide and 40 μm long Knoop impressions to simulate scratches. The indentations were placed at different locations within an area where a contact load would be applied. A two hundred gram Knoop indent load was chosen to avoid creation of a large local inelastic zone and initiation of cracks at the corners of the impressions. SEM examination was used to verify that no cracks were found around the indentation. A cyclic contact load then was applied to the area. The results indicate that, in the contact area, scratch defects (Knoop impressions) have little effect on wear. No crack initiation and no extra wear damage were found near the indentations after 80000 cycles under 15 GPa contact stress (Figure 50). However, the scratch (Knoop indentation) in

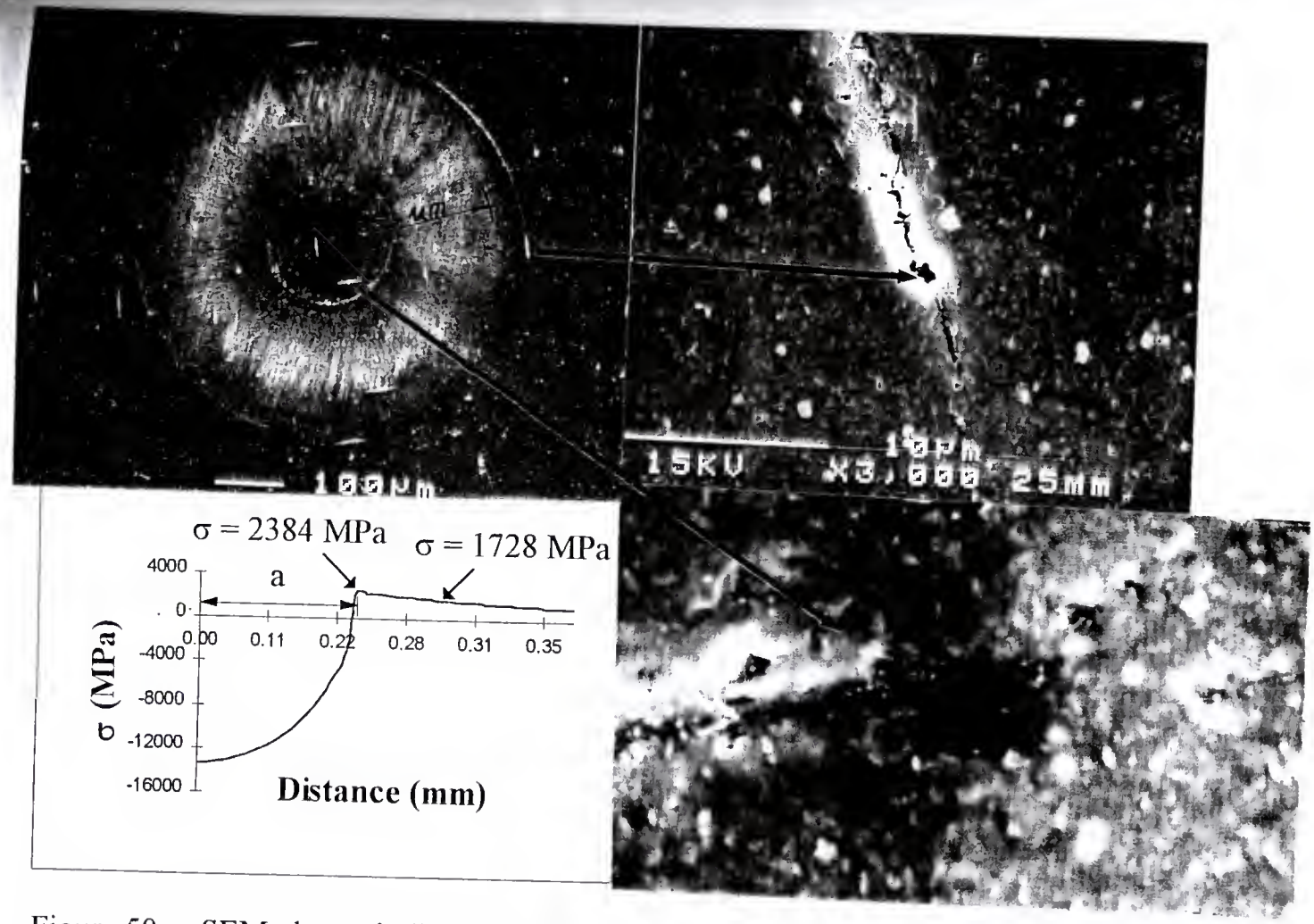

Figure 50 SEM photos indicate that the defects in the contact area caused little wear in Si_3N_4. The defect outside contact area resulted in a cone-crack initiation at low stress level. The stress curve displays the stress at the crack almost 600 MPa lower than the maximum stress.

the outside contact area promoted a cone-crack initiation. The cone crack initiated from one of the indentation sites (Figure 50) rather than from the maximum tensile stress region, even though the stress at the location of the indentation was almost 600 MPa lower. Thus, defects such as scratches can promote crack initiation and increase wear in silicon nitride at a lower stress level.

A Vickers indentation technique was also employed to induce cracks in the surface. The indentations from 1 kg or 3 kg loads were created both inside and outside the contact area. The spallation occurred from one of the indentations after 300,000 cycles under 15 GPa stress (Figure 51). The spalling pattern is very similar to those observed from the failed silicon nitride balls of the hybrid bearing system. The spallation was initiated from the region between two radial cracks of the indentation (Figure 52a) where a shallow lateral crack has potential to grow due to the inelastic zone of the indentation. The pictures in Figure 52a and b display a process of the lateral crack growing to the surface under contact fatigue loading. This experiment indicates that spallation only occurs when there are pre-existing cracks in the surface. These cracks, most likely, are lateral cracks due to large local inelastic deformation caused by sharp indenters. The lateral crack develop

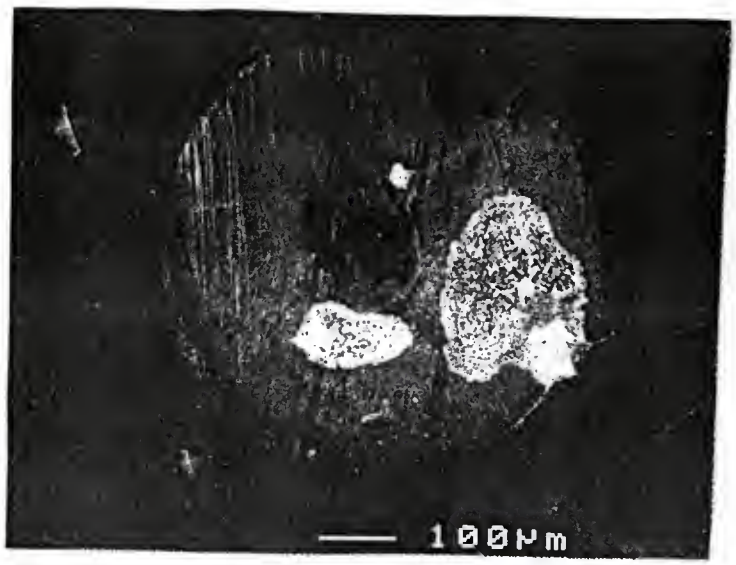

(a)

(b)

Figure 51 (a) SEM picture shows spallation happening in the contact area from the indentations. (b) A high magnification photo displays the spalling pattern, which is similar to those observed in failure bearing balls.

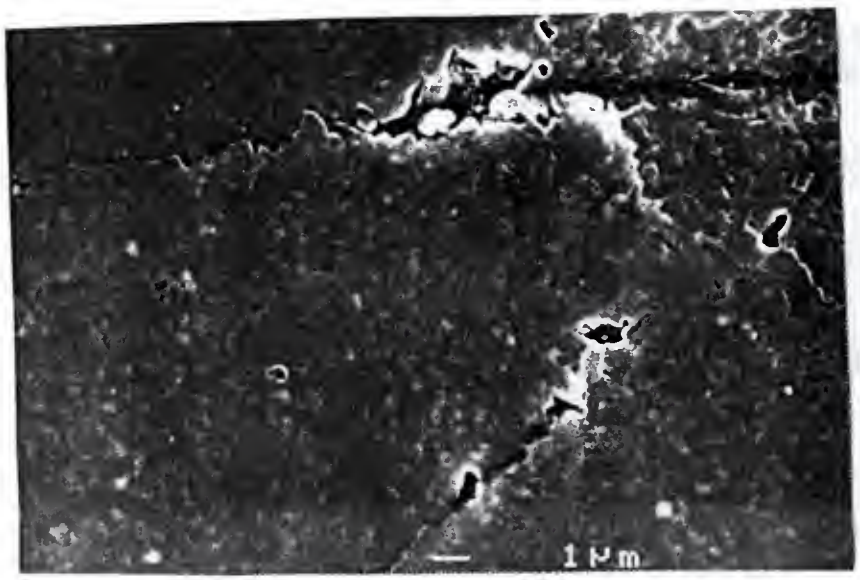

(a)

(b)

Figure 52 (a) SEM picture shows that spalling initiates at the area near indentation. (b) A low magnification photo displays spallation development.

quickly to result in spallation under contact fatigue stress. One important thing needs to be clarified: the difference between spallation and Hertzian cone cracking. Spallation is initiated from lateral defects which are mostly associated with local inelastic deformations caused by sharp indenters. Nevertheless, Hertzian cone cracking is due to Mode I stress created by contact loading within an elastic strain region. The different appearances are clearly shown in Figure 27 and Figure 51.

Lateral defects in the surface can significantly reduce the lifetime of silicon nitride under contact fatigue loading. Greater attention to limit scratches and crack defects than to decrease surface roughness in surface finishing processes may results in greater improvement in Si_3N_4 bearing ball wear resistance.

4.3.5 Subsurface Damage

Another primary concern in bearing applications is subsurface damage. Some reference articles describe subsurface damage as a brittle material wear mechanism and they attribute the subsurface damage to the shear fault underneath the contact surface[100-102]. It is inexplicable for the shear stress to initiate a crack or advance a crack in brittle materials

under hydrostatic compression, unless large defects exist in the materials. The wear samples were carefully sectioned across the contact areas and the cross sections then were polished down to a 1 μm finish. These specimens had experienced 1 million loading cycles under 15 GPa contact stress and 50000 loading cycles under 17 GPa stress, respectively. No subsurface damage underneath the contact surface has been observed (Figure 53). Several earlier studies used bonded specimens (Figure 54a) and subsurface damage underneath the contact surface at the interface after the sample was disassembled. In order to verify their results, we performed the same contact fatigue tests on the bonded specimens. 15 GPa and 13 GPa contact loads were applied to the samples, respectively. Subsurface damage was observed at the interface(Figure 54b). The subsurface damage occurs only when an artificial interface is in the contact area. The artificial interface was created by bonding two polished surfaces together using an adhesive (Krazy Glue, R, distributed by Borden Inc.). A decrease in the constraint force underneath the contact surface was caused by the artificial interface. The decreased constraint force in the direction perpendicular to the artificial interface results in an increase of the Poisson's ratio effect in this direction. The effect of Poisson's ratio near the interface results in material damage by

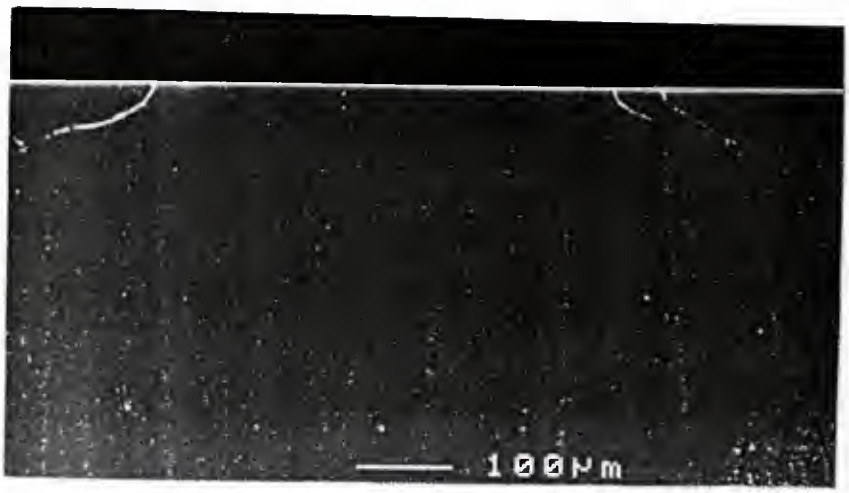

(a)

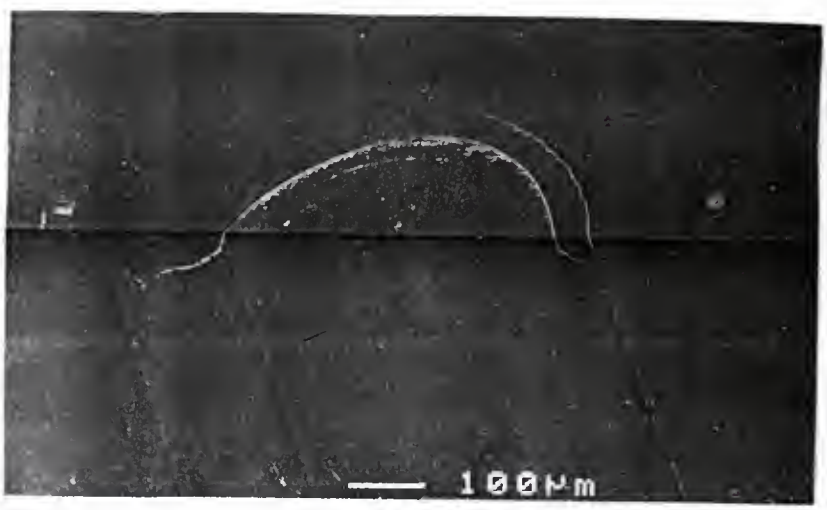

(b)

Figure 53 SEM pictures show cross-sections of the contact areas, which were tested after (a) 1 million cycles under 15 GPa contact stress and (b) 50000 cycles under 17 GPa stress. No subsurface damages are observed from both cases.

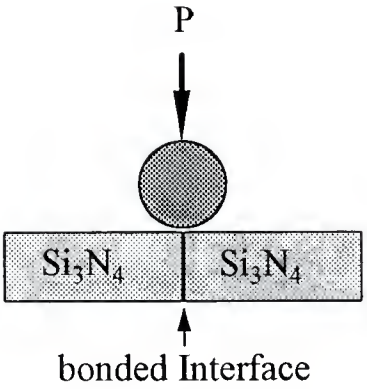

(a)

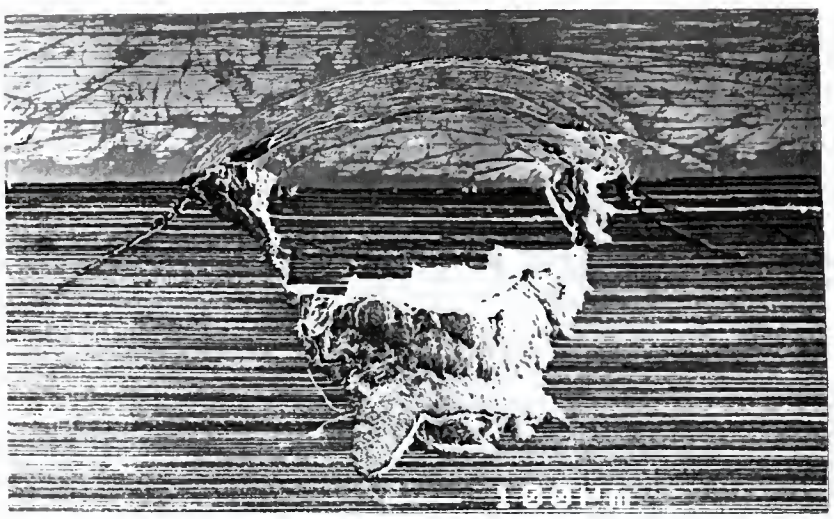

(b)

Figure 54 (a) Schematic showing a bonded Si_3N_4 specimen. (b) After disassembling the bonded specimen, which experienced 1000 loading cycles under 10 GPa contact stress, the cross-section displays subsurface damage.

shear stress near the interface and under the contact surface. From this study, it is clearly demonstrated that improper selection and preparation of specimens will lead to different results. No wear is caused by subsurface damage underneath the contact surface due to Hertzian contact fatigue stress.

4.3.6 Effect of Microstructure on Wear Behavior

The primary Si_3N_4 wear in hybrid bearing systems which has been demonstrated is a brittle fracture process under a cyclic Mode I stress. The discussion now turn to how the wear resistance of different microstructures responds to the ball on disc contact fatigue test. Two types of silicon nitride materials, Type A and Type B were chosen. The two pictures in Figure 13 display their different microstructures.

Two types of specimens were tested under 15 GPa cyclic contact stress. SEM photos in Figure 55 show the wear pattern of the Type A specimen which experienced 1 million loading cycles. Some grains were pulled-out in the contact area and a cone-crack was formed just outside the contact area. From another wear pattern of a Type A specimen after 3 million loading cycles (Figure 55b), more pulled-out grains and multiple cone-cracks were observed. Type B wear patterns are displayed in Figure

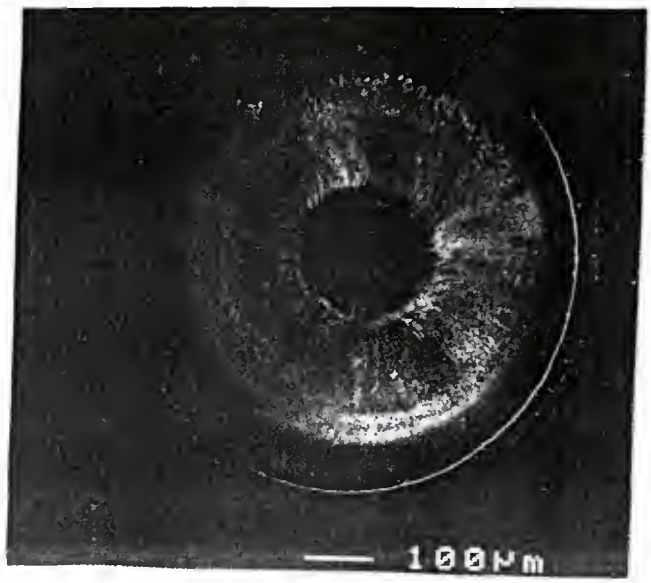

(a)

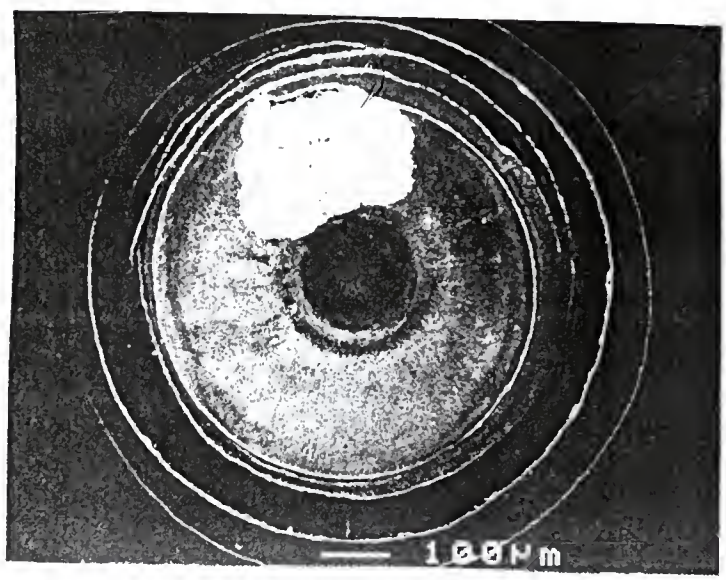

(b)

Figure 55 SEM photos show the wear patterns of type A Si_3N_4 under 15 GPa contact stress after 1 million cycles (a) and 3 million cycles (b), respectively.

56. The wear pattern caused by 1 million loading cycles (Figure 56a) shows a large number of grains pulled-out from the contact surface. After 3 million cycles in the contact fatigue specimen, a large volume of material removal is shown in Figure 56b. The results demonstrate that Type A material has a higher wear resistance than Type B. Type B shows a weaker grain boundary phase which results in more grains to be lifted from the contact surface and lower fatigue resistance which leads to larger material removal. The irregularly shaped grain structure and wide range of grain sizes may contribute to the higher wear damage in Type B material because of a lack of mechanical interlock among the grains. Type A has uniform rod-like grains and these grains are interwoven each other. It is reasonable to assume that this type of grain structure provides Type A's high resistance against grain pull-out and crack propagation. Other implications which could be drawn from the study is that the magnesium oxide based sintering phase may have a more severe delayed deformation behavior (longer relaxation time, τ) than yttrium and aluminum oxide based sintering phases. The longer τ in the glassy phase can lead to higher tensile stress along the grain boundaries and then result in faster grain boundary damage than the shorter τ in glassy phase.

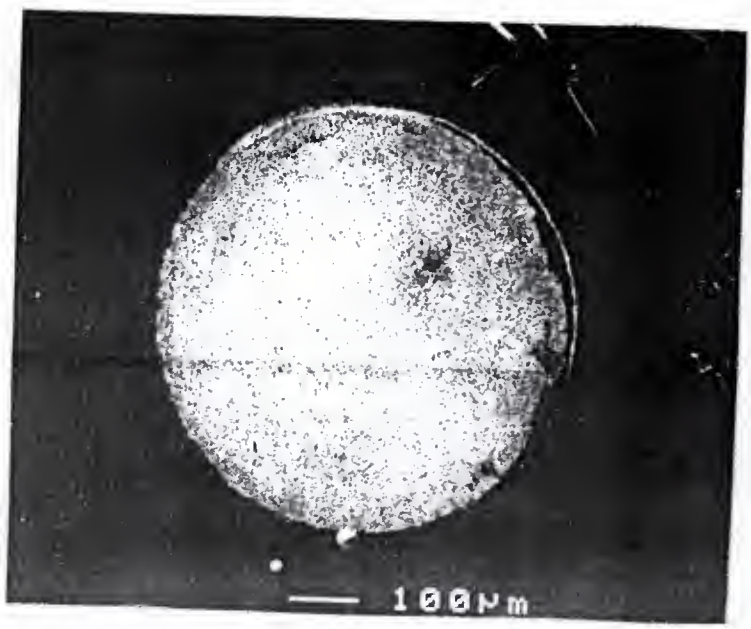

(a)

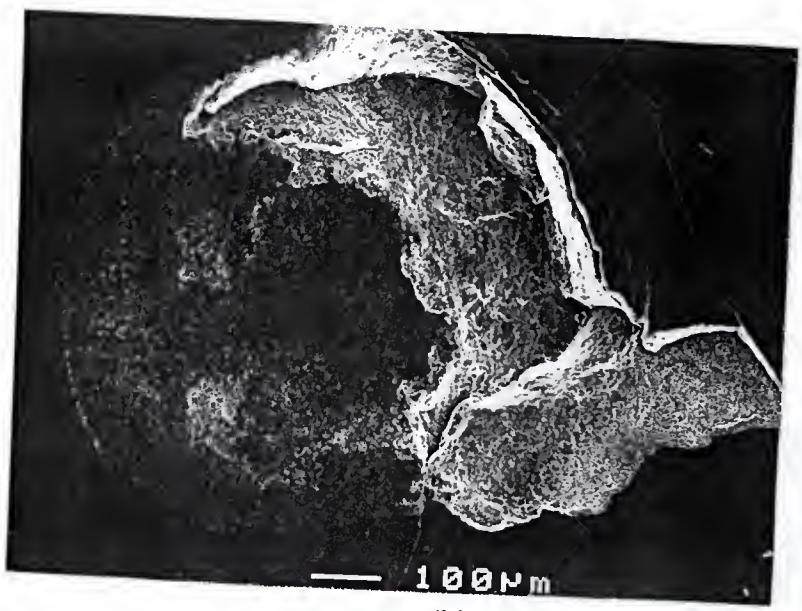

(b)

Figure 56 SEM photos show the wear patterns of type B Si_3N_4 under 15 GPa contact stress after 1 million cycles (a) and 3 million cycles (b), respectively.

This study also demonstrated that the ball on disc contact fatigue testing method can be used to study the differences in wear resistance of materials with different microstructures.

4.4 Diametral Compression Fatigue Tests under Different Environments

The diametral compression test has been used as a standardized test method for the tensile strength of concrete (ASTM/C 496). However, there are few reports in which the testing method has been used to study fatigue crack growth in silicon nitride under different environments.

Diametral compression fatigue tests were conducted under both static loading and cyclic loading. One of the side surfaces of a silicon nitride disk was indented with a 10 kg knoop indentation at the center (Figure 57a) with the long diagonal of the indent in line with the load. The maximum tensile stress in the static and cyclic fatigue tests was 120 MPa. The stress distribution along the diametric direction parallel to the loading direction is shown in Figure 55b. The maximum amplitude stress for cyclic fatigue was 120 MPa. The static test lasted 12 hours and the cyclic fatigue test lasted 10000 cycles at 10 Hz. The results are shown in Figure 58. The crack growth rates under cyclic fatigue loading are much higher than those under

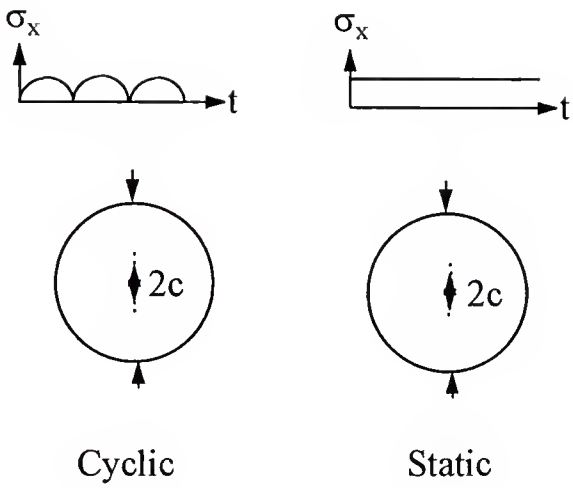

(a)

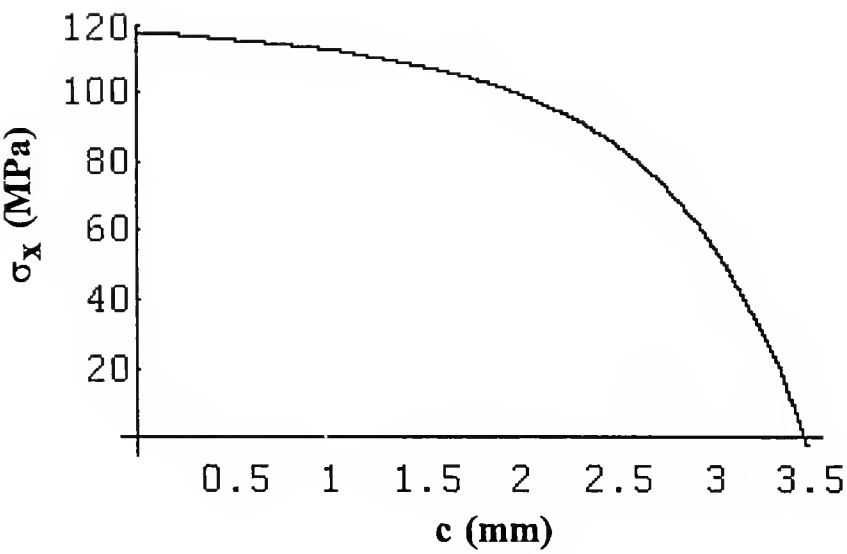

(b)

Figure 57 (a) Schematic showing the cyclic and static diametral compression tests. (b) The plot displays a tensile stress distribution along diametric direction parallel to the loading direction.

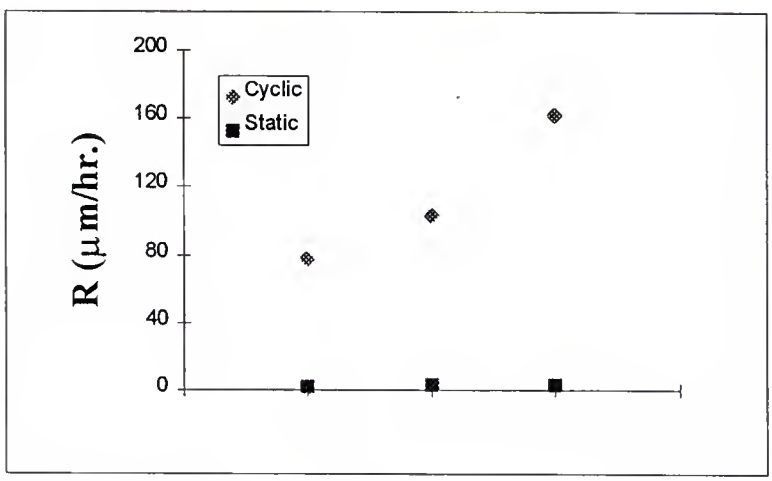

Figure 58 The plots indicate a higher crack growth rate caused by cyclic fatigue stress than static fatigue stress.

the static loading. Even though stress corrosion (which is also called static fatigue) contributes to crack growth (wear development), the major wear development in the silicon nitride bearing material is caused by cyclic fatigue.

The mechanism of cyclic fatigue crack growth in silicon nitride is the "wedge effect". Several rod-like grains were pulled out during the crack opening(Figure 59). Even though the bridging grains play a role in toughening of the material, the pulled-out grains are very difficult to return to their original position during the unloading. This juxtaposition is due to the grain position being changed during grain bridging and pull-out in the crack opening displacement. In addition, particles are created on the crack faces when the crack propagates. During unloading, the particles act as wedges between the crack surfaces resulting in tensile stress around the crack tip. The resulting stress drives the crack growth. The crack growth under cyclic loading in Si_3N_4 occurs during the unloading cycle. Crack growth is limited during static loading due to the absence of the unloading cycle.

The AFM micrograph in Figure 60 shows the fatigue crack tip which is stopped at the triple point. This phenomenon has been observed many

Figure 59 Displaced grains during the crack opening apply a force to against crack closing during the unloading cycles. The force results in crack growth during the unloading.

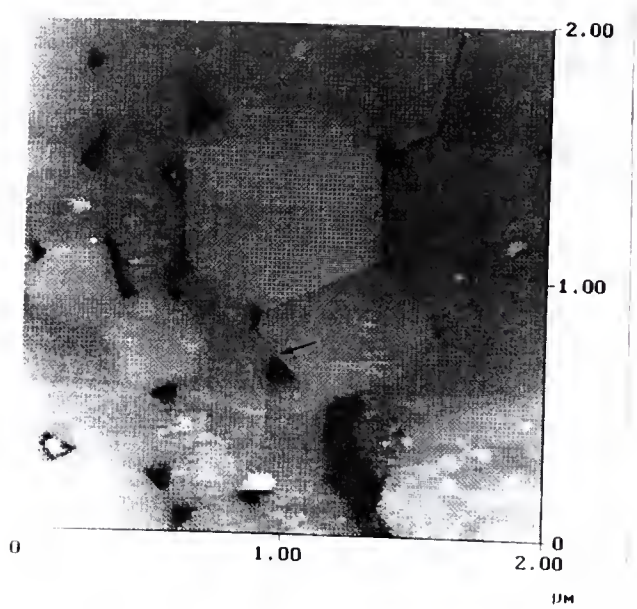

Figure 60 High resolution AFM image showing a fatigue growing crack stopped at a triple-point.

times and indicates that the fatigue crack grows around one or several grains during each unloading cycle. The crack growing distance under each unloading cycle depends on how much stress is created by the wedge effect from the particles. The larger the particles, the higher the stress at the crack tip during unloading and the larger the crack growing distance. The AFM image in Figure 61 suggests that the crack grows with a smaller resistance along the large grain boundaries than along the small grain boundaries. The small and rod-like grains can often deflect the crack growth direction at each triple point and hence more energy is needed to drive crack growth. The mechanism for fatigue crack growth has been observed by many investigators [57, 129].

The existence of cyclic fatigue crack growth in Si_3N_4 can also be seen on the fracture surface shown in Figure 62. The specimen was fractured after 46700 cycles under a 163 MPa maximum tensile stress. The initial crack (labeled with A), and the cyclic fatigue crack growth area (labeled with B) are shown in Figure 62. When the crack grew slowly to 1056 μm under cyclic loading, rapid monotonic fracture took place and the specimen was fractured into two pieces. A large smooth fracture surface beyond the fatigue crack region is the mirror region (labeled with C). The stress

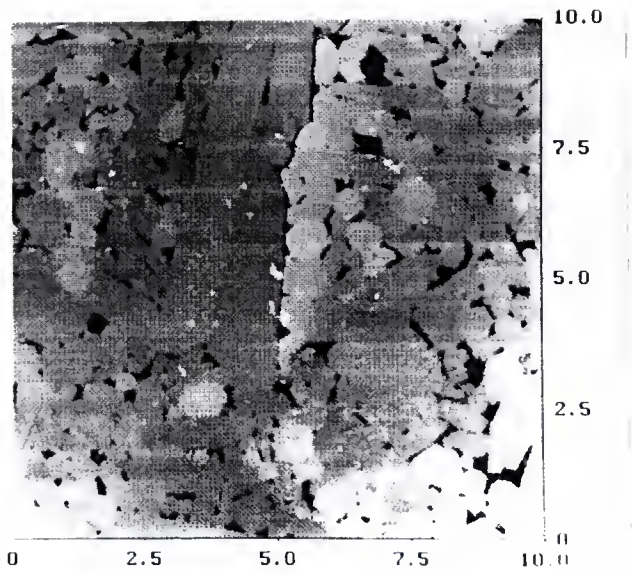

Figure 61 A high resolution AFM image shows that a fatigue crack grows along a large grain boundary with small resistance.

(a)

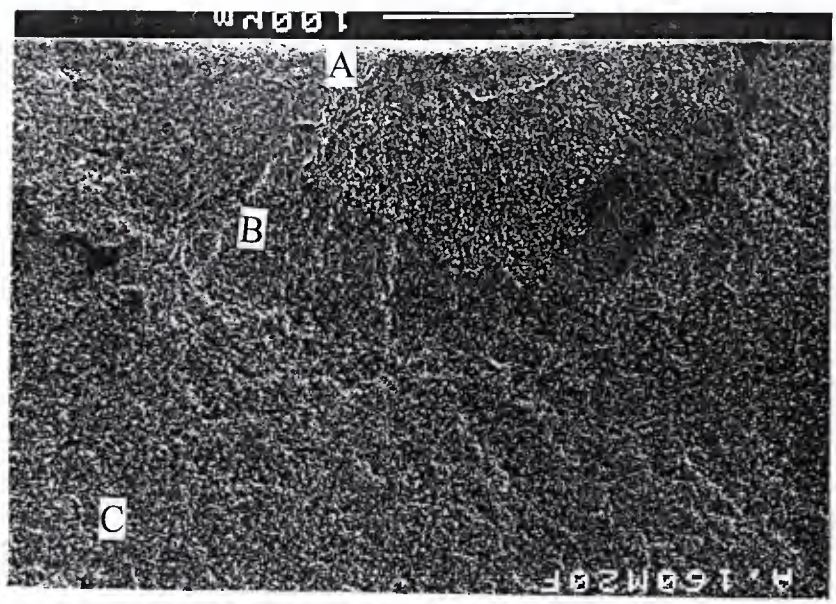

(b)

Figure 62 SEM pictures show a cyclic fatigue fracture surface in low magnification (a) and high magnification (b), respectively. The light gray area labeled with a letter B in the picture is cyclic crack growth region. Letters A and C represent the initial crack and monotonic fracture mirrror regions, respectively.

intensity factor, K_I, at the crack tip is dependent on the length of the growing crack. K_I versus crack length c is plotted in Figure 63. This plot is calculated according to Tang's equation [107]:

$$K_I = \sigma_{xx}\sqrt{\pi c}N_1(\frac{t}{R}) \tag{4.14}$$

where σ_{xx} is the distributed tensile stress (eq. 3.7), and $N_1(t/R)$ is a function of the stress intensity factor related to the specimen dimension. The general expression of the function is:

$$N_1(\frac{t}{R}) = L_0(\frac{t}{R}) + L_1(\frac{t}{R})\alpha + L_2(\frac{t}{R})\alpha^2 + L_3(\frac{t}{R})\alpha^3 \tag{4.15}$$

where α is the ratio of crack length c over specimen dimension d (diameter), and $L_0(t/R)$, $L_1(t/R)$, $L_2(t/R)$, and $L_3(t/R)$ are functions of the thickness, t, and the radius, R, of the specimen. The values for each function can be found in reference [107]. When the crack grew to c =1056 μm, K_I is 9.5 $MPam^{1/2}$ calculated according to equation (4.14). From section 4.21, the critical stress intensity factor of Type A at crack length = 1000 μm is about 9.8 $MPam^{1/2}$. Monotonic fracture occurred in the specimen when K_I at the crack tip increased to K_{Ic} for Type A after 46700 loading cycles.

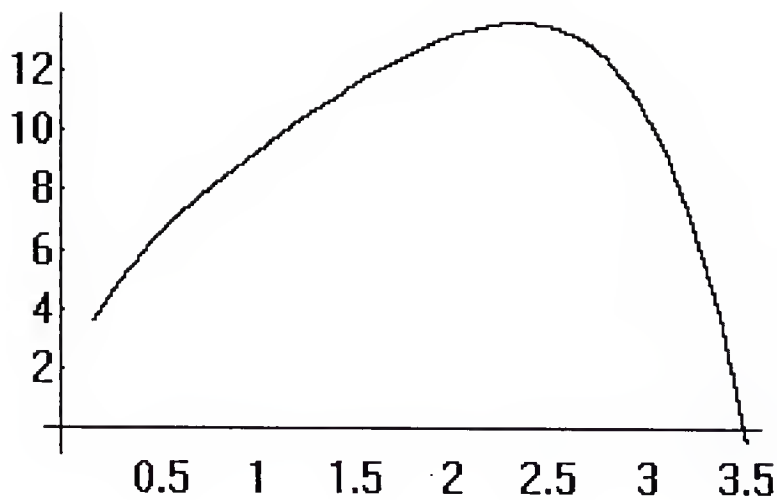

Figure 63 The stress intensity factor, K_I, is a function of the crack size, c, in a diametral compression test.

The cyclic fatigue process for silicon nitride basically consists of cyclic crack growth, which is a stable crack growth process, and monotonic fracture, which is a catastrophic fracture process.

The crack growth rate also shows a strong correlation with the stress intensity factor. The plot in Figure 64 demonstrates that after the stress intensity factor reaches $K_I = 3.75$ MPam$^{1/2}$, any increase in K_I can result in significant increase in the crack growth rate.

The diametral compression fatigue test was also employed to investigate the crack growth rate between Type A and Type B materials. The plots in Figure 65 display that Type B has higher crack growth rates than Type A. This agrees with the results found in the ball on disc contact fatigue test. The micrographs in Figure 66 show the crack paths in both Type A and Type B materials. The crack in Type A grows in a more tortuous manner than the crack does in Type B. In addition, the mean free path distance, which is a distance between the points at which the crack changes its crack growth direction, is much shorter in Type A than in Type B. From the picture in Figure 66b, we can see that larger grains existing between the crack faces may play a role in the toughening mechanism, but they also significantly increase the wedge effect during unloading. An

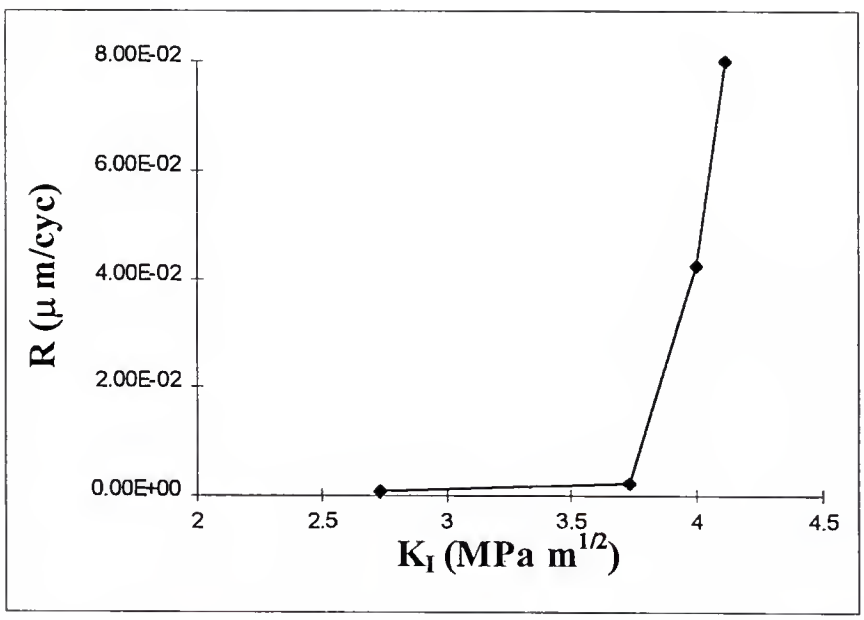

Figure 64 The crack growth rate under a cyclic fatigue load (in the air) increases quickly when $K_I > 3.5$ MPam$^{1/2}$.

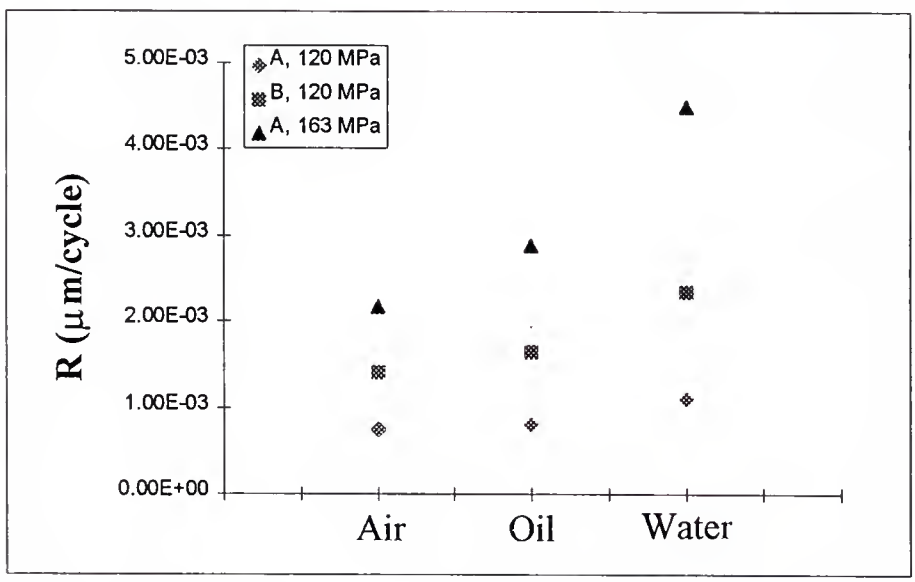

Figure 65 The plots indicate a higher crack growth in Type B than Type A. The crack growth rates are also dependence of environments and stress levels.

(a)

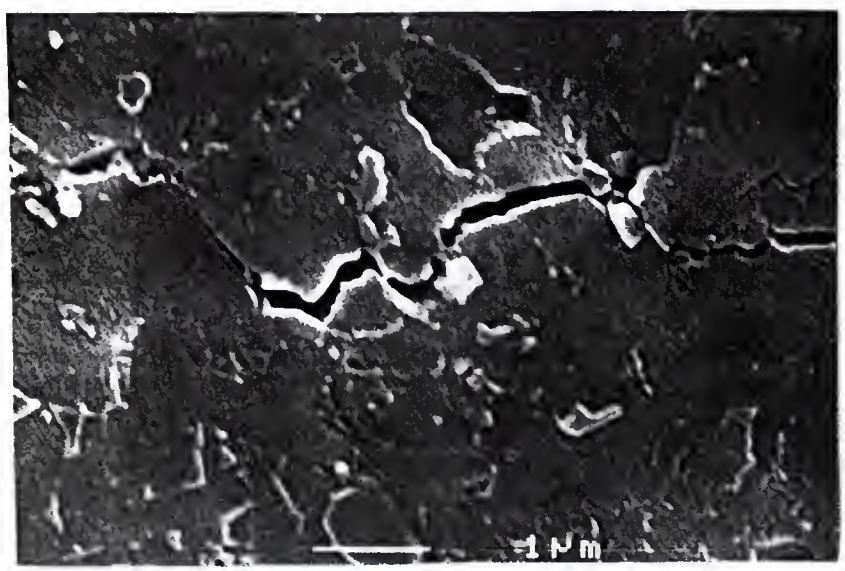

(b)

Figure 66 SEM photos exhibit the different crack pathes in Type A Si_3N_4 (a) and Type B (b), respectively.

increase in the wedge effect can increase the crack growth rate under the unloading cycles. All these factors demonstrate that Type A has a higher wear resistance than Type B.

In addition to the crack growth in Si_3N_4 under cyclic loading, the plots in Figure 65 indicate that water (H_2O) and Exxon turbo oil can enhance the crack growth rate. It has already been recognized that the oxide sintering phases exist in the grain boundaries and that the crack growth follows the grain boundaries. Wiederhorn, et al. showed that hydroxide group (OH) in water or in other dielectrics can assist crack growth even under a low stress level [130]. The mechanism for this type of crack growth was described as Si-O bonds, which are strained by a stress, are fractured by the chemical reaction between OH^- ions and Si-O bonds. The reaction rate is dependent on the concentration of OH^- ions and stress level at the crack tip. Water has the highest OH^- concentration, Exxon oil ($\approx$ 90% humidity) is next, and air ($\approx$ 70% humidity) has the least OH^- concentration of the three. The results shown in Figure 65 agree well with theory; the crack growth shows the highest rate in water, then in Exxon oil, and the lowest rate in air.

This experiment demonstrates that cyclic fatigue stress controls wear development in silicon nitride materials. The hydroxide group can enhance

wear development. The critical value of the stress intensity factor is K_I = 3.75 $MPam^{1/2}$. The wear will increase significantly under a cyclic fatigue stress when the stress intensity exceeds this critical value.

Based on the results of the present experiment, we can conclude the small rod-like grain structure is recommended to improve wear resistance of Si_3N_4 bearing material. In addition, the sintering phase should form a strong bond with the Si_3N_4 grains, and should have less reactivity with any environment such as water molecules.

4.5 The Geometry of Wear and Fracture Surfaces

To further verify our conclusion that wear in brittle materials is a crack initiation and propagation process of brittle fracture, the fractal geometry technique was applied to wear surface analysis. For wear and fracture surfaces, the surface geometry can be described using a quantitative fractal dimension rather than a word, such as rough or smooth.

The fracture process in brittle materials leaves characteristic markings on the fracture surface. Shand recognized the importance of these markings on the fracture surface of brittle materials in terms of quantitatively identifying characteristic parameters such as the stress at fracture and

velocity of the crack front [131]. An idealized fracture surface contains an origin with surrounding topography showing mirror, mist, and hackle regions.

However, not all fracture surfaces show all the idealized features. In Figure 67, four surfaces show apparently different appearances from an identical (Type A) material. The fracture surface appearances are determined not only by material properties but also by initial flaw/defect sizes and stress states. Fracture in brittle materials is an atomic bond breaking process. Therefore, the question can be asked if there exists a relationship between bond breaking and fracture surface geometry. Recent developments in fractal geometry have presented the possibility of enhancing the field of fractography to microstructure or even atomic scale level.

Many people have already shown that the nature of the fracture surface can be described using fractal geometry[132,133, 134]. Fractal geometry is a non-Euclidean geometry that allows for non-integer dimensions and has been used to describe a variety of natural processes. The fractal dimension of a line, for example, will reside between 1 and 2. A relatively "smooth" line would have a dimension of 1 (Euclidean). A

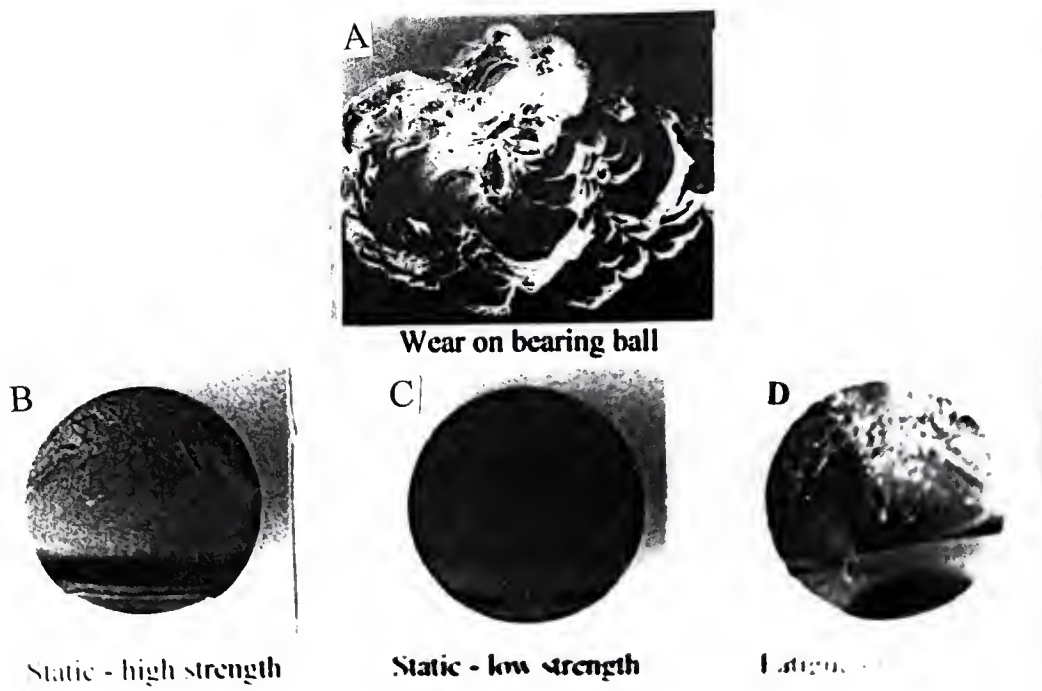

Figure 67 A, B, C, and D are from an Identical material (Type A). A was failure during the bearing test. B and C were fracture in bending at different stresses. D was fractured during rotating fatigue. Each case gave their own characteristic markings on the surface.

tortuous line could have a dimension greater than one (Figure 68). The dimension increases as the tortuosity increases. The fractal dimension of a surface lies between 2 and 3, etc. Mecholsky et al.[134-136], experimentally determined a relationship between fracture toughness (K_{Ic}) and fractal dimension (D). They found that

$$K_{Ic} = AD^{*1/2} + K_o \tag{4.16}$$

where A is a family parameter, D* the fractal dimensional increment. K_o accommodates the possibility of perfectly plane fracture, i.e. D=2. The family parameter, A, can be described by the expression:

$$A = E\sqrt{a_o} \tag{4.17}$$

where E is the elastic modulus and a_o is a characteristic atomic dimension. Although not totally understood, there is some evidence that "families" would be composed of either single crystals, large-grained materials, glass ceramics or fine-grained polycrystalline materials [137]. Within a family, an increase in fractal dimension corresponds to an increase in fracture toughness. In this study, we use fractal analysis to study the nature of fracture in silicon nitride and the geometry of the wear and fracture surfaces.

Three types of fracture surfaces and one wear surface (Figure 67) were analyzed in this study. In Figure 67, A is a wear surface which was

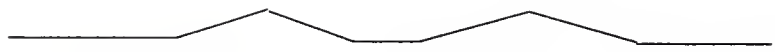

"Smooth" line, D = 1

Totuous line, 1 < D < 2

Figure 68 Schematic showing that tortuosity of line can be related to fractal dimension.

created during a bearing test, B and C were fractured in four-point flexure at different stresses, and D was fractured during a rotating cantilever beam fatigue test. The fractal dimensions of the wear and fracture surfaces were determined using the Richardson and Box counting methods [138]. The Richarson method was used in measurement of D* from replica specimens and the Box counting method was used with AFM software. These two different techniques were described in chapter 3 and are schematically shown in Figure 69.

The fracture contours obtained from polishing the replica samples are shown in Figure 70. The plot of count numbers versus ruler size is also shown in Figure 70 and whose slope was used to determine the D* of the fracture surfaces,. Sectioned AFM images and the corresponding graph are exhibited in Figure 71. The fractal dimensions obtained from the experiments are listed in Table 5.

The three fracture surfaces and one wear surface have similar fractal dimensions regardless of their different surface appearances. The different locations A, B, and C on the fracture surface (sample B) also exhibit the same fractal dimension (Figure 72). Moreover, the fractal dimensions measured using both techniques show consistency. Using the AFM, we

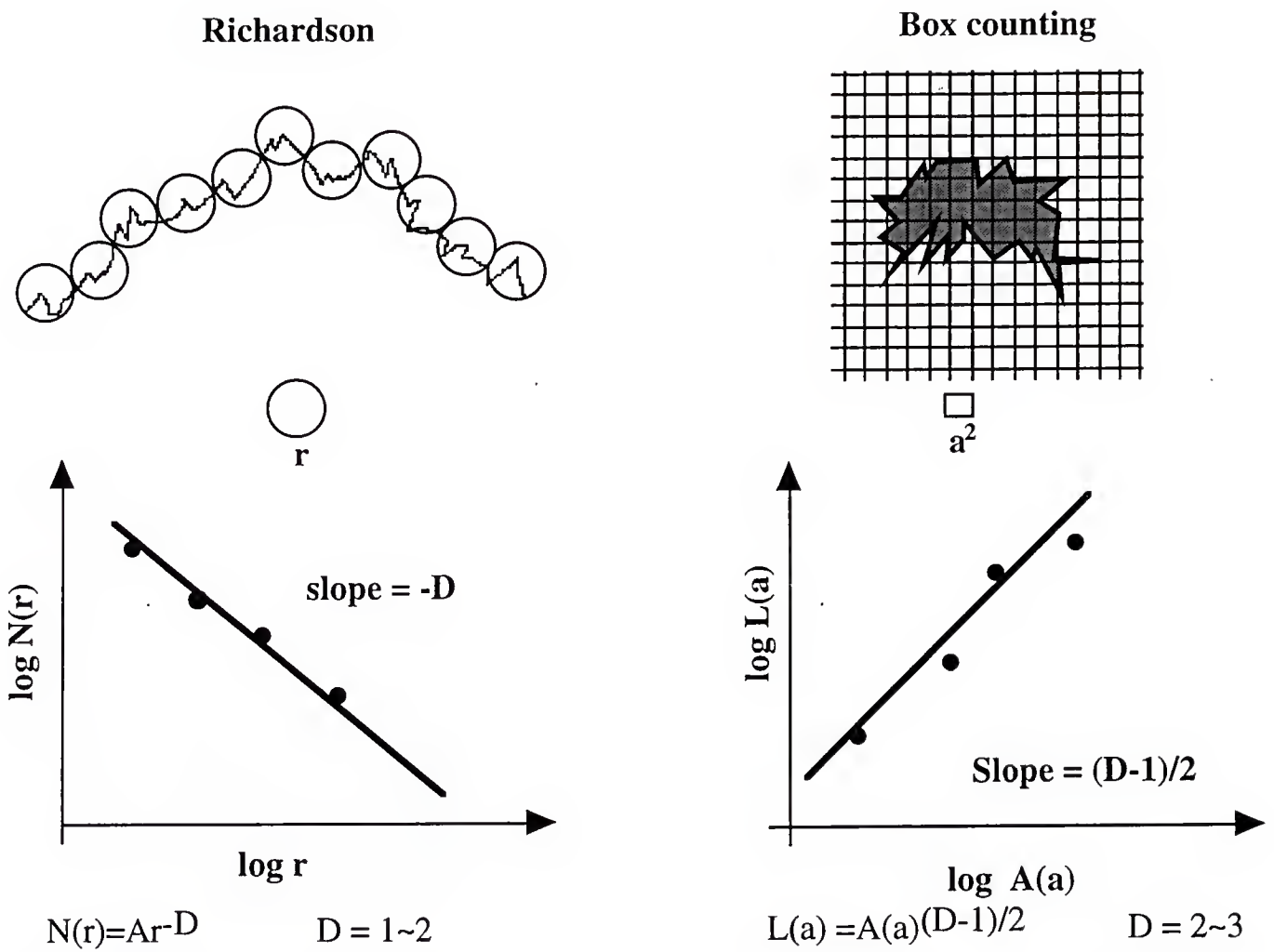

Figure 69 Schematic showing the fractal dimension measurement techniques,i.e., Richardson and Box counting.

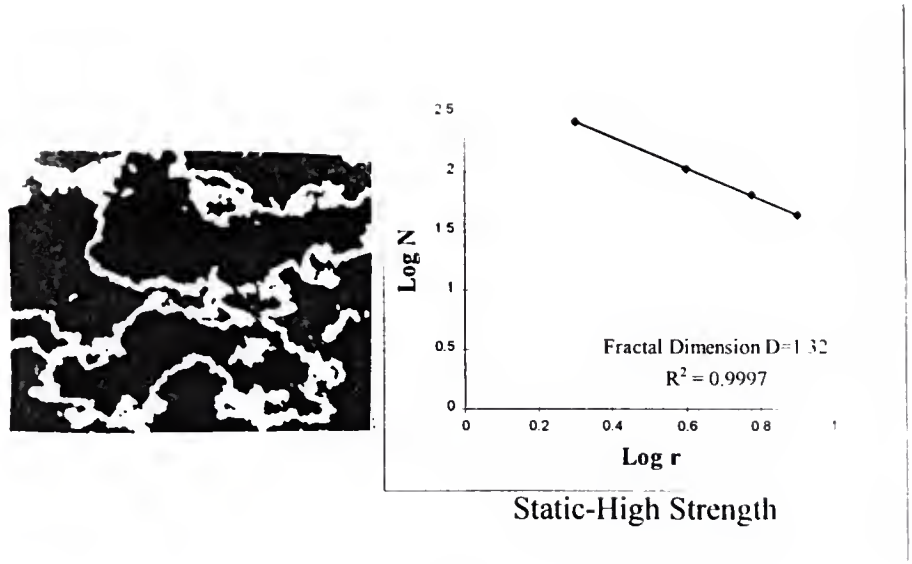

(a)

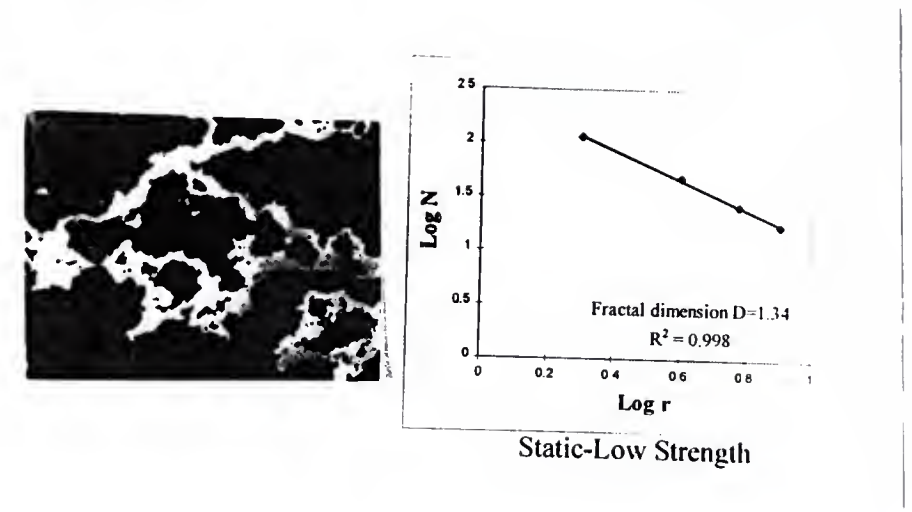

(b)

Figure 70 The Richardson method was used to measure D* from the fracture contours, (a) high stress bending fracture and (b) low stress bending fracture.

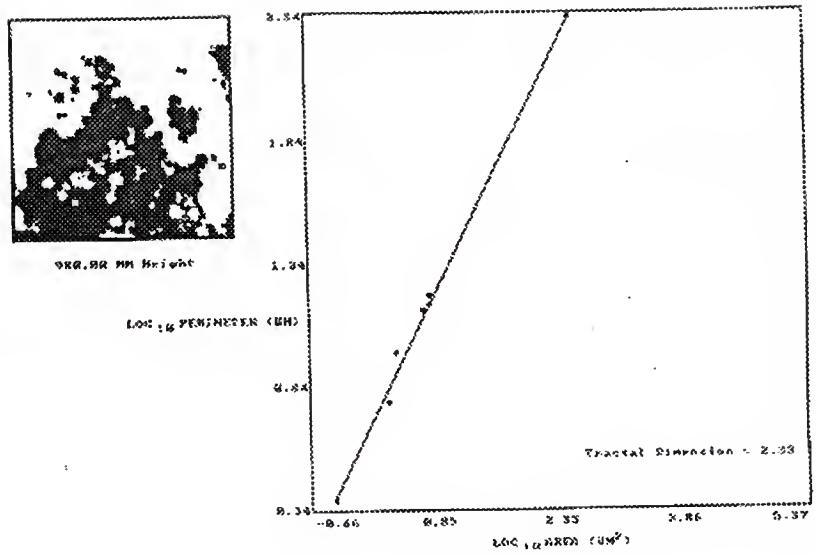

(a)

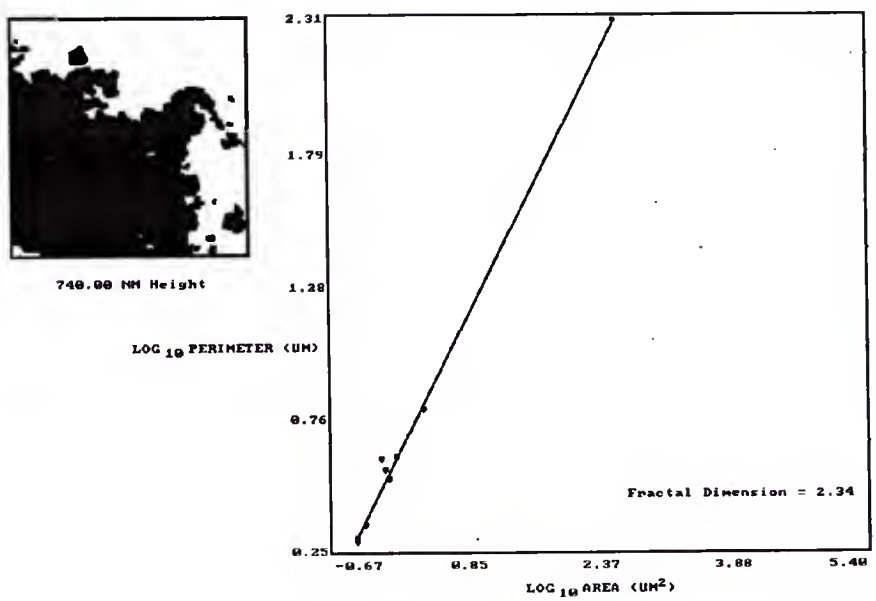

(b)

Figure 71 The box counting method was used to measure D* from the islands of (a) high stress bending fracture, (b) wear surface and (c) fatigue fracture surface.

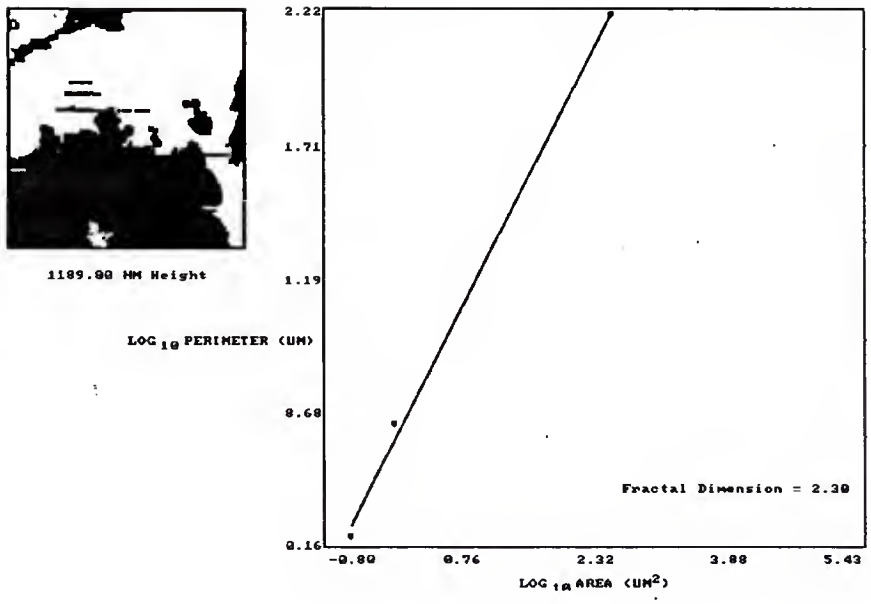

(c)

Figure 71--continued

Table 5 Fractal dimension increment data, D* data

	Surface A	Surface B	Surface C	Surface D	Location A	Location B	Location C
D_1*	non	0.32±0.03	0.33±0.03	0.33±0.04	non	non	non
D_2*	0.31±0.05	0.33±0.05	0.34±0.03	0.30±0.05	0.33±0.04	0.34±0.03	0.32±0.03
D*	0.31	0.33	0.34	0.32	0.33	0.34	0.32

* D_1* and D_2* are obtained from polishing method and AFM method. D* is average value.

** ± is standard deviation.

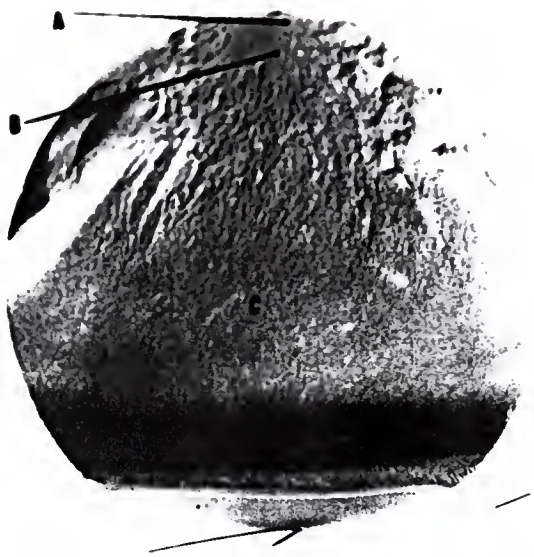

A: D*=0.33 **B: D*=0.34** **C: D*=0.32**
S.D. = ±0.03

Figure 72 Fractal dimensions were measured from the A, B, and C locations, respectively.

measured D* from areas down to 20 μm^2 and the fractal dimension value obtained are given in Table 5. The fractal dimension for each surface was averaged from more than 12 measurements. The typical D* data distribution from one surface is displayed in Figure 73. Two fracture contours from different scales show self similarity (Figure 74). From both experimental methods, the measured D* values appear the same regardless of scale. In addition, the toughness versus the fractal dimensional increment $D^{*1/2}$ is plotted with other polycrystalline material data (Table 6 [142]) in Figure 75, where the silicon nitride K_{Ic} used is the lowest value (intrinsic value, K_{Ic}= 5.8 $MPam^{1/2}$) i.e., disregarding the increment of K_{IC} due to grain bridging toughening. The K_{Ic}-$D^{*1/2}$ values lie approximately on a straight line. This indicates the relationship between K_{IC} and D* (equation 4.16), which was proposed by Mecholsky et al., also applies to silicon nitride. Thus, as the fractal dimension increases, fracture toughness increases.

This experiment discovered that, for an identical material, D* shows consistent values from different surfaces which were created under different stress states. D* for Type A material can be related to its intrinsic toughness through equation 4.16. Furthermore, the D* value is independent of scaling factors for an identical material. The information from the experiment

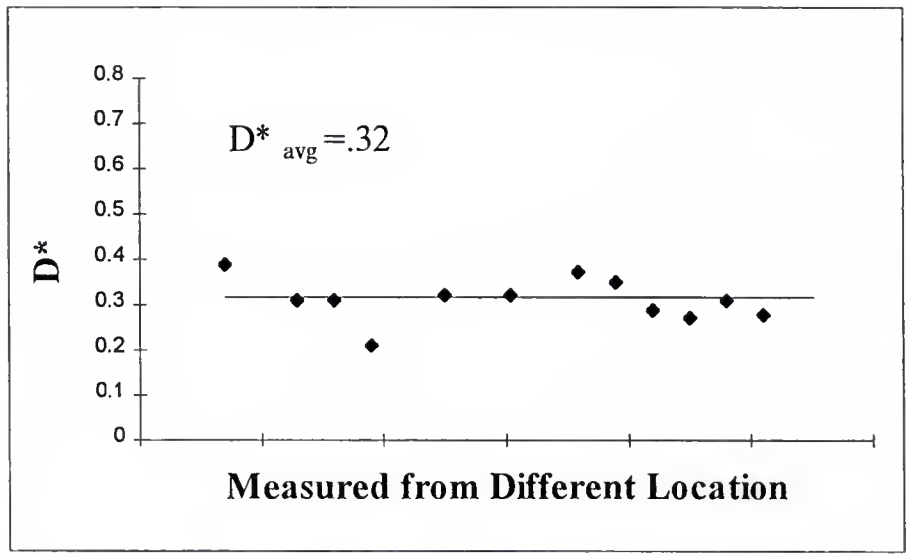

Figure 73 Typical distribution of the measured fractal dimension D* data from one fracture surface using the AFM.

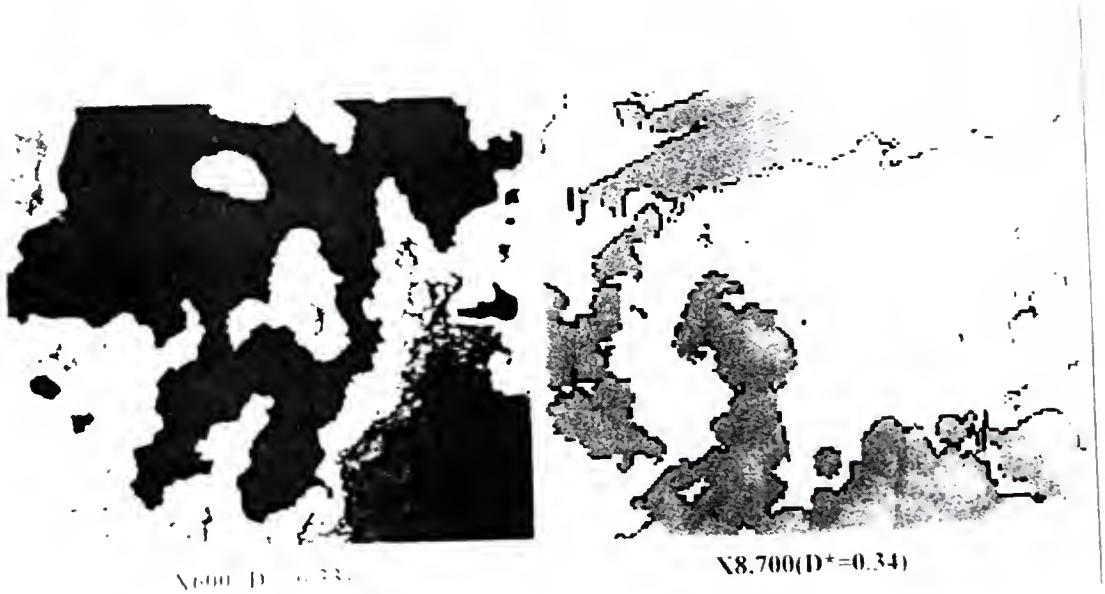

Figure 74 Slit island contours are shown in this photo. On the left, the contour was from the polishing method at x100. The right is from the AFM at 3200. Both of them show similarity regardless of the different scale.

Table 6 The data of fracture toughness and fractal dimension increment of brittle polycrystalline materials.

Number	Material	$K_{Ic}(MPam^{1/2})$	D*
1	Zinic Sillicate (ZSGC No.1)	2.0	0.05
2	Zinic Sillicate (MS 498-5)	2.2	0.07
3	Zinic Sillicate (ZSGC No.2)	2.0	0.09
4	Zinic Sillicate (MS 500-4)	2.2	0.12
5	Al_2O_3 (UCC)	4.0	0.15
6	Pyroceram (9606)	2.5	0.17
7	Al_2O_3 (WESGO A1500)	3.6	0.20
8	Al_2O_3 (AD99)	2.9	0.21
9	Al_2O_3 (GEND)	3.9	0.23
10	Al_2O_3 (AD999)	3.9	0.31
11	Al_2O_3 (Lucalox)	4.0	0.31
12	Si_3N_4 (Type B)	5.0	0.30
13	Si_3N_4 (Type A)	5.8	0.34

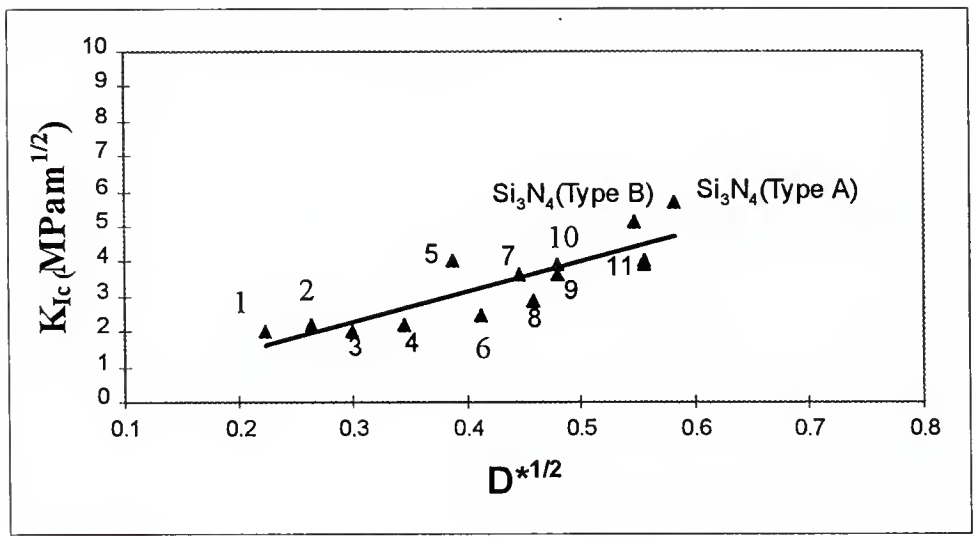

Figure 75 The toughness of polycrystalline ceramics as a function of fractal dimension D*

implies that: 1. the fractal dimension can be related to material characteristics regardless of the fracture stress states. 2. The fracture process in Si_3N_4 is a self-similar process from small scales to large scales. 3. The fracture process for brittle materials is a bond breaking process under a Mode I stress condition regardless of the global stress states. 4. The relationship between D* and the material constants further implies that fracture is a fractal process and is a material characteristic i.e., structure and bond energy.

The topography of the silicon nitride fracture and wear surfaces, therefore, were correlated through the fractal dimensional increment, D*. The same D* value for both the fracture and wear surfaces indicates that wear is a brittle fracture process which occurs in a local region. In addition, the D* value can be related to a material fracture constant K_{Ic}. This correlation is consistent with previous findings [134-136]. Thus, the reason that the fractal approach is appealing is that it not only provides a means of characterizing the material's fracture and wear surface, but also suggests a means for generation of the fracture surface. From this study, the fractal method emerges as a method with potential for identification of a failure

model, and eventually will lead to an understanding of fracture and wear processes in material structures.

4.6 XPS Surface Analysis

Two types of Type A Si_3N_4 surfaces were examined using X-ray photoelectron Spectroscopy (XPS); one is a polished surface and another is a bearing ball surface. The bearing ball had been tested for 180 hours. The purpose of this experiment is to study the major surface species present and their chemical states. The XPS spectrums of Si-2p are shown in Figure 76. For the polished surface, the peak location of Si-2p shifts from standard Si-N location at 101.8 eV to SiO_2 location at 103.7 eV (Figure 76a). The mass ratio of N over Si decreases from 0.67 (theoretical calculation) to 0.39. This result indicates that a SiO_2 thin film was created on the surface during the polishing process. For the bearing ball surface, there are three distinct peaks present (Figure 76b). Si-N bond (typical of Si_3N_4) peak occurs at 101.8 eV, Si-O bond (typical of SiO_2) peak occurs at 103.7 eV, and the another peak appears at 102.8 eV which indicates a silicon oxynitride structure. The ratio of N over Si in the ball surface is 0.15. These results indicate that some tribochemical reactions participated in the wear process,

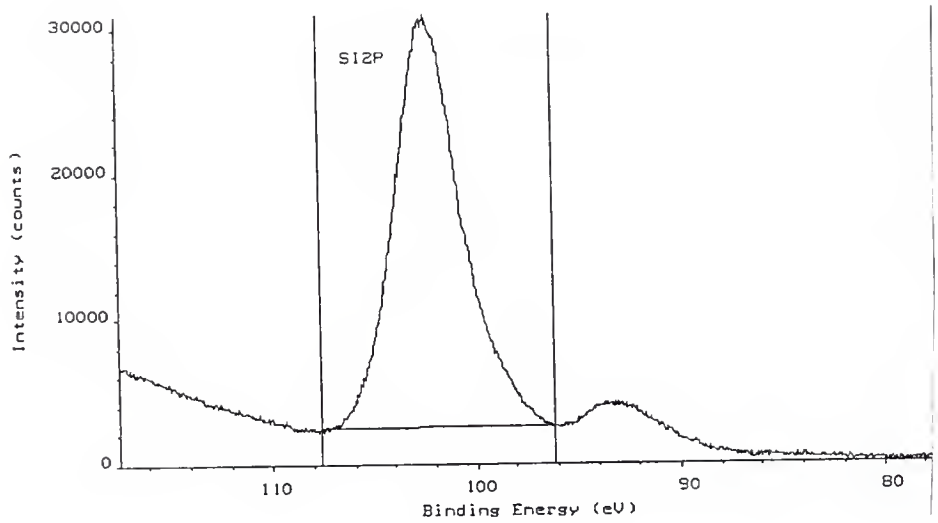

(a)

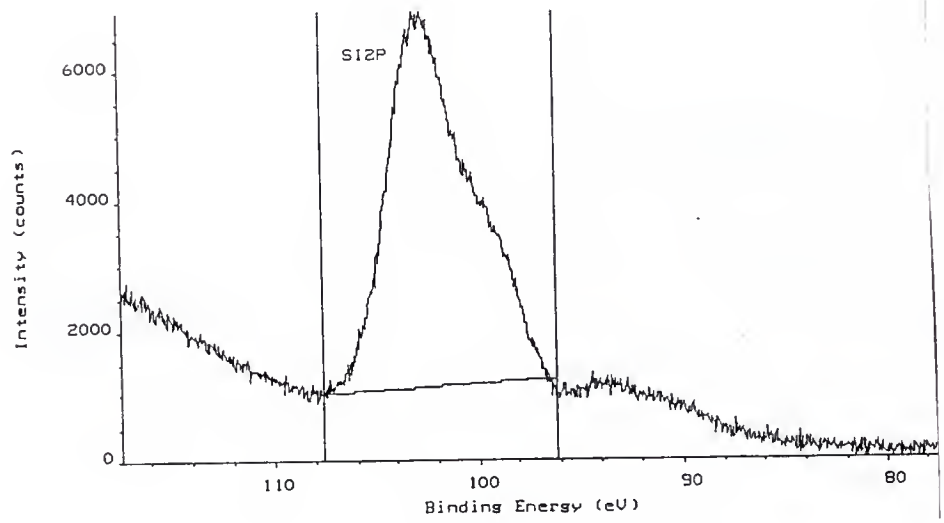

(b)

Figure 76 XPS spectrums on Si_3N_4 surface, (a) Si-2p peak from polished surface and (b) Si-2p peak from worn surface. Both peaks shifted to SiO_2 type bond (103.7 ev) and silicon oxynitride type bond (102.8) locations. The standard peak of Si_3N_4 type bond is located at 101.8 ev.

i.e., formation of SiO_2 and silicon oxynitride on the surface. These types of reactions, however, reduced the wear due to a decrease in surface friction based on Fischer and Tomizawa's experiment in reference [12]. In addition, the tribochemical film on wear scars, which was reported in references[11,12,22,25], was not found on the worn balls in Si_3N_4 hybrid ball bearing system nor on the cyclic contact fatigue specimens. This result further indicates that tribochemical wear is not a primary wear mechanism in the hybrid ball bearing but contact stress fatigue is.

CHAPTER 5
CONCLUSIONS

Type A silicon nitride bearing materials have been studied. The increase in crack resistance with crack size (R-curve or T-curve behavior) was exhibited in the bearing materials. However, the strength of the materials still show their sensitivity to crack size. Under mechanical stresses, either monotonic loading or cyclic loading, the material failure Mode Is a brittle fracture process, i.e., material failure under Mode I stress. Therefore, silicon nitride degradation during hybrid ball bearing operation is a brittle fracture process.

Problems in studying wear always exist due to the large number of variables involved in the wear process and any change in the variables will potentially lead to a wear rate change, perhaps even a wear mechanism change [139]. Wear problems in a Si_3N_4 hybrid ball bearing system are also very complicated, and involve many wear mechanisms. However, thoughtful studies of the primary bearing ball wear patterns can help find the primary causes of wear.

In this research, based on the typical silicon nitride ball wear pattern from bearing tests, the wear ball surface was carefully studied using XPS, EDS, and fracture surface analysis. Tribochemical wear is not a primary wear mechanism in the bearing system. Fracture surface analysis of the wear pattern identified multiple Hertzian contact stress fatigue as the cause of wear; this process contributes to major volume loss in the Si_3N_4 ball.

In this study, contact stress fatigue was considered a primary wear mechanism. After extensive experimental investigation in silicon nitride wear, it is hypothesized that the wear process in the hybrid ball bearing system occurs in the following manner. Wear in the silicon nitride bearing ball is initiated by contact fatigue stresses. Each wear stage described in chapter 4 can cause silicon nitride debris e.g., a grain or a conglomerate of many grains (Figure 77), which subsequently deposit in the lubricant. The debris in the lubricant creates a second wear mechanism that is essentially three body abrasive wear; i.e., scratching or cutting in both silicon nitride and M50 steel race surfaces. Furthermore, the large pieces of debris in the lubricant act as sharp indenters and create larger local inelastic deformation regions in the ball or race surface due to their indentation. The lateral cracks from this process could be initiated underneath the free surface due to local

Figure 77 Wear debris was collected from the lubricant after a ball on disc contact fatigue test

inelastic deformation. Therefore, the third wear mechanism starts to join in the wear process, i.e., spallation. The wear process is also shown schematically in Figure 78.

Wear degradation in silicon nitride hybrid ball bearing systems involves multiple wear mechanisms, but contact stress fatigue is the primary mechanism, and this mechanism determines the entire wear or degradation process. Consequently, an increase in contact stress fatigue resistance in Si_3N_4 can lead to significant reduction of overall wear in the system.

The study of the wear mechanism in silicon nitride bearing materials under contact fatigue stresses can be summarized as follows:

1. Throughout the wear processes, cyclic tensile stress (Mode I) plays a decisive role in causing grain boundary fracture, cone crack formation, and crack development in Si_3N_4. Si_3N_4 wear due to cyclic contact fatigue loading is a brittle fracture process under Mode I stress.

2. Three different wear appearances in Si_3N_4 bearing materials were observed. Grains are pulled out from the contact surface; this process increases surface roughness in this area dramatically. Cone-cracks are initiated near the maximum tensile stress region which is just outside the contact area. The material lifetime is considered as the time when a cone-

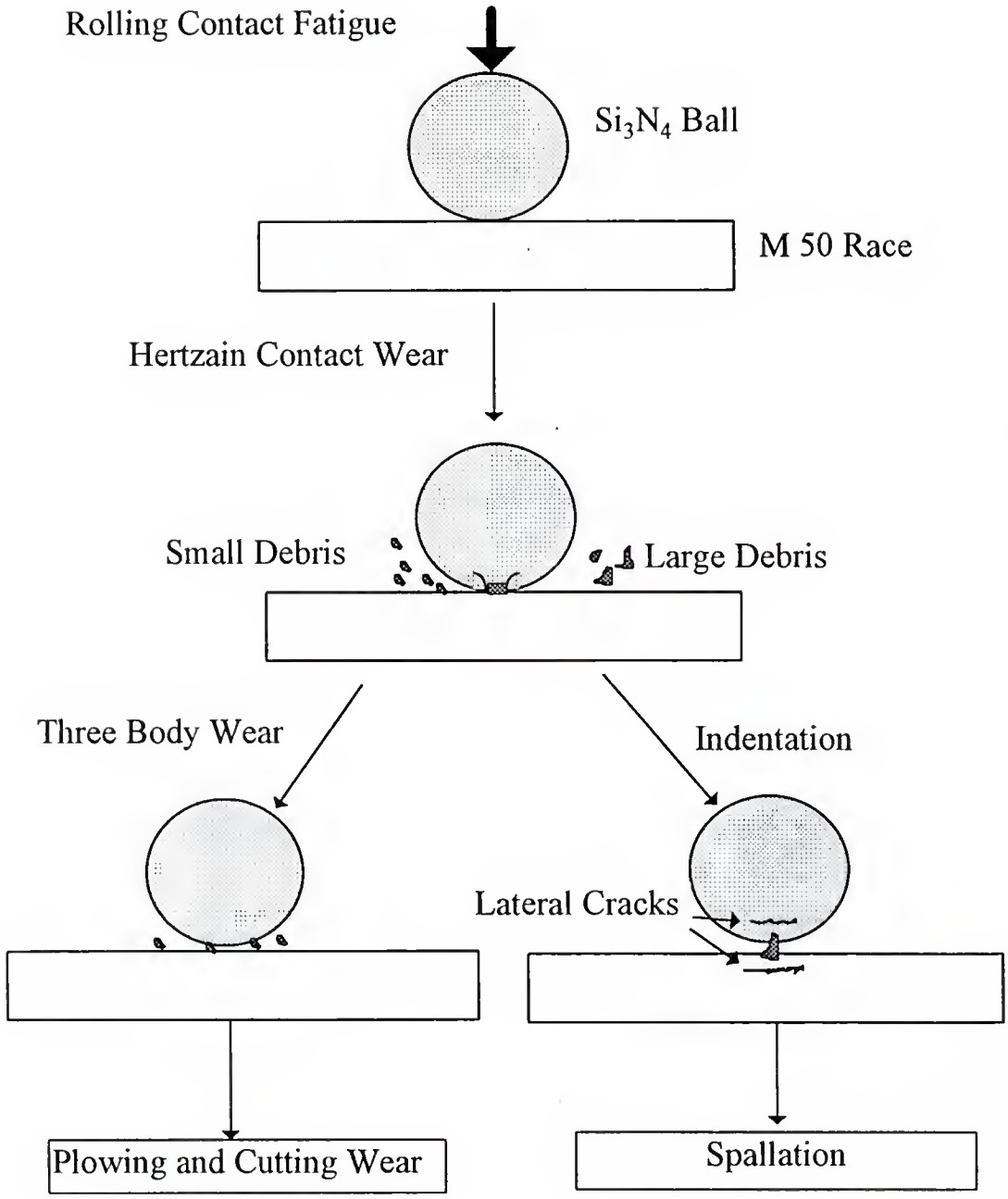

Figure 78 Schematic showing the wear process in Si_3N_4 hybrid ball bearing system.

crack forms a full circle. The number of cycles to form a full circle cone-crack under the maximum contact stresses are plotted in Figure 79. The lifetime of silicon nitride material (type A) increases exponentially when the maximum contact stress decreases.

3. Different stress states created by cyclic contact loading in the ball on disc test can be used to study different types of failure. Since the stress field is well defined, from the failure location and crack direction, the failure mode can be easily determined. In addition, the advantages of the testing method are: simple specimen preparation and ease of use for studying the influence of environments on material behavior.

4. Material heterogeneity exists in silicon nitride materials. The heterogeneous nature of the silicon nitride grains and the grain boundary phases results in wear initiation, i.e., grain pull-out. This wear initiation is due to the viscoelastic-elastic mechanical response of the grain boundaries to the stress loading. Wear then develops quickly from these initiation sites.

5. Static and cyclic fatigue tests have been conducted on bearing materials. The results showed that cyclic fatigue crack growth contributes to a major volume loss of Si_3N_4 material. Water and Exxon turbo oil can enhance cyclic fatigue crack growth. Therefore, both cyclic fatigue stress

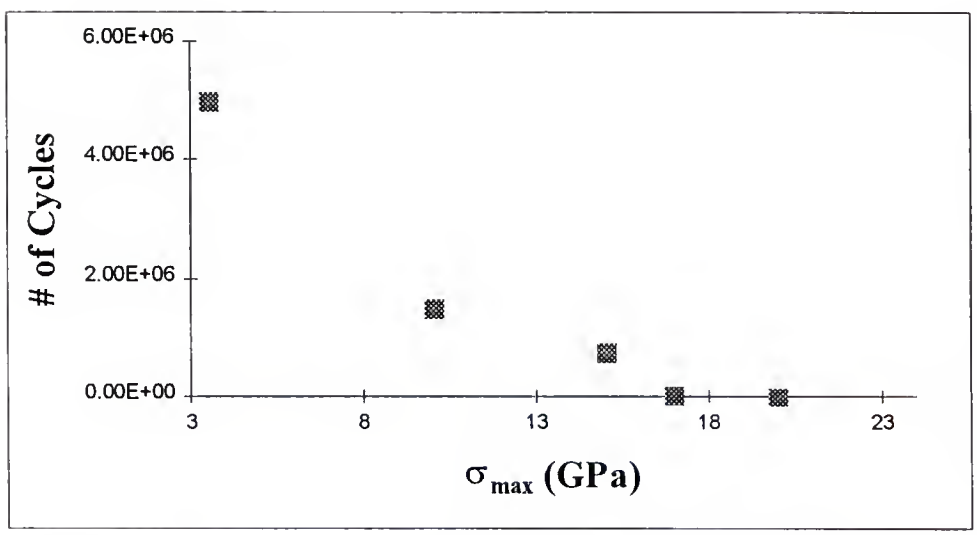

Figure 79 The contact fatigue lifetime of type A Si_3N_4 increases exponentially after $\sigma_{max} < 10$ GPa.

and the environment control wear development.

6. Surface finishing conditions for silicon nitride materials can affect wear behavior. Lateral defects on the surface such as scratches and cracks cause much more severe material degradation in silicon nitride than the surface roughness does. The lateral defects not only promote wear initiation but also increase wear at lower stress levels. More attention needs to be paid to eliminate lateral defects than to decrease surface roughness in selection of the lapping process.

7. This study indicates that the weakness of grain boundaries is a primary factor which limits silicon nitride lifetime. The weakness of the boundaries refers to not only low strength and high environmental sensitivity, but also to the material heterogeneous behavior which results in an extra tensile stress in the boundary phase. Therefore, improvement of microstructure would require small rod-like grain structure which would limit any extra tensile stress along the boundaries. The sintering phases should form a strong bond with the Si_3N_4 grains, and should have less reactivity with the environments such as OH^- group, and less delayed deformation behavior. The ideal material is the structure without, or with

less amount of grain boundary phase, or with crystallized grain boundary phase.

Another structure which may improve silicon nitride wear resistance is amorphous silicon nitride due to its homogeneity and absence of grain boundary. Based on a preliminary experiment, an amorphous CVD silicon nitride coating provides good wear resistance against cyclic contact fatigue wear under the maximum contact stress less than 7 GPa. No visible contact surface wear has been observed after 4.5 million cycles and under 7 GPa. Under a higher contact stress, interfacial debonding occurred at the interface between the CVD film and silicon nitride substrate. Using amorphous structures to eliminate the boundary shows potential as another interesting way to improve silicon nitride wear resistance.

8. The fractal dimension measurement technique has been successfully used in this study to identify wear as a brittle fracture process. Additional information found from this research is that the brittle fracture surfaces for an identical material have the same fractal dimension regardless of the stress states resulting in fracture. This discovery clearly suggests that fracture in brittle materials is a bond breaking process under Mode I stress. Mixed mode stresses can change the direction of crack propagation, but

Mode I stress is the stress creating fracture. Furthermore, the fractal approach is not just a creation of fractal number from these fascinating fracture surfaces, but also a unique tool which can be used to identify material failure modes from the failure surface. With continuous improvement in both the knowledge of fractal fracture and fractal measurement techniques, the fractal approach could become one of the powerful techniques in discovering the nature of the fracture and the relationship between fracture and the material's structure.

The study of wear is so fantastic because not only is a challenge but also it has broad variation. For any change in the wear environment, the mechanism can shift from one type to another, and wear rate can also be changed by orders of magnitude. So, caution must be paid in using wear models to explain the wear process. Moreover, with continuous development of bearing materials and bearing systems, the constant study of wear is needed. However, even though wear is a complicated phenomenon, if great effort is put into finding the primary factor in the wear process, the complicated problem will be straightened out and become a simple problem. This study has successfully demonstrated this truth.

APPENDIX A
FINITE ELEMENT ANALYSIS

The finite element method is one of the most popular numerical analysis techniques widely used by engineers and scientists. It is used to obtain approximate solutions to a wide variety of engineering and scientific problems, one of which is the stress distribution in solids.

For the problem of Hertzian contact we can use the model of axial symmetric analysis which is considered two dimensional to replace the three dimensional analysis. The indenter is spherical and the sample dimension is sufficiently large comparing with the contact area. It is obviously preferable to model the problem using a two dimensional analysis to reduce a tremendous amount of computational effort without sacrificing accuracy. Therefore, two dimensional elements are used but all three dimensional non-zero stress components will be obtained.

A commercially available finite element analysis (FEA) software ANSYS was used for all finite element analyses. This software provides a wide variety of element types and analysis capabilities.

In the beginning, we used two dimensional elements for both the spherical indenter and the sample ceramics, and point-to-surface contact elements to join the nodes between the elements of sample and indenter at the potential contact area. The dimensionless contact elements used present a bi-linear stress/strain relationship under loading [140]. When under no contact stress, the contact elements do not function, which allows for the physical separation between the sample and the indenter. When under contact stress, the elements function like stiff springs which permit the continuity of contact stress and displacement by allowing minimum penetration of the indenter into the sample. The spring constant is chosen an order of magnitude greater than the stiffness of the adjacent material with higher stiffness [140] and the zero friction coefficient was set according to the experiment condition. Ideally the spring constant should be infinite to prevent any unrealistic physical penetration. However, in reality a large spring constant will introduce extensive numerical error in the numerical process leading to a very slow convergence or even failure to convergence.

Next, a Hertzian distributed pressure is applied on the sample to simulate the contact between two frictionless elastic solids of revolution. The purpose of doing this is to compare the results from both analyses ---

real contact (RC) which is discussed above and simulated contact (SC) under which the Hertzian distributed pressure is used as the loading boundary condition. If the agreement is acceptable, the performance of nonlinear, complex and computing time consuming real contact analyses will not be necessary. The comparison shows that the discrepancy resulted is by no mean significant. Take the example of glass under a load of 124.58 N which was run for a test. The maximum σ_r which occurs at the edge of contact zone was found 260.861 MPa (RC) and 260.702 MPa (SC). The minimum σ_Z which occurs at the center of the contact was obtained as -2140.0 MPa (RC) and -2154.0 MPa (SC). The errors for both components are consider negligible due to the nature of computational analysis. We conclude, therefore, that it is sufficient to use Hertzian distributed pressure to simulate the real contact situation. Several plots of stress contour can be found in the context.

Finally, a finite element analysis was performed for the ceramics sample containing a Hertzian cone crack (HCC) due to the fatigue contact loading. FEA has a long history of being used to simulate crack propagation. The general tactic is as follows. First we arrange the FEA mesh line coincidence with the predicted crack propagation path. Next we

examine the crack tip strain energy release rate numerically. If the strain energy release rate obtained is greater than or equal to its critical value, the crack will be allowed to propagate. The crack tip node will then be relaxed into two nodes and crack extension will be one element length in the predicted direction. Nonetheless, if we do not know the crack propagation path beforehand, the prediction will be rather difficult. It is well known that for monolithic materials like the ceramics sample being tested, any crack will tend to follow a path for which the stress intensity at the crack tip is purely Mode I (crack opening). The crack propagation direction, accordingly, will be the direction at which the strain energy release rate for Mode II fracture vanishes. If the determination of the crack propagation direction is achievable though tedious, the determination of the crack path will not be considered achievable specially if the crack has a high curvature path such as the initial stage of HCC. It becomes an element size dependent problem. In other words, different FEA meshes will result in different crack paths. For the case of HCC, it is initiated somewhere outside of the contact edge and propagating perpendicular to the surface. The crack gradually alters its direction within a few dozen microns and later propagates asymptotically toward a constant angle. We do not intend to simulate the

initial HCC path which has been done using analytical prediction already. Since at later stage HCC propagates almost with a constant angle with the surface, we can consider the HCC as a straight line initiating from the contact edge. We believe that the curvature at its initiation will not affect the late stage HCC propagation.

The next task is to determine this angle. According to the concept described above, we obtained the angle with respect to the surface as 24.4 degrees for a crack length of 0.160 mm. Several stress contour plots for the ceramics sample with HCC are given in the context in corresponding to the stress plots without HCC. It has been shown in a parametric FEM study that the effect of crack length variation on the angle is small. There are many FEA techniques available for calculating the crack tip strain energy release rate. The one we employed is crack closure integral method. The detail of this technique can be found in [141]. In the analysis it was assumed that the creation and propagation of Hertzian cone crack do not affect the given Hertzian distributed pressure.

The program code used in this research is shown as following:

```
/BATCH
/COM,ANSYS REVISION  5.0
/show,vga
/unit,si
/auto,all
```

```
/dist,,5
/prep7
!
e1=309.0e3
e2=625.e3
nu1=.27
nu2=.24
pp=2015.5
rr=2.38
est=1./((1.-nu1**2)/e1+(1.-nu2**2)/e2)
aa=(3.*pp*rr/(4.*est))**(1./3.)
p0=.47746*pp/aa**2
!ax=1.2*aa
ax=0.26
!
et,1,42,,,1
mp,ex,1,e1
,nuxy,1,nu1
mp,ex,2,e2
,nuxy,2,nu2
!
ang1=65.6
ang2=ang1
ang3=ang1
rad1=ang1/180.*3.1415926
rad2=ang2/180.*3.1415926
rad3=ang3/180.*3.1415926
crack1=0.16
crack2=0.1
crack3=0.1
x1=crack1*sin(rad1)+ax
y1=-crack1*cos(rad1)
x2=x1+crack2*sin(rad2)
y2=y1-crack2*cos(rad2)
x3=x2+crack3*sin(rad3)
y3=y2-crack3*cos(rad3)
y4=y3-(5.6-x3)/tan(rad3)
k,1
,,,-ax
,,,-5.6
,,5.6,-5.6
,,x3,y3-ax
,,x2,y2-ax
,,x1,y1-ax
,,ax,-ax
,,5.6,y4
```

,,5.6
,,x3
,,x3,y3
,,x2,y2
,,x1,y1
,,ax
,,ax
!,,x1,y1
!,,x2,y2
l,1,15
,1,2
,2,3
,3,4
,5,4
,6,5
,6,7
,7,8
,8,2
,4,9
,12,5
,6,13
,7,14
,8,15
,12,9
,9,10
,11,10
,11,16
,11,12
,12,13
,13,14
,14,15
,14,16
!,16,17
!!,13,17
!!!,18,17
!!!,18,12
a,1,15,8,2
,15,14,7,8
,14,13,6,7
,13,12,5,6
,16,11,12,13,14
!!,16,11,12,13,17
!!!,16,11,12,18,17
,11,10,9,12
,12,9,4,5
,2,8,7,6,5,4,3

```
lesize,1,,,10
,2,,,10
,3,,,33,28
,4,.56
,5,,,33,28
,6,.02
,7,.02
,8,.02
,9,,,10
,10,.56
,11,.02
,12,.02
,13,.02
,14,,,10
,15,,,33,28
,16,.56
,17,,,33,28
,18,.02
,19,.02
,20,.02
,21,.02
,22,.02
,23,.02
!,24,.02
!,25,.02
save
mat,1
amesh,1,8,1
!
finish
/solu
lsel,,loc,y,-5.6
nsll,,1
d,all,uy
nsel,all
lsel,,loc,x,-.0001,.0001
nsll,,1
d,all,ux
nsel,all
!
nx=10
axx=ax/nx
*do,i,1,10
/gopr
aw1=(i-1)*axx-0.00001
aw2=i*axx+0.00001
```

```
av1=p0*sqrt(1.-(aw1/aa)**2)
*if,aw2,gt,aa,then
av2=0.
*else
av2=p0*sqrt(1.-(aw2/aa)**2)
*endif
sl=(av2-av1)/axx
nsel,,loc,x,aw1,aw2
nsel,r,loc,y,-.0001,.0001
sfgrad,pres,,x,aw1,sl
sf,all,pres,av1
allsel
*if,aw2,gt,aa,exit
*enddo
sflist
/psf,pres,norm,1
solve
save
finish
/exit,nosav
```

APPENDIX B
A COMPUTER PROGRAM FOR PREDICTION OF CRACK PATH

```
C     In this program, a correct integral is use.
C     The old ones are incorrect.
C     pr: principal stress.
C     sr: sigma r, the normal stress parallel to the plane.
C     sz: sigma z, the normal stress normal to the plane.
C     tzr: tau rz, the shear stress.

C
C
C
      REAL x(500), pr(500), x1(2500), z1(2500)
      COMMON aa, p0, anu, d, npts2, da, npts4
*
      pp = 11651.2
*     Total applied force.

      ee = 309.0E 3
*     Young's modulus of glass.

      anu = .27
*     Poisson's ratio of glass.

      rr = 2.38125
*     Radius of indentor.

      ee2 = 625.0E 3
*     Young's modulus of indentor.

      anu2 = .24
*     Poisson's ratio of indentor.

      del = .0005
*     Increment you want for finding maximum principal stress
*      on top surface.

      cl = 0.01
```

```
*       The distance of crack tip to the top surface.

        est = 1.0 / ((1.0 - anu ** 2) / ee + (1.0 - anu2 ** 2) / ee2)
*       E* (ref. 97)

        aa = (3.0 * pp * rr / (4.0 * est)) ** (1.0 / 3.0)
*       Radius of contact area.

        p0 = 1.5 * pp / aa ** 2 / 3.14159
*       Maximum distributed pressure.

        npts1 = 100
*       Number of points calculated to select the max. principal stress
*       at top surface.

        npts2 = 200
*       Number of points in integration.

npts3 = 300
* Number of points you want to calculate in crack direction.

        d = aa / npts2
*       Integration step.

        npts4 = npts2 / 4
*       Number of points in circular integration.

        da = 3.14159 / npts4
*       Circular integration step.

        prm = 0.0

         DO 10, i = 1,  npts1
         x(i) = del * (i - 1) + aa + 0.001
              pr(i) = (FNSr(0.0, x(i)) + FNSz(0.0, x(i))) / 2.0 +
*        SQRT(((FNSr(0.0, x(i)) - FNSz(0.0, x(i))) / 2.0) ** 2 +
*        FNTrz(0.0, x(i)) ** 2)
*       PRINT *, 'pr, x =', pr(i), x(i)
         IF (pr(i) .GT. prm) THEN
         prm = pr(i)
         ii = i
         END IF
10       CONTINUE
```

```
      PRINT *, 'x(ii)=', x(ii), ii
      PRINT *, 'prm=', prm
      prm1=(1.-2.*anu2)*pp/(2.0*3.1415926*aa**2)
      PRINT *, 'prm1=', prm1

      case=2
      IF (case.EQ.1) THEN
      x1(1) = x(ii)
      ELSE IF (case.EQ.2) THEN
      x1(1) = aa * 1.03
      ELSE
      x1(1) = aa + 0.00001
      END IF

      z1(1) = 0.0
      PRINT *, 'ee,nu,ee2,nu2', ee, anu, ee2, anu2
      PRINT *, 'e*=', est
      PRINT *, 'aa=', aa
      PRINT *, 'p0=', p0
      PRINT *, 'distance=', x1(1)
      PRINT *, 'max principal stress=', prm

*     h = cl / npts3
*     h = 0.0001
      h = 0.001

      DO 20, i = 2 , npts3
      z1(i) = z1(i - 1) + h
      zz = z1(i - 1)
      xx = x1(i - 1)
      ak1 = h * FNF(zz, xx)
      zz = z1(i - 1) + h / 2.0
      xx = x1(i - 1) + ak1 / 2.0
*     print *, 'ak2, z,x', zz, xx
      ak2 = h * FNF(zz, xx)
      zz = z1(i - 1) + h / 2.0
      xx = x1(i - 1) + ak2 / 2.0
*     print *, 'ak3, z,x', zz, xx
      ak3 = h * FNF(zz, xx)
      zz = z1(i - 1) + h
      xx = x1(i - 1) + ak3
      ak4 = h * FNF(zz, xx)

*     print *, 'aks=', ak1, ak2, ak3, ak4
      x1(i) = x1(i - 1) + (ak1 + ak2 * 2.0 + ak3 * 2.0 + ak4) / 6.0
```

```
      IF (i .EQ. 2) THEN
      angl = ATAN2((x1(2) - x1(1)), z1(2) - z1(1)) * 180.0 /
     *  3.14159
      PRINT *, 'angle', angl
      END IF
20    CONTINUE

      DO 30, k = 1 , npts3
      IF (k.LT.npts3) THEN
      angl = ATAN2((x1(k+1)-x1(k)), z1(k+1)-z1(k)) * 180.0/3.1415926
      END IF
      IF (k.LT.50) THEN
      PRINT *, 'z, x & ang', z1(k), x1(k), angl, k
      ELSE IF (MOD(k,10).EQ.0) THEN
      PRINT *, 'z, x & ang', z1(k), x1(k), angl, k
      END IF
30    CONTINUE
      STOP
      END


      REAL FUNCTION FNSr (z, r)
      COMMON aa, p0, anu, d, npts2, da, npts4
      srs = 0.0
      srs1 = 0.0
      DO 40, j = 1 , npts2 + 1
      IF ((j .EQ. 1) .OR. (j .EQ. (npts2 + 1))) THEN
      tt = .5
      ELSE
      tt = 1.0
      END IF
      s = d * (j - 1)
      DO 45, k = 1 , npts4 + 1
      IF ((k .EQ. 1) .OR. (k .EQ. (npts4 + 1))) THEN
      ttt = .5
      ELSE
      ttt = 1.0
      END IF
      alf = da * (k - 1)
      srs = srs + tt * ttt *
     *  ((1.0 - 2.0 * anu) *
     *  (1.0 / (r ** 2 + s ** 2 - 2.0 * r * s * cos(alf))) * (1.0
     *  - z /SQRT(r** 2 + s ** 2 + z**2 - 2.0 * r * s * cos(alf)))
     *  - 3.0 * z * (r ** 2 + s ** 2 - 2.0 * r * s * cos(alf))
     *  /(SQRT(r** 2 + s ** 2 - 2.0 * r * s * cos(alf)+z** 2))**5)
```

```
45      CONTINUE
        srs1 = srs1 + srs * s * SQRT(1.0 - (s / aa) ** 2)
        srs = 0.
*       print *, "srs=", srs1
40      CONTINUE
        FNSr = srs1 * d * da * p0 / 3.14159
*       print *, "x=", r, "z=", z, "srs=", srs
*       print *, "x=", r, "z=", z, "srs=", FNSr
        RETURN
        END


        REAL FUNCTION FNSz (z, r)
        COMMON aa, p0, anu, d, npts2, da, npts4
        szs = 0.0
        szs1 = 0.0
        DO 50, j = 1 , npts2 + 1
        IF ((j .EQ. 1) .OR. (j .EQ. (npts2 + 1))) THEN
        tt = .5
        ELSE
        tt = 1.0
        END IF
        s = d * (j - 1)
        DO 55, k = 1 , npts4 + 1
        IF ((k .EQ. 1) .OR. (k .EQ. (npts4 + 1))) THEN
        ttt = .5
        ELSE
        ttt = 1.0
        END IF
        alf = da * (k - 1)
        szs = szs + tt * ttt
    *   /(SQRT(r ** 2 + s ** 2 - 2.0 * r * s * cos(alf) + z ** 2))**5
55      CONTINUE
        szs1 = szs1 + szs * s * SQRT(1.0 - (s / aa) ** 2)
        szs = 0.
50      CONTINUE
        FNSz = -szs1 * d * da * p0 * z ** 3 * 3.0 / 3.14159
        RETURN
        END

        REAL FUNCTION FNTrz (z, r)
        COMMON aa, p0, anu, d, npts2, da, npts4
        trzs = 0.0
        trzs1 = 0.0
        DO 60, j = 1 , npts2 + 1
```

```
      IF ((j .EQ. 1) .OR. (j .EQ. (npts2 + 1))) THEN
      tt = .5
      ELSE
      tt = 1.0
      END IF
      s = d * (j - 1)
      DO 65, k = 1 , npts4 + 1
      IF ((k .EQ. 1) .OR. (k .EQ. (npts4 + 1))) THEN
      ttt = .5
      ELSE
      ttt = 1.0
      END IF
      alf = da * (k - 1)
      trzs = trzs + tt * ttt *
     *  SQRT(r ** 2 + s ** 2 - 2.0 * r * s * cos(alf))
     *  /(SQRT(r ** 2 + s ** 2 - 2.0 * r * s * cos(alf) + z ** 2))**5
65    CONTINUE
      trzs1 = trzs1 + trzs * s * SQRT(1.0 - (s / aa) ** 2)
      trzs = 0.
60    CONTINUE
      FNTrz = -trzs1 * d * da * p0 * z ** 2 * 3.0 / 3.14159
      RETURN
      END


      REAL FUNCTION FNF (z, r)
      COMMON aa, p0, anu, d, npts2, da, npts4
      ss = (FNSr(z, r) + FNSz(z, r)) / 2. + SQRT(((FNSr(z, r)
     *  - FNSz(z, r)) / 2.) ** 2 + FNTrz(z, r) ** 2)
*     FNF = -(ss - FNSr(z, r)) / FNTrz(z, r)
      IF (abs(ss-FNSz(z,r)).le.0.001) THEN
      FNF=0.0
      ELSE
      FNF = -FNTrz(z, r)/(ss - FNSz(z, r))
      END IF
*     print *, 'trz,ss,sr,z,r',FNTrz(z,r),ss,FNSr(z,r), z, r
      RETURN
      END
```

REFERENCES

1. J. Hannoosh, Design News, 11-21-88, pp. 224-31.

2. K. Taylor, L. Sibley, and J. Lawrence, Wear, [6], 226-40 (1963).

3. K. Jack, "The crystal chemistry of the Sialons and Related Nitrogen Ceramics", pp.109-28 in Nitrogen Ceramics, Edited by F. Riley, Noordhoff International Publishing, Leyden, Netherlands, 1977.

4. F. Riley, "Nitridation and Reaction Bonding", pp. 265-88 in Nitrogen Ceramics, Edited by F. Riley, Noordhoff International Publishing, Leyden, Netherlands, 1977.

5. D. Richerson, Am. Ceram. Soc. Bull., 52[7] 560-69 (1973).

6. L. Gauckler, S. Boskovic, G. Petzow, and T. Tien, "Desification b-Si3N4 Solid Solutions Containing AlN:Al2O3 During Chemical Reaction", pp. 41-62 in Nitrogen Ceramics, Edited by F. Riley, Noordhoff International Publishing, Leyden, Netherlands, 1977.

7. C. Greskovich and C. O'Clair, Am. Ceram. Soc. Bull., 57[11] 1055-56 (1978).

8. A. G. Evans, "The Fracture of Brittle Materials" pp. 451-75 in Nitrogen Ceramics, Edited by F. Riley, Noordhoff International Publishing, Leyden, Netherlands, 1977.

9. D. Clark and G. Thomas, J. Am. Ceram. Soc., 61[3-4] 114-18 (1977).

10. A. Tsuge and K. Nishida, Am. Ceram. Soc. Bull., 57[4] 424-31 (1978).

11. M. Akazawa, Wear, 124(1988)123-32.

12. T.E. Fischer and H. Tomizawa, Wear, 105(1985)29-45.

13. J.F. Braza and H.S. Cheng, Tribology Transactions, 32(1989)4439-46.

14. B.C. Bunting, Lubrication Engineeing, 46[11]745-51.

15. A.T. Galbato, R.T. Cundill, and T.A. Harris, Lubrication Engineeing, 46[11]886-94.

16. S.W. Freiman, A. Williams, J.J. Mecholsky, and R.W. Rice, in Ceramic Microstructures `76, R.M. Fulrath and J.A. Pask (eds.), Westview Press, Boulder, Colorado, 1977.

17. R.W. Rice, K.R. McKinney, C.C. Wu, and S.W. Freiman, J. Mater. Sci., 20(1985)1392-1406.

18. M.G. Jenkins, M.K. Ferber, and C.K. Lin, J. Am. Ceram. Soc., 76[3]788-92(1993).

19. F. Lange, J. Am. Ceram. Soc., 57 [2] 84-87 (1972).

20. R. Rice,K, McKinney, C. Wu, S. Freiman, and W. McDonough, J. Mater. Sci., 20, 1392-1406 (1985).

21. P.J. Kennedy, A.A. Conte, Whitenton, L.K. Ives, and M.B. Pertson, in Friction and Wear of Ceramics, S. Jahanmir (ed.), pp. 79-98.

22. R. Gates and S. Hsu, Tribology Transactions, 34 (1991), 3, 417-425.

23. X. Dong and S. Jahanmir, Wear 165 (1993) 169-180.

24. J. Lucek, Prsented at the Gas Turbine and Aeroengine Congress and Exposition, June 11-14, 1990, Brusseis, BelgiumASME paper No. 90-GT-165.

25. S. Danyluk, M McNallan, and D. Park, in Friction and Wear of Ceramics, S. Jahanmir (ed.), pp. 61-77.

26. O. Adewoye, Wear, 70 (1981) 37-51.

27. D. Scott, J. Blackwell, and P. McCullagh, Wear, 17 (1971) 73-82.

28. D. Broek, Elementary Engineering Fracture Mechanics, Sijthoff & Noordhoff, Alphen aan den Rijin, The Netherlands, 1978.

29. L. Ewart and S. Suresh, J. Mater. Sci. Lett. 5, 774 (1986).

30. L. Ewart and S. Suresh, J. Mater. Sci., 22, 1173 (1987).

31. A. Hartman, Int. J. Fracture Mech., 1 (1965) 167-88.

32. M. Achter, ASTM STP 415, (1967) 181-204.

33. R. Wei, Eng. Fracture Mech., 1 (1970) 633-51.

34. F. Guiu, J. Mater. Sci. 13, 1375 (1978).

35. S. Lathabai, J. Rodel and B. Lawn, J. Am. Ceram. Soc., 74, 1340 (1991).

36. T. Kishimoto, A. Ueno, and H. Kawamoto, Mechanical behavior of materials, Edited by M. Jono and T. Inoue, Vol. 2, p. 357, Pergamon Press, Oxford 1991).

37. J. Beals and I. Bar-On, ceram. Eng. Sci. Proc., 11 (1992) 1061.

38. Paris, P. C., The Growth of Fatigue Cracks due to Variations in Load, Ph.D. Thesis, Lehigh University (1962).

39. D. Wilhem, ASTM STP 415 (1967) 363-83.

40. C. Hudson, NASA TN-D-2331 (1964).

41.A. Cottrell and D. Hull, Proc. Roy. Society, A 242 (1957) 211-17.

42. N. Mott, Acta Met., 6 (1958) 195-197.

43. S. Wiederhorn and L. Bolz, J. Amer. Ceram. Soc. 53 (1970) 543.

44. H. Nelson, D. Williams, and A. Tetelman, Met. Trans, 2 91971) 953.

45. R. Dauskardt, W. Yu and R. Ritchie, J. Am. Ceram. Soc. 70, 248-52 (1987).

46. S.-Y Liu and I.-W Chen, J. Am. Ceram. Soc. 74, 1197-216 (1991).

47. D. Davison, J. Campbell, and J. Lankford, Acta Metall. Mater., 39, 1319-30 (1991).

48. H. Ko, J. Mater. Sci. Lett., 5, 464-66 (1986).

49. T. Hoshide, Tohara, and T, Yamada, Int. J. Fracture, 37, 47-59 (1988)

50. T. Kawakubo and K. Komeya, J. Am. Ceram. Soc. 70, 400-05 (1987).

51. A. G. Evans, Intl. J. Fracture, 16, 485 (1980).

52. T. Kawakubo, N. Okabe, and T. Mori, Fatigue '90, pp. 717-32 in Proc. 4th Intl. Conf. On Fatigue and Fatigue Thresholds, vol. 2, Edited by H. Kitagawa and T. Tanaka, Mat. Comp. Eng. Publ., Ltd., Edgbaston, U.K. (1990).

53. D. Cardona and C. Beevers, Fatigue '90, pp. 1023-29 in Proc. 4th Intl. Conf. On Fatigue and Fatigue Thresholds, vol. 2, Edited by H. Kitagawa and T. Tanaka, Mat. Comp. Eng. Publ., Ltd., Edgbaston, U.K. (1990).

54. H. Ko, J. Mater. Sci. Lett., 8, 1438-41 (1989).

55. S. Lauf, V. gerold, and R. Babst, Fatigue '90, pp. 775-80 in Proc. 4th Intl. Conf. On Fatigue and Fatigue Thresholds, vol. 2, Edited by H. Kitagawa and T. Tanaka, Mat. Comp. Eng. Publ., Ltd., Edgbaston, U.K. (1990).

56. T. Kawakubo and K. Komeya, J. Am. Ceram. Soc., 70 (1987) 400.

57. S. Horib and R. Hirahara, Acta Metall Mater, 39[6]1309-17(1991).

58. H. Kirchner, R. Gruver,and D. Richard, J. Mater. Sci., 14 (1979) 2713-2720.

59. J. Burke, R. Doremus, A. Turkalo, and W. Hilling, G. E. Report No. 71-C-035, Jan. 1971.

60. S. Freiman and J.J. Mecholsky, Fractography: A Quantitative Measure of the Fracture Process, pp. 55-78 in Fractography of Glass and Ceramics II, Edited by V. Frechette and J. Varner, The Amer. Ceram. Soci., Inc., Westervill, Ohio, 1990.

61. Y. Tsai, Ph.D. Thesis, The University of Florida, 1993.

62. J.J. Mecholsky, D. Passoja, and K. Feinberg-Ringel, J. Am. Ceram. Soc. 72 [1] 60-65 (1989).

63. Standard Terminology Relating to Wear and Erosion, American Soc. Test. Mater., ASTM G40-92

64. B. Frisch, Adhesive Wear, pp. 174-181 in Metallurgical Aspects of Wear, Edited by E. Hornbogen and K. Zum Gahr, DGM Verlag, Oberursel, 1981.

65. D. Buckley and W. Winer, Wear Control Handbook, ASME, New York 1980.

66. I. M. Hutchings, Tribology: Friction and Wear of Engineering Materials, Edward Arnold, London and CRC Press, Baco Raton, 1992.

67. E. Rabinowicz, Friction and Wear of Materials, Wiley, 1965.

68. I. Hutchings, Powder Technology, 76 (1993) 3-13.

69. B. R. Lawn and M. V. Swain, J. Mater. Sci., 10(1975)113.

70. B. Hockey, J. Am. Ceram. Soc., 54 (1971) 223-231.

71. M. Swain, Proc. R. Soc., London, A366 (1979) 575-97.

72. M. Moor and F. King, Wear, 60 (1980) 123-40.

73. J. Veldkamp and N. Hattu, J. Mater. Sci., 16 (1981) 1273-1284.

74. F. Bowden and D. Tabor, The Friction and Lubrication of Solids, Part 2. Clarendon Press, Oxford 1964.

75. D. Marsh, Proc. R. Soc., A382 (1964) 33-43.

76. A. G. Evans and D. B. Marshall,in D. A. Rigney (ed.), Fundamentals of Friction and Wear of Materials, ASM, 1981, pp.439-452.

77. A. G. Evans, in B. J. Hockey and R. W. Rice (eds.), The Science of Ceramic Maching and Surfacing Finishing II, NBS Sp. Pub. 562, Washington, 1979, 1-14.

78. T. Quinn, trib. Intl., 16, 5 (1983) 257-71.

79. R. Iler, The chemistry of Silica, Wiley, New York, 1979.

80. A.Kiehle, L Heung, P. Gielisse and T. Rockett, J. Am. Ceram. Soc., 58 (1975) 17.

81. S. Singhal, J. Am. Ceram. Soc., 59 (1976) 81.

82. A. G. Evans, J. Mater. Sci., 7 (1972) 1137.

83A. Westwood, N. Macmillan, and R. Kalyoncu, J. Am. Ceram. Soc., 56 (1975) 372.

84. N. Wallbridge, D. Dowson, and E. Roberts, pp. 202 in Proc. Intl. Conf. On Wear materials, Edited by K. Ludema, Am. Soc. Mech. Eng., New Yprk, 1983.

85. D. Cranmer, J. Soc. Tribologists and Lubrication Eng., 44[12] 1988 975-80.

86. R. Katz, pp. 313-29 in Friction and Wear of Ceramics, Edited by S. Jahanmir, Marcel Dekker, Inc, New York, 1994.

87. M. Hadfield, T. Stolarski, R. Cundill, and S. Horton, Wear, 169 (1993) 69-75.

88. H. Aramaki, Y. Shoda, Y. Morishita, and T. Sawamoto, J. Tribology, 110
(1988) 693-98.

89. H. Baumgartner, pp. 713-18 in Ceramic for High Performance Applications, Edited by J. Burke, A. Gorum, and R. Katz, Brook Hill Pulishing, Chestnut Hill, MA, 1974.

90. H. Dalal, Y.P. Chiu, And E. Rabinowitz, ASLE Trans., 18 (1975) 211.

91. B. Bhushan and L. B. Sibley, ASLE Transactions, 25[4], pp. 417-428.

92. F. Morrison, ASLE Preprints, No. 82-LC-3C-4.

93. F. Morrison, J. Pirvics, and T. Yonushonis, SKF Rept. No. AL79T033, September (1980).

94. G. Lundberg and A. Palmgren, Act Polytechnica, 196 (1947).

95. G. Lundberg and A. Palmgren, Act Polytechnica, 210 (1952).

96. H. Hertz, Miscellaneous Papers By H. Hertz,Jones and Schott, London:Macmillan, 1896, pp.156.

97. K. L. Johnson, Contact Mechanics, Cambridge University Press, Cambridge, 1985.

98. L. Yingzhi and D.A. Hills, Transactions of The ASME, [58] 120-27 (1991).

99. H. Cai, M. Kalceff, B. Hooks, B. Lawn, K. Chyung, J. Mater. Res. 9[10]

1994 2654-61.

100. H. Cai, M. Kalceff, B. Hooks, andB. Lawn, J. Mater. Res. 9[10] 1994 762.

101. B. Lawn, N. Padture, F. Guiberteau, and H. Cai, Act Metall. Mater, 42 [5] 1683-93 (1994).

102. F. Guiberteau, N. Padture, H. Cai, and B. Lawn, Phil. Mag. A. 68 (1993) pp. 1003.

103. H.K. Xu, L. Wei, N.P. Padture, and B. R. Lawn, J. Mater. Sci., in press.

104. F.L.L.B. Carniero and A. Barcellos, Rep. 13, 1953, pp98 (Union of testing and Research Laboratories for materials and Structures).

105. S. Timoshenko and J. Goodier, Theory of Elasticity, McGraw-Hill, New York, 1951.

106. J. Ovri and T. Davies, Materials Science and Engineering, 96 (1987) 109-16.

107. T. Tang, J. Testing & Evaluation, 22 [5] 401-09 (1994).

108. J.J. Mecholsky and J.R. Plaia, J. Non-crystalline Solids, 146(1992)249-255.

109. R. McMeeking and A. Evans, J. Am. Ceram. Soc., 65[5] 242-46 (1982).

110. A. Evans and K. Faber, J. Am. Ceram. Soc., 67 [4] 255-60 (1984).

111. Y. Mai and B. Lawn, J. Am. Ceram. Soc., 70 [4] 289-94 (1987).

112.A. Okada and N. Hirosaki, J. Am. Ceram. Soc., 73 [7] 2095-96 (1990).

113. J. Johnson and D. Holloway, Philos. Mag., [14] 731-44 (1951).

114. C. Li, D. Lee, and S. Lui, J. Am. Ceram. Soc, 75 [7] 177-85 (1992).

115. E. Joffe, Philos. Mag., [112] 739-50 (1951).

116. A. Clar and G. Irwin, Exp. Mech., 6[6] 321-30 (1966

117. H. Kirchner, Eng. Fract. Mech.,[10] 283-88 (1978).

118. J. Kalthoff, On the propagation Direction of Bifurcated Crack, pp. 449-58 in Dynamic Crack Propagation, Edited by G. Sith, Noordhoff International Publishing, Leyden, 1973

119. . W. Doll, Intl. J. Fracture, [11] 184-86 (1975).

120. A. G. Evans, J. Mater. Sci., 7 (1972) 1137-46.

121. R.W. Hertzberg, Deformation and Fracture Mechanics of Engineering Materials, Wiley, New York, 1989.

122. D. Kulawansa, L. Jensen, S. Langford, and J. Dickinson, J. Mater. Res., 9[2], (1994) 476-484.

123. J. Zarzycki, Glasses and the Vitreous State, Cambridge University Press, Cambridge, 1991.

124. J. De Bast and P. Gilard, Rend. Rech. IRSIA, No. 32, 1965.

125. A. Nowick and B. Berry, I.B.M. J. Res. Dev., 5 [297] 312 (1961).

126. D. Singh and D. Shetty, J. Am. Ceram. Soc., 72 [1] 78-84 (1989).

127. S. Hu, J.S. Bark, J.A. Nairn, Composites Sci. & Tech., 47(1993) 321-29.

128. Y. Li and D. Hills, Transactions of the ASME 58 Mar. (1991) 120-27.

129. R. Ritche and R. Dauskardt, J. Ceram. Soc. Janpen, 99 [10] 1047-1062

(1991).

130. S. M. Wiederhorn, S. W. Freiman, E. R. Fuller, and C. J. Simmons, J. Mater. Sci. 17 (1982) 3460-78.

131. E. B. Shand, J. Am. Ceram. Soc., 42[10](474-77)1959.

132. B.B. Mandelbrot, D. E. Passoja, and A. J. Paullay, Nature, 308 (1984) 721.

133. B.B. Mandelbrot, "The Fractal Geometry of Nature," Freeman, San Francisco, 1982.

134. J.J. Mecholsky, D.E. Passoja and K.S. Feinberg-Ringel, J. Am. Ceram. Soc., 72(1) 60-65 (1989).

135. J.J. Mecholsky and T. Mackin, J.Mater. Sci. letter, 7 (1991) 1145-47.

136. Y.L. Tsai and J.J. Mecholsky, Fractal Fracture of Single Crystall Sillicon, J. Mater. Res., 6[6]1991.

137. J.J. Mecholsky and S.W. Frieiman, J. Am. Ceram. Soc., 74[12]3136-38 (1991).

138. T. Mackin, "Fractal and Fracture," Ph.D. Thesis, The Pennsyvania State University.

139. D. Rigney, Scripta Metallurgica et Materialia, 24 (1990) 799-803.

140. ANSYS User's Manual for Revision 5.0. Swanson Analysis Systems, Inc.

141. Rybicki, E. F. and Kanninen, M. F., Engineering Fracture Mechanics, 9 (1977) 931-938.

142. J.J. Mecholsky, Jr., Quantitative Fractography: An Assessment, Fractography of Glasses and Ceramics II, Edited by V. D. Frechette and J. R. Varner, pp. 413-452, Ceramic Transactions, Vol. 17, The America

Ceramic Society, Inc. Westerville, Ohio, 1991.

BIOGRAPHICAL SKETCH

Zheng Chen was born in Shanghai, China. He attended local schools there and graduated from Huguong High School in 1979.

In 1979, he matriculated in the Materials Science and Engineering Department of Shanghai Jiaotong University, and graduated with a Bachelor of Science degree in Materials Science and Engineering in 1983.

Begining in Fall, 1983, he worked as a research associate in the Shanghai Welding Technology Institution of Shanghai Jiaotong University, until he enrolled at Pennsylvania State University and worked as Professor Jack Mecholsky's research assistant in the Fall of 1989. In the Spring of 1990, he joined the Department of Materials Science and Engineering, University of Florida. Within five and a half years at the University of Florida, under the guidance of Dr. J. J. Mecholsky, Jr, he obtained an M.S. degree and a Ph.D. degree in Materials Science and Engineering. He published 7 papers and gave 11 presentations at professional conferences.

I certify that I have read this study and that in my opinion it conforms to acceptable standards of scholarly presentation and is fully adequate, in scope and quality, as a dissertation for the degree of Doctor of Philosophy.

Ellsworth D. Whitney
Professor of Materials Science and Engineering

This dissertation was submitted to the Graduate Faculty of the College of Engineering and to the Graduate School and was accepted as partial fulfillment of the requirements for the degree of Doctor of Philosophy.

May, 1995

Winfred M. Phillips
Dean, College of Engineering

Karen A. Holbrook
Dean, Graduate School

I certify that I have read this study and that in my opinion it conforms to acceptable standards of scholarly presentation and is fully adequate, in scope and quality, as a dissertation for the degree of Doctor of Philosophy.

John J. Mecholsky, Jr. Chair
Professor of Materials Science
and Engineering

I certify that I have read this study and that in my opinion it conforms to acceptable standards of scholarly presentation and is fully adequate, in scope and quality, as a dissertation for the degree of Doctor of Philosophy.

James H. Adair
Associate Professor of Materials
Science and Engineering

I certify that I have read this study and that in my opinion it conforms to acceptable standards of scholarly presentation and is fully adequate, in scope and quality, as a dissertation for the degree of Doctor of Philosophy.

Bhavani V. Sankar
Associate Professor of Aerospace
engineering, Mechanics, and
Engineering Science

I certify that I have read this study and that in my opinion it conforms to acceptable standards of scholarly presentation and is fully adequate, in scope and quality, as a dissertation for the degree of Doctor of Philosophy.

Rajiv K. Singh
Assistant Professor of Materials
Science and Engineering

LD
1780
199_

LD
1780
1995
.C5189

UNIVERSITY OF FLORIDA
3 1262 08553 7107